WARSAW UNIVERSITY OF TECHNOLOGY

DISCIPLINE OF SCIENCE – INFORMATION AND COMMUNICATIONS TECHNOLOGY / FIELD OF SCIENCE – ENGINEERING AND TECHNOLOGY

Ph.D. Thesis

Jędrzej Drozdowicz, M.Sc.

Single Channel 3D Synthetic Aperture Radar with Platform Trajectory Tuning

Supervisor

Professor Piotr Jerzy Samczyński, Ph.D., D.Sc.

WARSAW 2023

Finansowanie – Funding

Niniejsza rozprawa powstała dzięki Narodowemu Centrum Nauki, w ramach stypendium w programie Etiuda 7 pod tytułem "Interferometryczne zobrazowania radarowe z wykorzystaniem dopasowanej trajektorii nośnika radaru", numer 2019/32/T/ST7/00120.

This dissertation was prepared thanks to the National Science Centre, Poland, under a scholarship in the Etiuda 7 program entitled "Interferometric Radar Imaging Using a Matched Radar Carrier Trajectory," number 2019/32/T/ST7/00120.

Acknowledgements

I would like to express my sincere gratitude to my supervisor, professor Piotr Samczyński, for his invaluable assistance, willingness to impart knowledge, and guidance on the path towards scientific excellence.

I would like to thank my colleagues from the Radar Techniques Research Group – working with each of you was a great pleasure and a wonderful experience.

I thank the Radar and Surveillance Systems Laboratory team in Pisa for giving me the opportunity to carry out a research internship, during which I learned a great deal.

A word of thanks goes to the students of the Warsaw University of Technology, whom I had the honour of teaching. Their curiosity and thirst for knowledge propelled me to continuous development.

Many thanks to Karol Abratkiewicz for his numerous comments on this dissertation, which helped shape its final form.

Special thanks go to the employees and experts of the National Science Centre, not only for their hard work for Polish science, but also for their substantive support and professional assistance at every stage of cooperation – from submitting the application to settling the grant.

No words can express my gratitude to my wife and children for their support and understanding during my work on this dissertation.

Streszczenie

Radarowe systemy obrazujące z syntetyczną aperturą montowane na platformach latających wykorzystywane są w wielu dziedzinach, między innymi przemyśle, nauce oraz obronności. Ze względu na wnikanie fal radiowych do wnętrza obiektów oraz możliwość pomiarów polarymetrycznych systemy radarowe pozwalają uzyskać dodatkowe informacje dotyczące obrazowanego obiektu lub obszaru w porównaniu z systemami optycznymi.

Obecnie stosowane radary z syntetyczną aperturą pozwalają uzyskiwać przede wszystkim zobrazowania dwuwymiarowe. Uzyskanie zobrazowania trójwymiarowego wymaga zastosowania co najmniej dwóch kanałów odbiorczych lub co najmniej dwóch równoległych przelotów platformy. Pierwsze rozwiązanie jest trudne do zastosowania na niewielkiej platformie latającej ze względu na konieczność uzyskania odległości między antenami większej, niż wymiary platformy, natomiast rozwiązanie drugie zwiększa czas pomiaru.

Jednym z kierunków rozwoju sensorów radarowych jest miniaturyzacja oraz zmniejszenie kosztu, a w szczególności ten drugi czynnik odpowiada za upowszechnienie się sensorów radarowych. W połączeniu ze zmniejszeniem się kosztu oraz upowszechnieniem bezzałogowych platform latających, w szczególności wielowirnikowców, w naturalny sposób istotnym obszarem badań stają się systemy radarowe montowane na tych platformach. Nowym aspektem niewystępującym w przypadku płatowców jest możliwość niemal dowolnego kształtowania trajektorii platformy radaru.

Niniejsza rozprawa opisuje metodę uzyskiwania trójwymiarowych zobrazowań radarowych z syntetyczną aperturą, z wykorzystaniem dostrajanej, nieprostoliniowej trajektorii platformy radaru. Najważniejszym elementem przedstawionej metody jest algorytm wyznaczania trajektorii uwzględniający model ruchu platformy radaru, dzięki któremu możliwe jest uzyskiwanie zobrazowań o zadanej jakości szybciej niż z wykorzystaniem trajektorii prostoliniowej. Zastosowano powszechnie stosowany w wielowirnikowcach i płatowcach model ruchu o ograniczonym zrywie oraz model planowania trasy oparty o punkty kontrolne. Prezentowana metoda pozwala na określenie trzech parametrów jakości zobrazowania – rozdzielczości, współczynnika sumarycznych listków bocznych oraz współczynnika maksymalnego listka bocznego. Pozwala również przyporządkować tym parametrom wagi w celu ich priorytetyzacji. Aby poprawić jakość uzyskiwanych zobrazowań stosowane jest dostrajanie trajektorii wykorzystujące minimalizację funkcji kosztu.

Prezentowana metoda może znaleźć zastosowanie tam, gdzie istotnym czynnikiem jest czas pomiaru, czyli przede wszystkim w przemyśle i obronności. Dzięki niej możliwe jest także dodanie możliwości obrazowania trójwymiarowego istniejącym systemom radarowym.

Słowa kluczowe: *radar, radar z syntetyczną aperturą, obrazowanie, bezzałogowy statek powietrzny, modelowanie ruchu*

Abstract

Airborne synthetic aperture radar imaging systems are used in many fields, including industry, science and defense. Due to the penetration of radio waves into objects and the possibility of polarimetric measurements, radar systems make it possible to obtain additional information about the imaged object or area compared to optical systems.

Currently used synthetic aperture radars allow obtaining primarily two-dimensional imaging. Obtaining three-dimensional imaging requires at least two receiver channels or at least two parallel flights of the platform. The first solution is difficult to apply on a small flying platform due to the need to obtain a distance between antennas larger than the dimensions of the platform, while the second solution increases measurement time.

One of the directions of radar sensor development is miniaturization and cost reduction, and the latter factor in particular is responsible for the proliferation of radar sensors. Combined with the decrease in cost and the proliferation of unmanned flying platforms, especially multi-rotors, radar systems mounted on these platforms naturally become an important area of research. A new aspect not found in fixed-wing platforms is the ability to shape the trajectory of the radar platform almost arbitrarily.

This dissertation describes a method for obtaining three-dimensional synthetic aperture radar imaging using a tunable, non-rectilinear radar platform trajectory. The most important element of the presented method is a trajectory determination algorithm that takes into account the motion model of the radar platform, thanks to which it is possible to obtain imaging of a given quality faster than using a rectilinear trajectory. A jerk limited motion model commonly used in multirotor and fixed-wing aircraft and a trajectory planning model based on waypoints were used. The presented method allows the determination of three imaging quality parameters – resolution, integrated side lobe ratio and peak side lobe ratio. It also allows assigning weights to these parameters for prioritization. To improve the quality of the resulting imaging, trajectory tuning using cost function minimization is applied.

The presented method can find application where measurement time is an important factor, that is, primarily in industry and defense. It also makes it possible to add 3D imaging capabilities to existing radar systems.

Keywords: *radar, synthetic aperture radar, imaging, unmanned aerial vehicle, motion modeling*

Contents

List of Acronyms

1D one-dimensional 23, 24
2D two-dimensional 17, 23, 24, 37, 41, 42, 48
3D three-dimensional 17–20, 27, 30, 33, 35, 37, 41, 48, 54
3DSAR Three-Dimensional Synthetic Aperture Radar 33–35, 83

CCD Charge-Coupled Device 17
CSAR Circular Synthetic Aperture Radar 19, 30

DBS Doppler Beam Sharpening 18
DoF Degree of Freedom 41

GNSS Global Navigation Satellite System 20

IC Imange Contrast 26
IE Image Entropy 26
INS Inertial Navigation System 20
InSAR Interferometric Synthetic Aperture Radar 18, 19, 24, 30
ISLR Integrated Side Lobe Ratio 26, 28, 37, 45

JPL Jet Propulsion Laboratory 18

LoS Line of Sight 37, 42

MBSAR Multi-Baseline Synthetic Aperture Radar 30
ML main lobe 28, 37

NASA National Aeronautics and Space Administration 18

PRF Pulse Repetition Frequency 28, 35, 43
PSF Point Spread Function 25, 37, 47
PSLR Peak Side Lobe Ratio 26, 28, 37, 45

RCS Radar Cross Section 23
ROI Region Of Interest 20, 28, 31, 33, 35–37, 41, 44, 54

SAR Synthetic Aperture Radar 17–20, 23, 24, 27, 33, 41, 48, 83

SL side lobe 28, 37, 45

SR Spatial Resolution 26, 27, 37

UAV Unmanned Aerial Vehicle 17, 19, 20, 36

List of Symbols

α	angular span
δ	radar image resolution
ε	dielectric constant
ϑ	spherical coordinates inclination angle
θ	antenna beam width
θ_{gl1}	angular distance between the main lobe and the first grating lobe
λ	wavelength
ρ	spherical coordinates radius
σ	Radar Cross Section (RCS)
τ	time delay
τ_p	pulse duration time
ϕ	signal phase
φ	spherical coordinates azimuth angle
χ_u	cross-correlation function
Ψ	grazing angle
Ψ_u	cross-ambiguity function

A	amplitude
A_e	antenna effective area
B	bandwidth
D	geometrical dimension
G	gain
ISLR	Integrated Side Lobe Ratio
L	synthetic aperture length
ML	main lobe
P	power
PSLR	Peak Side Lobe Ratio
Q	quality metric
Q_D	desired quality
R	range
SL	side lobe
W_S	swath width
a	acceleration
c	speed of light in vacuum
d	distance between synthetic aperture sampling points
d_{gl1}	distance between the main lobe and the first grating lobe
f_c	carrier frequency
f_d	Doppler frequency

f_r	Pulse Repetition Frequency
j	jerk
k	cost
p	position
p_x	pixel size
q	direction
s	matched filter response
s_t	transmitted signal
s_r	received signal
t	time
u	value
v	velocity
v_r	radial velocity
v_t	tangential velocity
w	weight

1. Introduction

Microwave and optical imaging are the most commonly used methods of obtaining images of the ground [1], structures [2, 3], objects [4], and humans [5]. Microwave approach typically uses an own illumination source and a coherent receiver [6]. On the contrary, the optical approach typically makes use of an external source of illumination (e.g., the Sun) and incoherent two-dimensional (2D) sensor (e.g. a Charge-Coupled Device (CCD) matrix) [7]. The existence of LIght Detection And Ranging (lidar)[1] must also be mentioned – it is an optical imaging method that uses own source of illumination (a Light Amplification by Stimulated Emission of Radiation (laser)) and a coherent light sensor [8].

The literature in the RAdio Detection And Ranging (radar)[2] field commonly presents microwave imaging as superior to the optical one and this claim is backed by the argument, that a radar can operate both day and night and in any weather conditions [6, 5, 9]. However, this is usually oversimplification. Independence from weather conditions is true only for selected frequencies, and operating in precipitation or night conditions is often impossible due to the limitations of the radar platform, especially for civilian applications [5]. Moreover lidar can work at night, just like radar [8], however it can not operate through clouds or smoke.

The actual advantages of microwave imaging are that the cross-range resolution (the resolution in the direction perpendicular to the line of sight) is independent of the radar distance from the object (in Synthetic Aperture Radar (SAR) imaging), the possibility of imaging the internal structure of the object or obtaining volumetric properties of it (when the wavelength can penetrate through the external layer) [6, 5].

In fact, microwave imaging is complementary to the optical one, as the two approaches usually provide a different kind of information [6]. There are applications where both of them are equally suitable, applications where one is preferred over another, and applications where both are needed in multisensor hyper-spectral systems [1, 10].

Typically, the SAR imaging sensor is placed on a moving platform, e.g., an airplane, a Unmanned Aerial Vehicle (UAV) or a satellite. Unlike optical sensors, which allow for 2D or three-dimensional (3D) imaging of a scene from a single platform position, a microwave sensor

[1] *lidar* is an acronym, but similarly to *radar* is uncapitalized in writing

[2] *radar* is an acronym, but is uncapitalized in writing

requires multiple sounding positions, which is achieved by the movement of the radar platform and leads to the creation of a synthetic aperture [11].

Typically, microwave and optical imaging (excluding lidar) provide 2D images. While this is sufficient for some applications, there are many areas where 3D imaging is of great value. In optical imaging this is achieved using lidar, while in radar imaging it is achieved using interferometry [12]. Interferometry requires two (or more) vertically positioned antennas on the radar platform or, alternatively, two (or more) flights at different altitudes [6]. The former approach requires a radar platform of considerable size, and the latter requires a very precise measurement of the platform's position. If the radar sensor is to be mounted on an UAV, the former becomes virtually impossible, and the latter is the only possibility of obtaining 3D SAR imaging.

The main challenge associated with the use of microwave sensors on a UAV is the long measurement time due to the need to perform multiple soundings. It should be emphasized that in the case of using a small and slow UAV, the time of measurement does not increase linearly with the increase in the number of sounding points, if an interruption is necessary due to the depletion of the energy source. This dependence is particularly noticeable when multiple interruptions for battery charging or replacement are needed. In military applications (reconnaissance), this problem is even more important because an interruption in the measurements can lead to a mission failure, and the capacity of the energy source imposes a rigid upper limit on the measurement time. A small UAV may have a maximum flight time of a few minutes, after which it must return to the base for battery replacement.

Another important, although less critical challenge is the amount of raw radar data obtained from the measurement. Depending on the system, this limitation can be imposed by memory capacity, communication link throughput, or the computational power of the on-board computer. A typical radar with a bandwidth of 1 GHz, a Pulse Repetition Frequency (PRF) of 1 kHz, and a distance range of 300 m produces 6 MB of data per second when using a 12-bit Analog to Digital Converter (ADC).

In order to remedy these problems, i.e., to reduce the time required for 3D imaging and to reduce the amount of data collected, the author proposes the use of a non-rectilinear trajectory of the radar platform. The initial knowledge of the Region Of Interest (ROI) dimensions and the imaging quality requirements allow one to determine a trajectory to obtain the imaging that is shorter than the one used in the traditional approach.

1.1. Motivation

The author's motivation to work in the field of 3D SAR imaging is the growing demand for these images and the insufficient effectiveness of existing interferometric methods using

airborne and satellite radar platforms. While working on radar data processing algorithms [13, 14, 15], the author noticed data coming from parts of the platform's trajectory that are not rectilinear – there is a change in altitude. Standard algorithms did not allow to obtain high-quality images from these data, however, the author started preliminary research on the possibility of obtaining 3D SAR images. At the same time, the continuous development of microwave techniques resulted in the emergence of smaller and more accessible radars operating in X [16], K [17], and higher bands [18], and passive radars [19] which can be mounted on UAV. This, and the rapidly growing popularity of UAVs, especially multirotors, which can fly on virtually any trajectory, allowed the author to see a technological gap to be filled. The author investigated the possibility of designing a specific trajectory to obtain an image of the ROI with a single-channel radar [20, 21]. This research was then carried on under an individual grant from the National Science Centre (NCN) and subsequently as a PhD thesis. Since 2018, the author has also worked on military applications of this method in the NATO SET-250 Multidimensional Radar Imaging research task group [22] and presented the potential for military application of his work at the NATO Early Career Scientist Event in Oslo, Norway in 2022.

1.2. Research Problem and Thesis

The aim of this thesis is to develop a novel method of obtaining 3D interferometric SAR images of a selected area. Contrary to contemporary 3D SAR imaging techniques that require either a radar equipped with two or more antennas in a single rectilinear (or circular) pass [23, 24, 25] or a radar with a single antenna in two or more passes [26, 27], the proposed new approach for 3D imaging is to use the radar with a single antenna in a single radar platform pass using an optimized flight trajectory.

The theses of this dissertation are as follows:

> It is possible to obtain three-dimensional radar imaging of a region of interest using a single single-channel radar and a non-rectilinear trajectory of the radar platform.

> It is possible to tune the trajectory of the radar platform to improve imaging quality or reduce sounding time, if the radar parameters, radar platform motion model, dimensions of the area of interest, and required imaging quality parameters are known.

It is assumed that the radar sensor and the radar platform allow one to achieve the required image quality. The thesis assumes that the trajectory is optimized with respect to a predefined cost function.

It should be noted that the more information there is about ROI, the better the trajectory can be adjusted. However, having full ROI information precludes the need for imaging. In this work, the initial information should be understood as approximate geometric dimensions and position.

1.3. Original Contributions

The author's innovative achievements are as follows:

— Development of an algorithm for determining the trajectory of a radar platform with a single-channel radar sensor to obtain 3D imaging [20].

— Development of a method of trajectory tuning in order to improve the imaging parameters, taking into account the motion model of the radar platform [28, 29].

— Development of an open-source complex 3D SAR simulator [30].

— Verification of the developed method on simulated and experimental data [29].

1.4. Outline

The dissertation is divided into 6 chapters, including this one (Introduction). Chapter 2 begins by introducing the coordinate systems used in this dissertation. This is followed by the theoretical background of the issues covered in this dissertation, from the basics of radar operation, to SAR, including imaging issues such as Point Spread Function (PSF), grating lobes, side lobes, and measures of imaging quality. The most popular methods for obtaining imaging are also presented. The rest of the chapter presents the theoretical foundations of Interferometric Synthetic Aperture Radar (InSAR). Chapter 2 concludes with a presentation of optimization issues.

Introduction to Chapter 3 is the history of development of SAR technique, which led to the work on 3D imaging. The remainder of the chapter presents existing approaches to obtaining 3D SAR imagery, ranging from traditional ones such as Circular Synthetic Aperture Radar (CSAR) or Multi-Baseline Synthetic Aperture Radar (MBSAR), to actually non-rectilinear trajectories such as HAT-manouver or random trajectories. The advantages and disadvantages of the presented approaches are presented, which introduces the next chapter.

Chapter 4 is the main part of the dissertation, where the 3D SAR method is described. It starts by presenting the geometry of the 3D imaging and then describes the requirements of the imaging quality with emphasis on resolution. The next section presents the next steps of the developed method: determining the shape of the SA, distributing the waypoints on the synthetic aperture surface, and determining the PSF, taking into account the rectilinear segmented and jerk-limited motion model. Then, the process of tuning the trajectory by moving the waypoints

is presented. In the next section, a method for optimizing the tuning process with respect to computational complexity is briefly presented. The chapter concludes with the presentation of methods for obtaining 3D SAR images and target reconstruction.

Chapter 5 presents the results of a simulation study for an example target, followed by the experimental results for comparison. The results are commented in the context of the assumed requirements and the differences between theoretical and experimental studies.

The final Chapter 6 of the dissertation serves as a summary of the main achievements, which are also presented in the context of the experimental results. The chapter ends by outlining a direction for further work.

1.5. Conclusions

This dissertation presents an algorithm that allows one to use the knowledge of the radar platform motion model to determine the trajectory allowing to obtain three-dimensional imaging of ROI with assumed quality in a shorter time than the previously used 3D SAR methods. Detailed presentation of the method is accompanied by the results of simulation and real-world tests, confirming the applicability of the method.

2. Theoretical Background

This chapter presents the established theory in the dissertation area. The principles of radar, synthetic aperture radar, and imaging techniques are briefly presented. Optimization problem is also illustrated, as it is relevant to the dissertation topic.

2.1. Coordinate System

Both Cartesian and spherical coordinate systems are used through this dissertation, according to [31] as shown in Figure 2.1. It is assumed that x and y axes are parallel to the

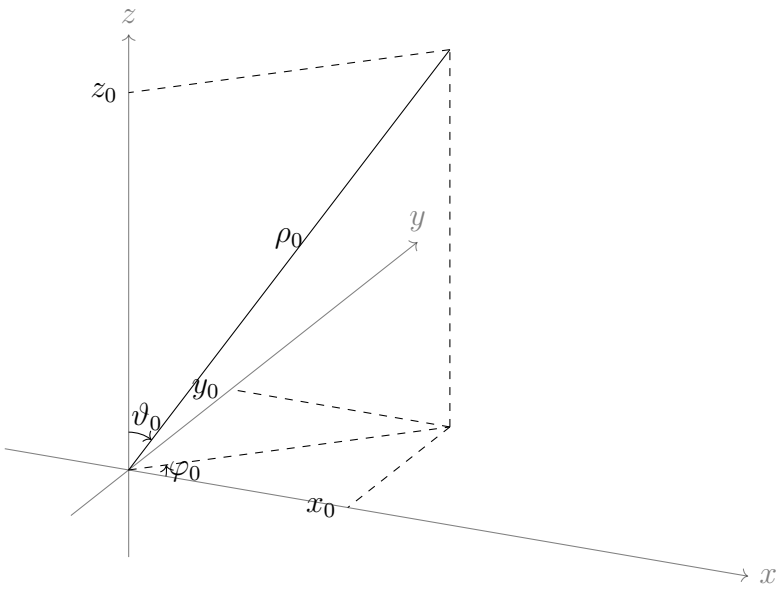

Figure 2.1. Coordinate system used through this dissertation.

ground plane and z axis is normal to the ground plane. The Cartesian and spherical coordinates are linked in the following way:

$$\begin{aligned} x &= \rho \sin\vartheta \cos\varphi, \\ y &= \rho \sin\vartheta \sin\varphi, \\ z &= \rho \cos\vartheta, \end{aligned} \tag{2.1}$$

and

$$\begin{aligned}\rho &= \sqrt{x^2+y^2+z^2},\\ \theta &= \arctan\frac{\sqrt{x^2+y^2}}{z},\\ \varphi &= \arctan\frac{y}{x},\end{aligned} \tag{2.2}$$

where $\arctan\left(\frac{\cdot}{\cdot}\right)$ is a two-argument, four-quadrant arctangent. It is assumed that a target is located at the origin $(0,0,0)$. If 2D coordinates are required locally, x, y, and ρ, φ are used and $z = 0$ and $\theta = \frac{\pi}{2}$ is assumed.

2.2. Radar Principles

Merrill Skolnik defines radar as *an electromagnetic sensor for the detection and location of reflecting objects* [6]. This is a rephrased expansion of the word *radar*, which is an acronym – **Ra**dio **D**etection **a**nd **R**anging. Radar uses a radio signal to detect the presence of a reflecting object and indirectly estimate its range R by measuring the round-trip delay of the signal τ_R:

$$R = \frac{c\tau_R}{2}, \tag{2.3}$$

where c is the speed of light. These short and concise definitions describe what the radar was designed and primarily used for, however they do not show a wide range of possibilities the radar offers. A typical radar geometry is presented in Figure 2.2. It must be stressed that a

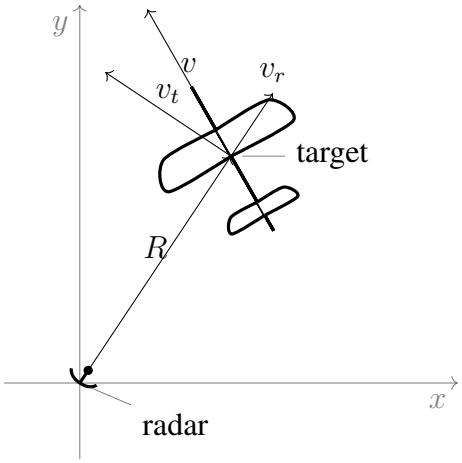

Figure 2.2. Radar geometry.

single stationary radar sensor is not capable of estimating the position of the target, but only the range.

Apart from the range, another important target parameter can be estimated – radial velocity v_r, which is the component of the target velocity parallel to the line of sight, directed away from the radar. It is derived from the Doppler frequency shift f_d:

$$f_d = \frac{-2v_r}{\lambda}, \tag{2.4}$$

where λ is wavelength. Radial velocity component is the only information of the target velocity that a single radar sensor can obtain (the tangential velocity component v_t cannot be measured). If the radial velocity of the target is non-zero, the returned radar signal in the baseband takes the form:

$$s_r(t) = A(t)s_t\left(t-\tau\right)\exp\left(j4\pi f_c\left(t-\tau\right)\right)\exp\left(j2\pi f_d t\right), \tag{2.5}$$

where $A(t)$ denotes signal amplitude factor (which does not play an important role in the following part of the dissertation), $s_t\left(t-\tau\right)\exp\left(j4\pi f_c\left(t-\tau\right)\right)$ is the delayed copy of the transmitted signal and $\exp\left(j2\pi f_d t\right)$ is the Doppler phase term. This formula does not impose any restrictions on the transmitted signal s_t; in the remainder of the dissertation, unless otherwise noted, all considerations are independent of the transmitted signal type. The radar can estimate f_d and then, using (2.4), v_r. The possibility of estimation of the Doppler frequency shift not only allows for velocity estimation, but also provides the possibility of separating moving and stationary targets, even if they appear at the same range. In air surveillance radars, this leads to clutter suppression techniques and in SAR to Moving Target Indication (MTI) [32, 33].

In (2.5), the factor $A(t)$ represents the fact that only a portion of the transmitted energy reaches the target and only a portion of that energy is reflected back to the radar. This leads to another target parameter – the Radar Cross Section (RCS). It describes the equivalent target reflective area in m^2 and has the symbol σ. It is present in the radar equation [6]:

$$P_r = \frac{P_t G_t}{4\pi R^2}\frac{\sigma}{4\pi R^2}A_e, \tag{2.6}$$

where P_r is the received power and the right side is a product of three factors: first is the power density at range R when the transmitted power is P_t and transmitter gain is G_t, second is the power reflected back to the transmitter, and third is the receiving antenna effective area A_e.

Apart from the range, radial velocity and the RCS other target parameters can be also estimated using special techniques and assuming some a priori knowledge of the object, such as material type, humidity, temperature, and many others [34, 35, 36, 37, 38].

The amount of information that can be obtained about the object is proportional to the signal bandwidth. The higher the signal bandwidth, the more precise and rich the information is, in particular, the distance between distinguishable scatterers is smaller.

2.3. Synthetic Aperture Radar

The previous subsection describes the basic configuration of a stationary radar. Placing the radar on a moving platform greatly increases its applications, one of which is SAR. A SAR geometry is presented in Figure 2.3 and Figure 2.4. While a single stationary radar sensor

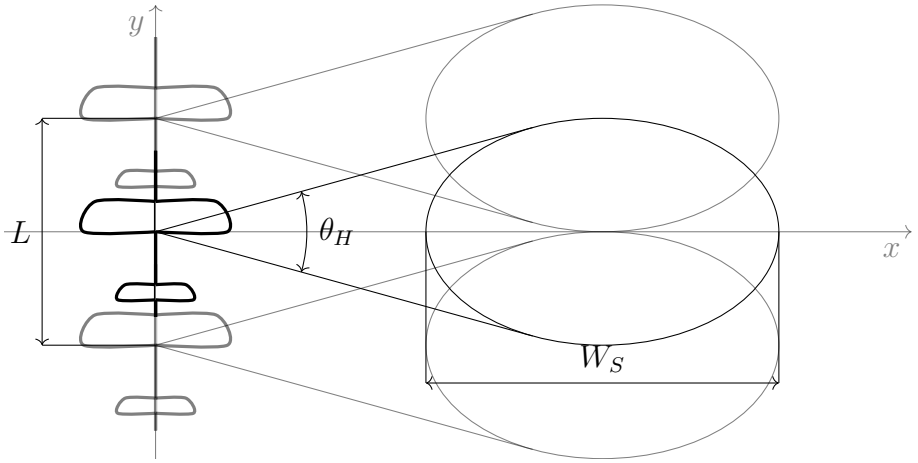

Figure 2.3. SAR geometry (top view).

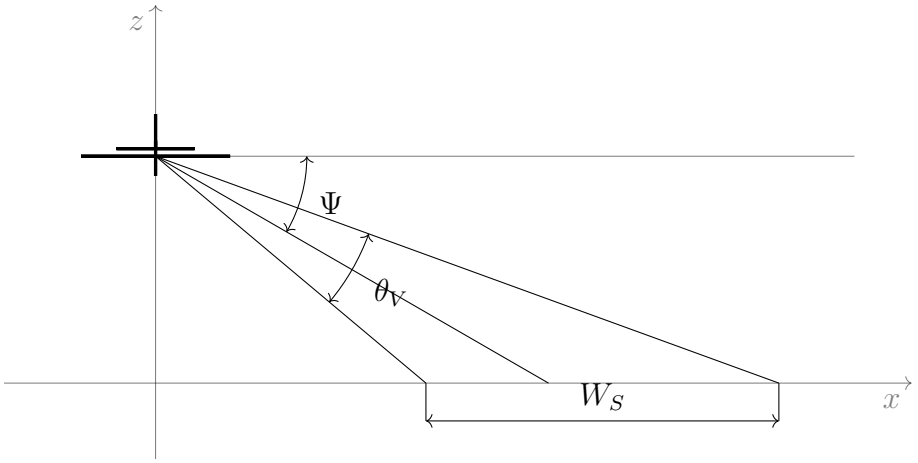

Figure 2.4. SAR geometry (side view).

produces a one-dimensional (1D) signal, called a range profile (reflectivity versus range). Using a 1D array of radar sensors (aperture) leads to a 2D signal, called a range-cross-range profile (reflectivity versus range and platform position). If the target is stationary and does not change its properties in time, the array can be formed through moving the sensor along a line (synthetic aperture). In such a situation, the sensor position is uniquely related to time, and the signal is called a range-time profile. In SAR the 2D signal is sometimes referred to as a range-Doppler profile [39], however it must be stressed that not the Doppler effect and not even the relative velocity between the radar platform and the target is needed to obtain a 2D image [11]. In fact, it can even be the source of errors if not accounted for in very high resolution imaging [40, 41].

If the consecutive positions of the radar platform are known, it is possible to obtain a two-dimensional imaging of the target. An example of such an imaging is shown in Figure 2.5 [14], and for reference, an optical imaging of the same area in Figure 2.6 is also provided. On

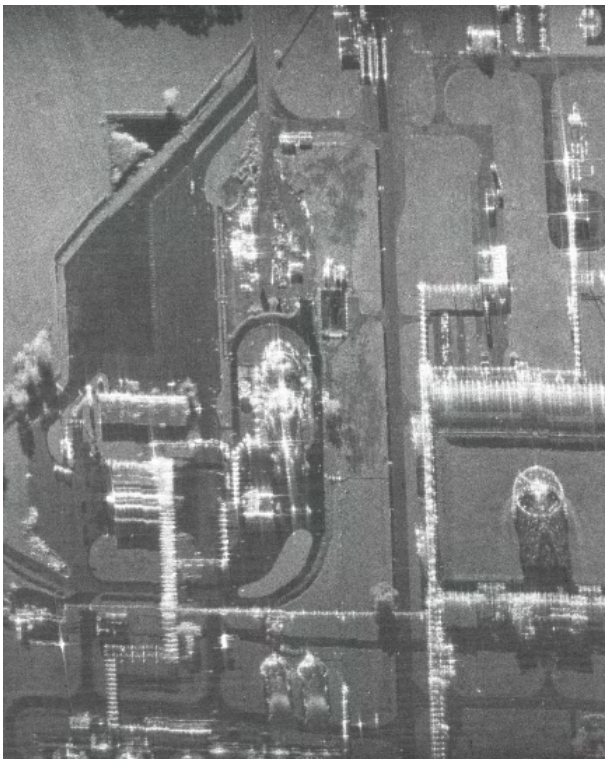

Figure 2.5. SAR image of a selected region.

Figure 2.6. Photographic image of the same region. Image ©2022 CNES/Airbus, MGGP Aero, Maxar Technologies, Map data ©2022 Google.

the example of this imaging, important features of SAR imaging can be observed:

— Elements reflecting electromagnetic radiation at the radar carrier frequency are more strongly visible, for example, the most prominent elements of the pipelines are the supporting structures.

— The internal structure of some objects is visible, for example, tanks located in the central, lower, and right parts of the image.

The principles of SAR imaging are presented in detail in the following subsections.

2.4. Point Spread Function

PSF is the response of the imaging system to a point target. In the case of SAR, it is the image that is obtained when observing a material point target. An example of a PSF of a 2D SAR system is presented in Figure 2.7. The shape of the PSF along range direction depends

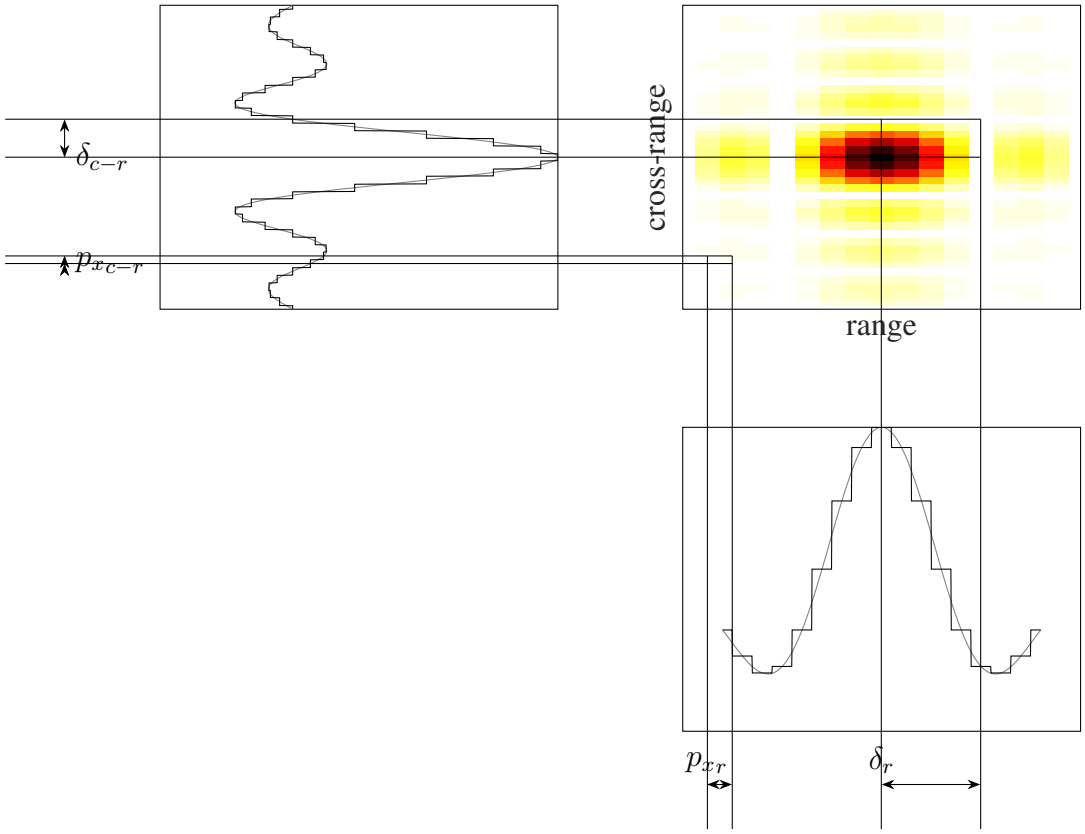

Figure 2.7. 2D SAR PSF.

solely on the bandwidth of the radar, while the shape of the PSF along the cross-range direction depends on the shape of the synthetic aperture (in the case of 2D SAR – synthetic aperture length – L on Figure 2.3).

Considering a single radar sensor (an aperture consisting of one point – one antenna position) the PSF is a one-dimensional function given by the formula [6]:

$$s_1(\boldsymbol{p}) = \exp\left(j4\pi\frac{r}{\lambda}\right)\operatorname{sinc}\left(\frac{r}{\frac{c}{2B}}\right), \tag{2.7}$$

where λ is wavelength, c is speed of light in vacuum, B is bandwidth and $r = |\boldsymbol{p}-\boldsymbol{p_a}|-|\boldsymbol{p_t}-\boldsymbol{p_a}|$ is the difference between the distance from the antenna position $\boldsymbol{p_a}$ to the point $\mathbf{p}$ and the distance from the antenna position to the target position $\boldsymbol{p_t}$. This response form is valid for large time-bandwidth products $BT \gtrsim 100$ [11], where T is the pulse length.

If the synthetic aperture consists of N points, the response is a coherent sum of responses from each of those points [42]:

$$s(\boldsymbol{p}) = \sum_{n=1}^{n=N}\exp\left(j2\pi\frac{r_n}{\lambda}\right)\operatorname{sinc}\left(\frac{r_n}{\frac{c}{2B}}\right), \tag{2.8}$$

where $r_n = |\boldsymbol{p}-\boldsymbol{p_{an}}| - |\boldsymbol{p_t}-\boldsymbol{p_{an}}|$ is the difference between the distance from the nth antenna position $\boldsymbol{p_{an}}$ to the point $\mathbf{p}$ and the distance from the nth antenna position to the target position $\boldsymbol{p_t}$.

2.5. 3D Point Spread Function

In the previous section, a two-dimensional PSF is presented. However, since the essence of this work is 3D imaging, it is necessary to introduce the concept of 3D PSF. Figure 2.8 (a) shows a 3D view of a PSF of a traditional two-dimensional SAR (with a rectilinear horizontal trajectory). It can be seen that the PSF does not change along the vertical axis, as the traditional SAR has no resolution in the vertical direction. Figure 2.8 (b) shows a 3D view of a PSF of a 3D SAR (with two-dimensional synthetic aperture). It can be seen that the horizontal cross sections

(**a**) (**b**)

Figure 2.8. SAR PSF in 3D: (**a**) 2D SAR. (**b**) 3D SAR.

of these two PSFs are the same (see Figure 2.7). Since the topic of this work is 3D imaging using a non-rectilinear trajectory, and the shape of the trajectory determines the shape of the PSF in the cross-range direction, in the remainder of this dissertation, only the cross-section of 3D PSF in cross-range plane (perpendicular to the range) is presented for readability, as shown in Figure 2.9. Additionally, the $\cdot_{c-r}$ subscript is omitted. The shape of the PSF in the range

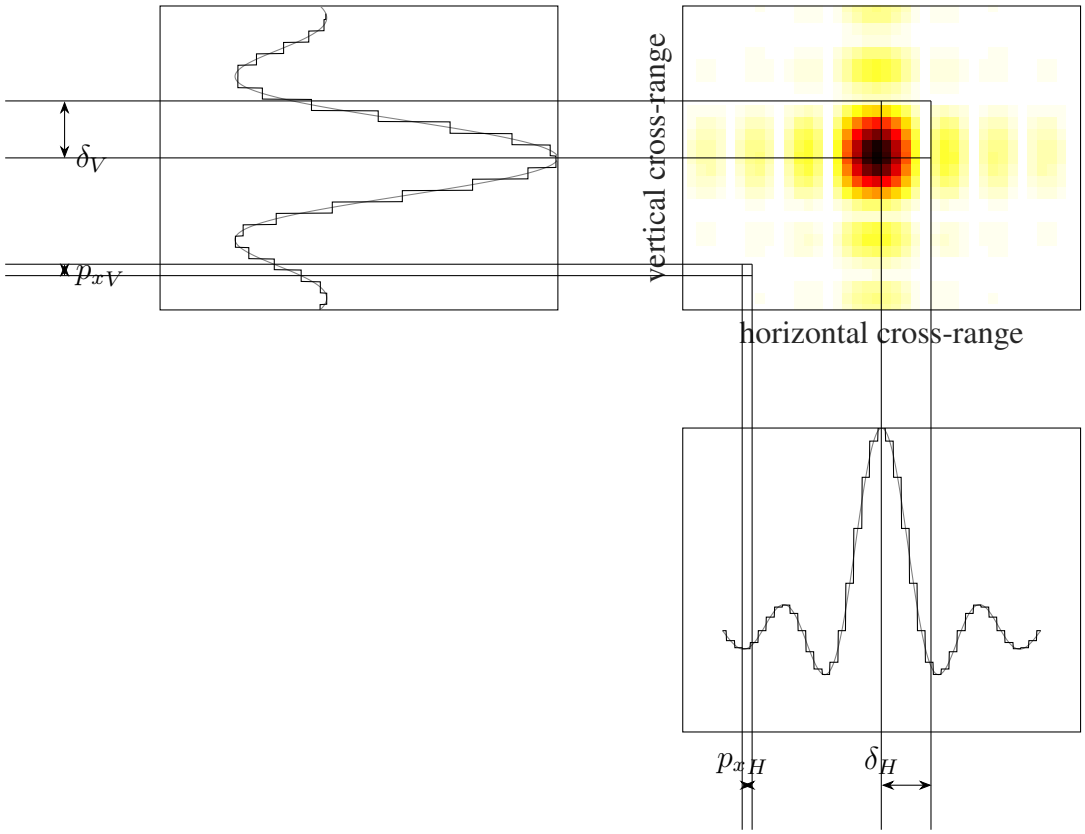

Figure 2.9. 3D SAR PSF Cross-section in cross-range plane.

direction depends primarily on the radar bandwidth, a parameter considered constant in this work.

2.6. SAR Image Formation

The PSF described in the previous subsection applies to the situation where the target is a single reflecting point. As with the transition from (2.7) to (2.8), the imaging of a target consisting of M points is the coherent sum of the imaging of each of these points:

$$s(\boldsymbol{p}) = \sum_{m=1}^{m=M} \sum_{n=1}^{n=N} \exp\left(j4\pi \frac{r_{mn}}{\lambda}\right) \operatorname{sinc}\left(\frac{r_{mn}}{\frac{c}{2B}}\right), \tag{2.9}$$

where $r_{mn} = |\boldsymbol{p} - \boldsymbol{p_{an}}| - |\boldsymbol{p_{tm}} - \boldsymbol{p_{an}}|$ is the difference between the distance from the nth antenna position $\boldsymbol{p_{an}}$ to the point $\mathbf{p}$ and the distance from the nth antenna position to the mth scatterer position $\boldsymbol{p_{tm}}$.

Equation (2.9) describes the SAR imaging based on the information of the positions of the reflecting points. Swapping the order of the summations, the following equation is obtained:

$$s(\boldsymbol{p}) = \sum_{n=1}^{n=N} \sum_{m=1}^{m=M} \exp\left(j4\pi \frac{r_{mn}}{\lambda}\right) \operatorname{sinc}\left(\frac{r_{mn}}{\frac{c}{2B}}\right). \tag{2.10}$$

Given that (2.7) describes the one-dimensional range profile obtained by range compression from (2.5), which can be written as a function of distance $s_r(r)$. As a result, substituting this form into (2.10) yields the formula:

$$s(\boldsymbol{p}) = \sum_{n=1}^{n=N} \exp\left(-j2\pi \frac{r_n}{\lambda}\right) s_r(r_n), \tag{2.11}$$

where $r_n = |\boldsymbol{p} - \boldsymbol{p_{an}}|$. This formula describes conceptually the simplest tomography-derived Back Projection Algorithm (BPA) imaging method [43]. This method has two important features:

1. It provides the best quality imaging from the given data, as it contains no simplifications or approximations.
2. It has a high computational complexity of $O(N^3)$ [44] without simplifications.

There are other SAR imaging methods, the most popular of which is the range-Doppler algorithm, but it is designed for obtaining two-dimensional imaging [6]. In this work, the BPA method is used to obtain imaging.

2.7. Grating Lobes and Side Lobes

In the previous section, Figure 2.7 shows the PSF of the SAR system for the ideal case – effects of synthetic aperture sampling are omitted (the PRF is infinite). The side lobes of the sinc function resulting directly from the radar principle can be seen. In the real situation, when the PRF is finite, grating lobes may appear in addition to the main lobe.

2.7.1. One-Dimensional aperture

In a typical 2D SAR, the synthetic aperture is a straight line that is uniformly sampled in space. With sampling comes the phenomenon of grating lobes. If the distance between successive sampling points is defined as

$$d = \frac{v}{f_r}, \tag{2.12}$$

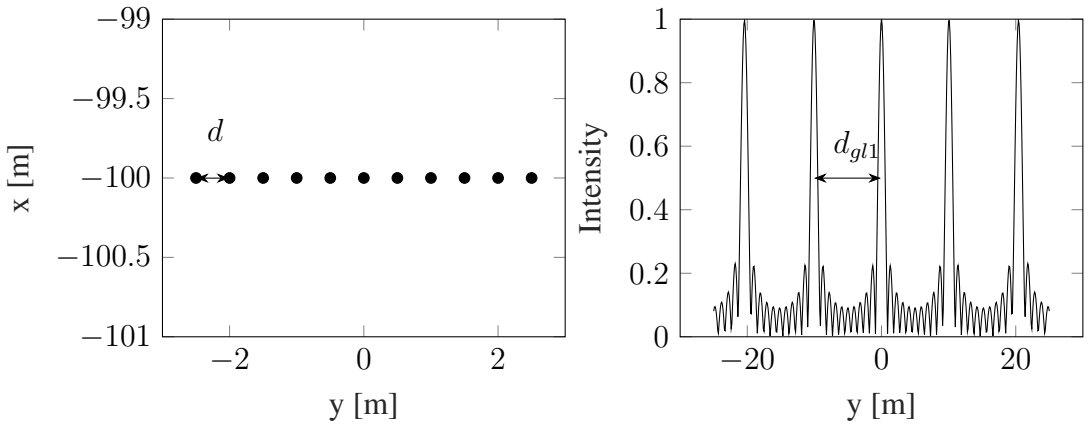

(a) **(b)**

Figure 2.10. Grating lobes. **(a)** Sampling points (Trajectory), **(b)** 2D cross-range cross-section of 3D PSF.

where v is the radar platform along-track velocity and f_r is the PRF, then the azimuthal cross-section of the PSF takes the form shown in Figure 2.10, and the distance between the main lobe and the first grating lobe is

$$d_{gl1} = \frac{\lambda R}{d}, \tag{2.13}$$

and the angular distance is

$$\sin\theta_{gl1} = \frac{\lambda}{d}. \tag{2.14}$$

It must be noted that usually in typical SAR imaging the parameters are chosen so that the phenomenon of grating lobes does not affect the imaging – the first grating lobe is outside the imaging area. As per [6], this is ensured when the following requirement for spatial spacing between synthetic aperture points is not fulfilled

$$d < \frac{\lambda}{1 + |\sin\theta|}, \tag{2.15}$$

where θ is the observation angle. If the sampling of the synthetic aperture is not uniform, the formulas (2.13) and (2.14) do not apply. There are side lobes, whose position cannot be determined analytically and to know this position, it is necessary to determine the PSF. Random sampling of the synthetic aperture reduces the grating lobes at the expense of increasing the Integrated Side Lobe Ratio (ISLR), as presented in Figure 2.11.

2.7.2. Two-Dimensional Aperture

For a 2D synthetic aperture, formulas (2.13) and (2.14) remain valid. In the case of uniform sampling, grating lobes are present in the imaging as shown in Figure 2.12, in the case of

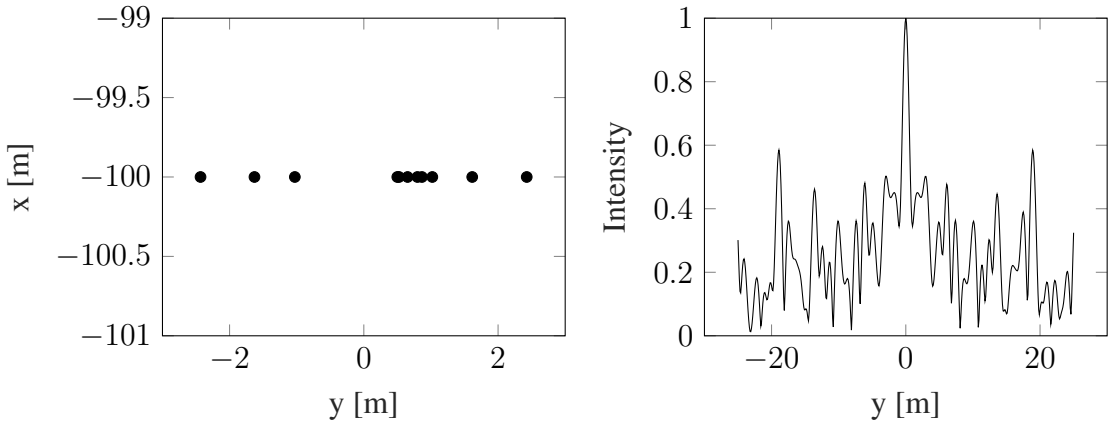

(a) **(b)**

Figure 2.11. Side lobes with non-uniform sampling. **(a)** Sampling points (Trajectory), **(b)** 2D cross-range cross-section of 3D PSF.

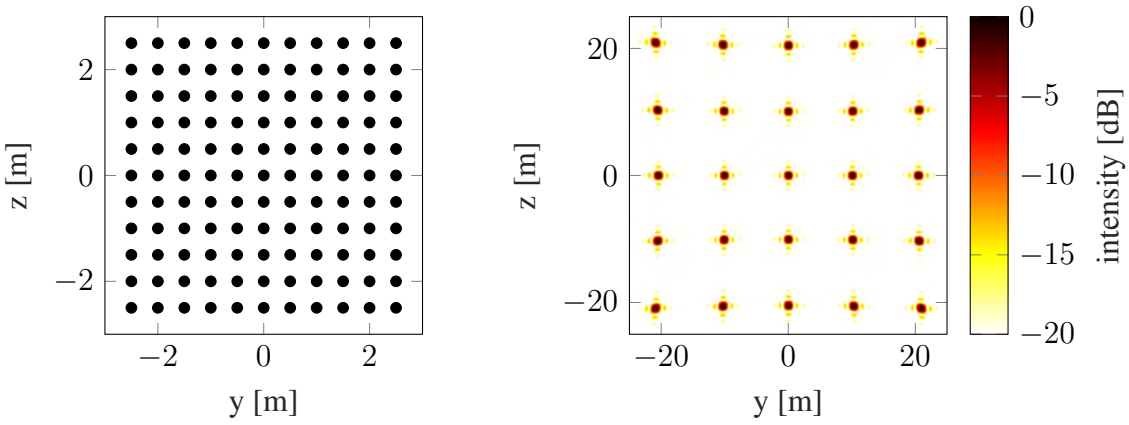

(a) **(b)**

Figure 2.12. Side lobes with uniform sampling. **(a)** Sampling points (Trajectory), **(b)** 2D cross-range cross-section of 3D PSF.

non-uniform sampling, side lobes are seen showing some regularity (Figure 2.13), and in the case of random sampling, side lobes show no regularity (Figure 2.14). These observations are analogous to those of a 1D aperture – decreasing the regularity in synthetic aperture spatial sampling decreases the peak side lobe value. For reference, sample 3D PSFs are provided in Figure 2.15. Note that 2D cross-sections provided assume zero bandwidth to exclude range resolution impact, while 3D PSFs assume bandwidth of $300\,\mathrm{MHz}$.

2.8. Image Quality Metrics

SAR imaging quality measures for 3D images can generally be inherited from traditional 2D SAR. The term *quality* regarding SAR images is rather vague. It is most commonly understood as *resolution*, but the resolution (2D or 3D) does not describe the image quality precisely

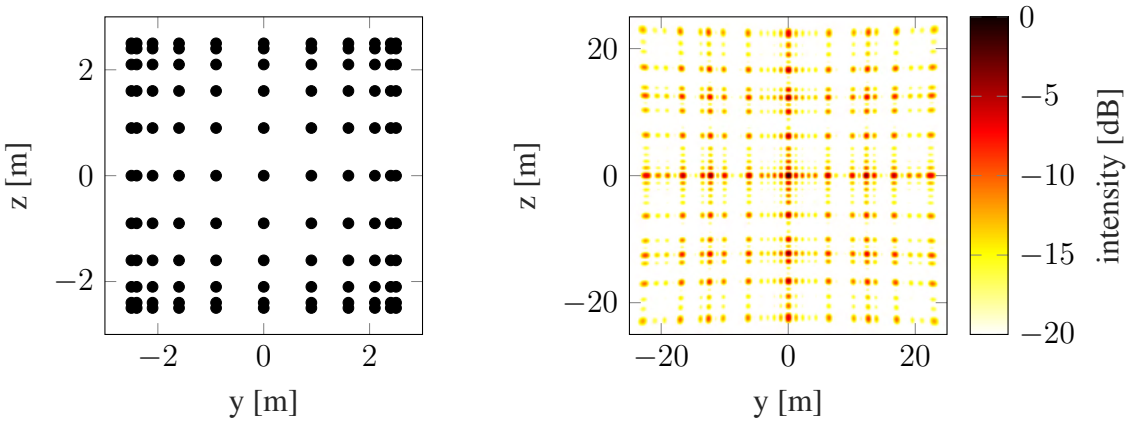

Figure 2.13. Side lobes with uneven sampling. **(a)** Sampling points (Trajectory), **(b)** 2D cross-range cross-section of 3D PSF.

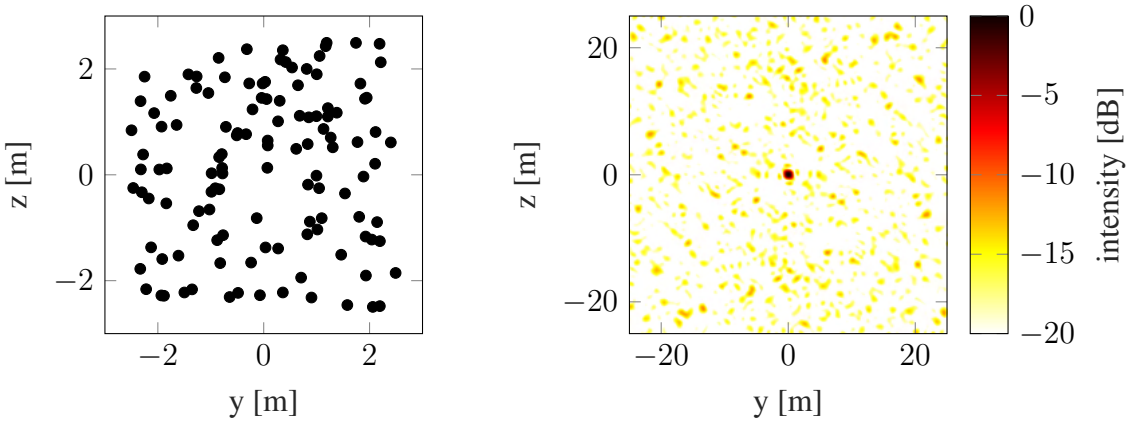

Figure 2.14. Side lobes with random sampling. **(a)** Sampling points (Trajectory), **(b)** 2D cross-range cross-section of 3D PSF.

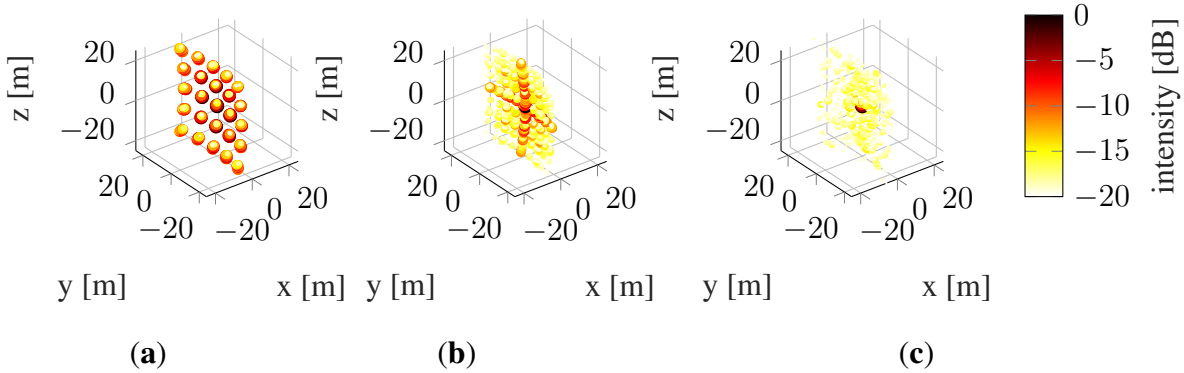

Figure 2.15. 3D PSF example for side lobe demonstration. **(a)** Uniform sampling, **(b)** uneven sampling, **(c)** random sampling. Non-zero bandwidth is assumed for image readability.

enough. In the 80's, as SAR systems were gaining popularity, there were works carried out to define common quality measures [45, 46].

The term *quality* is defined in Cambridge Dictionary as *how good or bad something is* [47]. A radar image can not be arbitrarily *good* or *bad*, but it can be *good* or *bad* for specific purposes. This implies that the quality of an image should be defined with respect to the intended use of that image, however the spectrum of potential usages is very broad and a universal quality metric is needed.

The resolution is not equal to the image quality. As the reflectivity of a scatterer is a complex number, the side lobes can add constructively, distorting the image. Another important thing is that real objects are not formed of point scatterers, but are continuous.

A good quality measure must be, first of all, objective – meaning that it must have a numerical value that can be unambiguously calculated. Most popular objective quality measures include [48]:

1. Spatial Resolution (SR) [49, 50]
2. Peak Side Lobe Ratio (PSLR) [51, 52]
3. ISLR [53, 54, 55, 50]
4. Imange Contrast (IC) [56, 57, 58]
5. Image Entropy (IE) [56, 59, 58, 60, 61]

The parameters listed above can be divided into two groups: SR, PSLR, and ISLR depend primarily on the radar parameters and the shape of the aperture (radar platform trajectory), while IC and IE are affected primarily by the imaging procedures and the accuracy of the radar platform position estimation.

For the record, there are also subjective quality measures that is neither described nor discussed in this dissertation [45]:

1. Image Artifacts
2. Geometric Distortion
3. Image Intensity Uniformity

2.8.1. Spatial Resolution

SR is the most common quality measure of SAR images. It determines how far apart two scatterers must be in order to be distinguishable. In 2D SAR, there is a range and a cross-range resolution, as shown in Figure 2.7. Considering a SAR image of a single scatterer, both range and cross-range cross-sections resemble a sinc function, which is the envelope of a matched filter response [6]. Despite their similarity, the processes responsible for them are different.

Range resolution depends solely on the radar bandwidth and is defined as [62]

$$\delta_r = \frac{c}{2B}, \tag{2.16}$$

where B is the radar bandwidth and c is the speed of light. The width of main lobe is $\frac{c}{B}$, which results in resolution of $\frac{c}{2B}$. First side lobe height is -13,3 dB [63].

Cross-range resolution is defined as

$$\delta_{c-r} = \frac{\lambda R_0}{2L} = \frac{\lambda}{4} \frac{1}{\tan \frac{\alpha}{2}}, \tag{2.17}$$

where R_0 is the distance from synthetic aperture center to imaging region center and L is synthetic aperture length, α is the angular span of the synthetic aperture (observation angle). In 2D SAR imaging there is range dimension and cross-range dimension, as shown in Figure 2.7, while in 3D SAR imaging there is one range dimension and two cross-range dimensions, usually horizontal cross-range and vertical cross-range.

Apart from the resolution, SAR images have one more parameter – pixel size. For BPA the pixel size is arbitrary, while for the range-Doppler algorithm, the pixel size depends on the radar and scenario parameters. Range pixel size for range-Doppler algorithm is defined as:

$$p_{xr} = \frac{c}{2f_d}, \tag{2.18}$$

where f_d is the range sampling rate. Radar cross-range pixel size for range-Doppler algorithm is defined as:

$$p_{xc-r} = \frac{v}{f_r}, \tag{2.19}$$

where v is the cross-range velocity of the platform and f_r is the PRF or cross-range sampling rate. That means p_{xc-r} is equal to the spatial distance between synthetic aperture points.

2.8.2. Peak Side Lobe Ratio

PSLR describes how the highest side lobe level relates to the main lobe level. It can be interpreted as a maximum energy of a scatterer that can be covered by a side lobe of a stronger scatterer.

The one–dimensional PSLR in decibels is given by [50]:

$$\mathrm{PSLR} = 20 \log_{10} \left(\frac{\max\limits_{n \in \mathrm{SL}} [A(n)]}{\max\limits_{n \in \mathrm{ML}} [A(n)]} \right), \tag{2.20}$$

where $n \in \mathrm{SL}$ denotes points in the side lobe, and $n \in \mathrm{ML}$ denotes points in the main lobe.

In the literature, various authors provide various definitions of the side lobe region taken for integration [48]. In [62], it is eqal to ten times the main lobe width, in [50], to six times the main lobe width and in [54], to 128 samples. As none of these approaches can be considered objective or intuitive, in this work, the side lobe region is defined as the whole imaging region (ROI) outside the main lobe. Such an approach ensures that the highest side lobe is always considered for image quality assessment. Main lobe and side lobe regions for a 1D case are depicted in Figure 2.16.

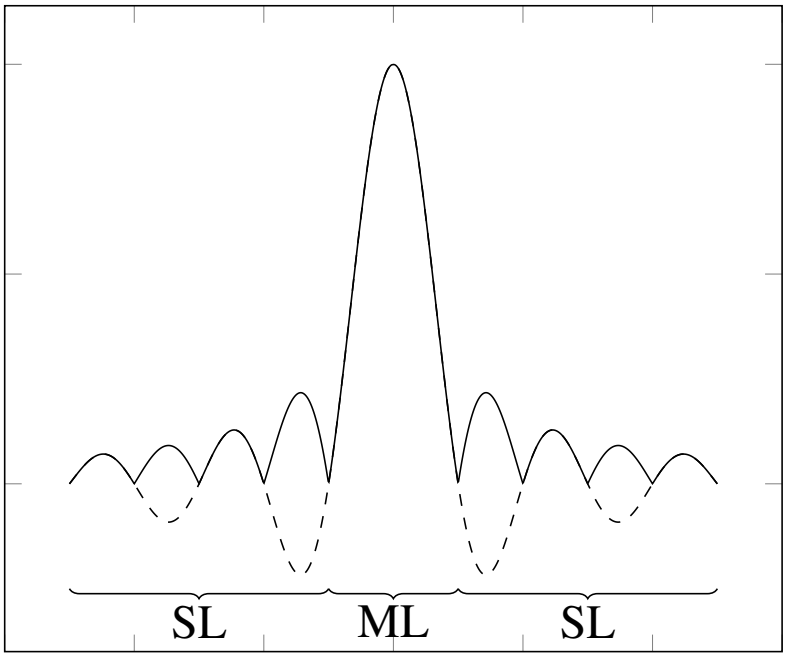

Figure 2.16. The main lobe (ML) and side lobe (SL) regions defined for ISLR and PSLR calculation.

2.8.3. Integrated Side Lobe Ratio

ISLR describes the amount of energy in the side lobes related to the amount of energy in the main lobe.

The one–dimensional ISLR is decibels given by [50]:

$$\mathrm{ISLR} = 20 \log_{10} \left(\frac{\sum\limits_{n \in \mathrm{SL}} [A(n)]}{\sum\limits_{n \in \mathrm{ML}} [A(n)]} \right), \tag{2.21}$$

where $n \in \mathrm{SL}$ denotes points in the side lobe, and $n \in \mathrm{ML}$ denotes points in the main lobe. The side lobe region for ISLR calculation is defined in the same way as for PSLR . Obviously this leads to the situation, where ISLR depends on the ROI size and shape, but this is an appropriate behaviour, as the ISLR is used mainly to compare the outcome of consecutive steps of the optimization process.

High PSLR and low ISLR result in a low probability of an echo from a scatterer being covered by a side lobe from an echo of another scatterer, but even relatively strong scatterers have a chance of being covered. On the other hand low PSLR and high ISLR result in a high probability of a very weak scatterer of being covered.

2.8.4. Contrast

Contrast is used mostly in the autofocusing[1] algorithm and is defined as [56]:

$$IC = \frac{\sigma_I}{\mu_I}, \tag{2.22}$$

where $\mu_I \equiv \mathrm{A}(I)$ is the average (mean) pixel intensity, $\sigma_I \equiv \sqrt{\mathrm{A}((I-\mu_I)^2)}$ is standard deviation of image pixel intensity, and $\mathrm{A}(\cdot)$ is the mean operator.

2.8.5. Entropy

Entropy is also used in the autofocusing algorithm as an optimization criterion and is defined as [56]:

$$E = -\sum_x \sum_y \sum_z \overline{I(x,y,z)} \log\Big(\overline{I(x,y,z)}\Big), \tag{2.23}$$

where $\overline{I(x,y,z)} = \frac{|I(x,y,z)|^2}{\mathrm{A}(|I|^2)}$.

2.9. Radar Interferometry

In Section 2.3, it is pointed out that the traditional SAR that relies on moving the radar on a platform along a straight line produces a 2D imaging that does not have information about the height of points above the imaging plane. The simplest way to obtain such information is to take two images from two different radar heights above the imaging plane, and then determine the height based on the phase difference. Naturally, the phase measurement requires the sensor to be coherent. This technique is called InSAR [65, 66]. InSAR can be implemented in two ways: using a radar with two receiving antennas (Figure 2.17 (a)) or two separate flights of the platform with a single receiving antenna (Figure 2.17 (b)). The latest 3D Inverse Synthetic Aperture Radar (ISAR) imaging research also uses a constellation of simultaneously flying drones, with one equipped with a transmitter and a receiver, and the others with a receiver only [67].

It must be noted that generally in radar interferometry one transmitter and two receivers are used. However, taking into account the specific geometry used in this dissertation, for simplicity, it is assumed that there are two transmit and receive sensors (or two positions of one transmit and receive sensor). To simplify the description, one point scatterer and two sensors are assumed as in Figure 2.18.

[1] Autofocusing is a technique of compensating the unknown components of the radar platform motion in SAR by using image contrast maximization [64].

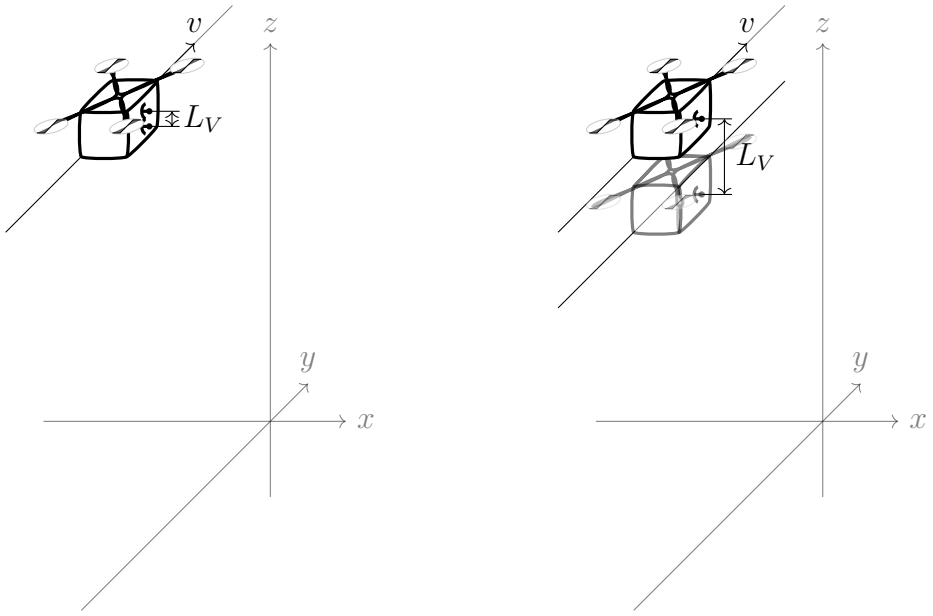

(**a**) (**b**)

Figure 2.17. Traditional InSAR geometries: (**a**) Dual antenna, single pass. (**b**) Single antenna, dual pass. v denotes the direction of motion of the radar platform, L_V is the baseline.

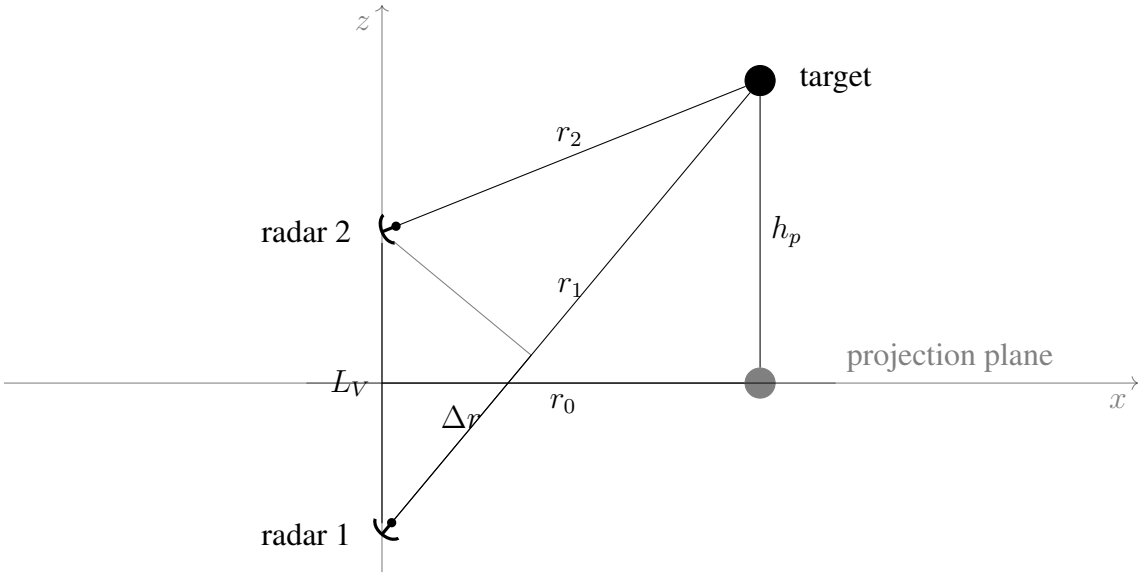

Figure 2.18. Radar interferometry schematics

The phase values of each signal are as follows:

$$\phi_1 = \angle \exp\left\{-j\frac{4\pi}{\lambda}r_1\right\}, \tag{2.24}$$

$$\phi_2 = \angle \exp\left\{-j\frac{4\pi}{\lambda}r_2\right\}. \tag{2.25}$$

Note that the range cannot be derived from this term, as it is a periodic function. The phase difference is given by:

$$\Delta\phi = \phi_2 - \phi_1. \tag{2.26}$$

If $\Delta r < \lambda$, then

$$\Delta\phi = \frac{4\pi}{\lambda}\Delta r, \tag{2.27}$$

where

$$\Delta r = r_2 - r_1. \tag{2.28}$$

The height over the projection plane h_p can be then calculated:

$$h_p = \frac{c}{4\pi f_c} r_0 \frac{\Delta\phi}{L_V}. \tag{2.29}$$

Note that the determined height depends on the phase difference $\Delta\phi$, not the distance difference Δr, so it is a periodic function. To fully illustrate that fact, a 3D PSF of an InSAR scenario is presented in Figure 2.19. It can be seen, that the maxima of the PSF are repeated along an

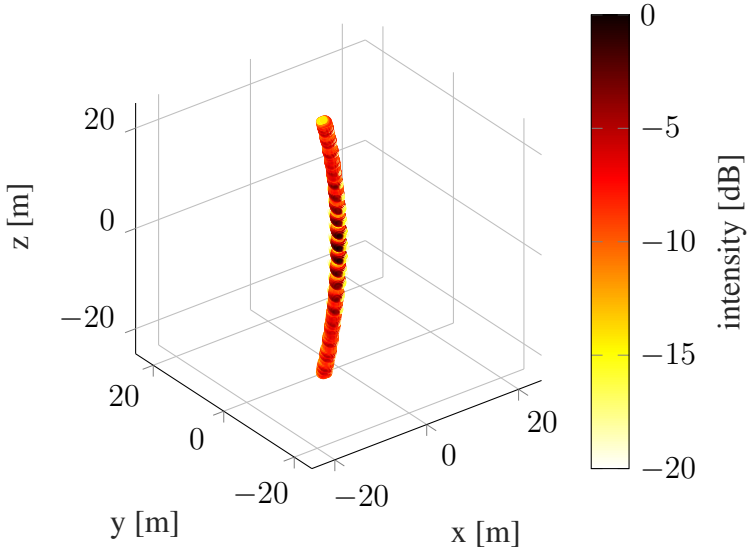

Figure 2.19. InSAR 3D PSF example.

arc. The vertical distance between the maxima determines both vertical spatial resolution and maximum unambiguous height of the imaged object. For clarity, a 2D cross section of the PSF is presented in Figure 2.20.

In fact, maximum unambiguous height depends on the baseline L_V [6]:

$$h_{umaxV} = \frac{\lambda R}{L_V}. \tag{2.30}$$

This is illustrated in Figures 2.21 and 2.22, where a vertical cross-section of the PSF for shorter and longer baselines are shown. The longer the baseline, the lower the maximum unambiguous height.

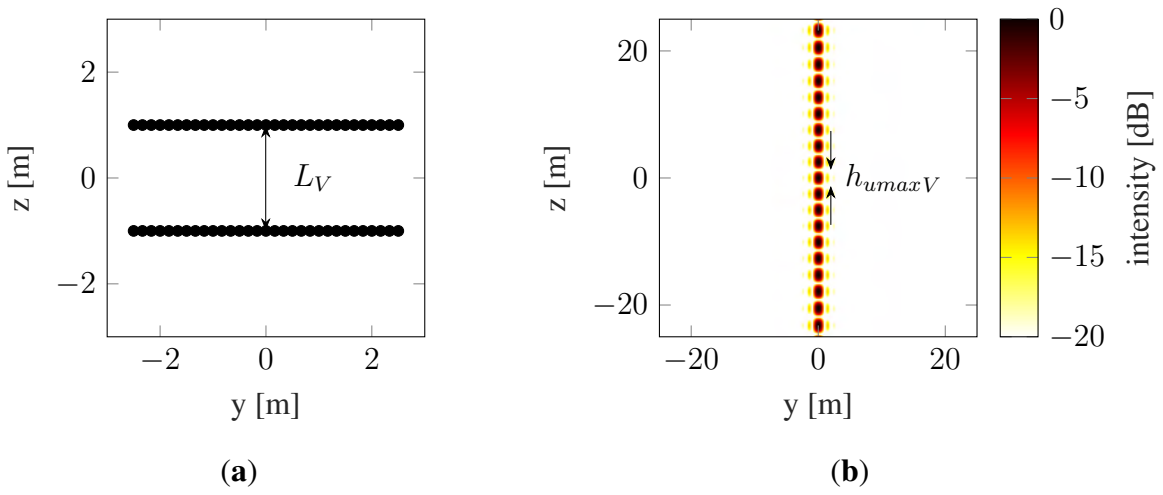

(a) **(b)**

Figure 2.20. InSAR with a medium baseline. **(a)** Trajectory, **(b)** 2D cross-range cross-section of 3D PSF.

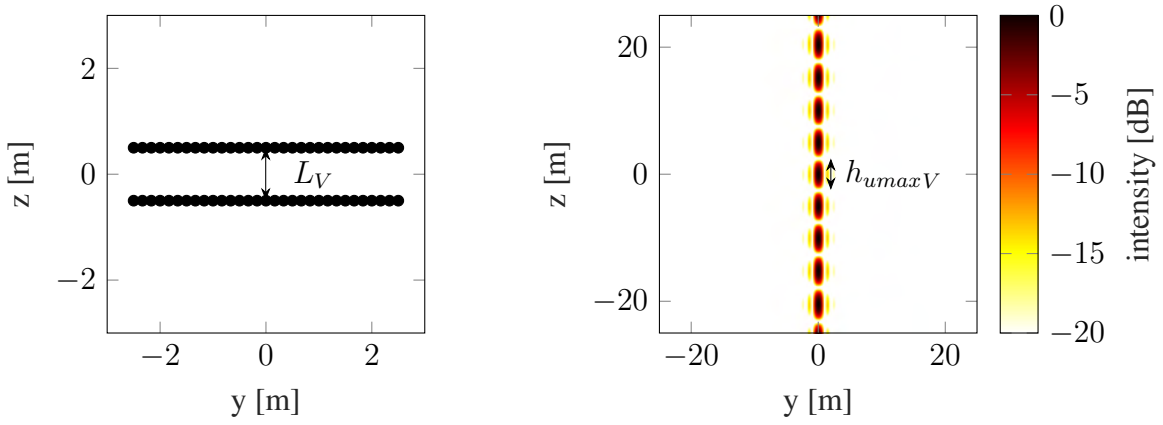

(a) **(b)**

Figure 2.21. InSAR with a short baseline. **(a)** Trajectory, **(b)** 2D cross-range cross-section of 3D PSF.

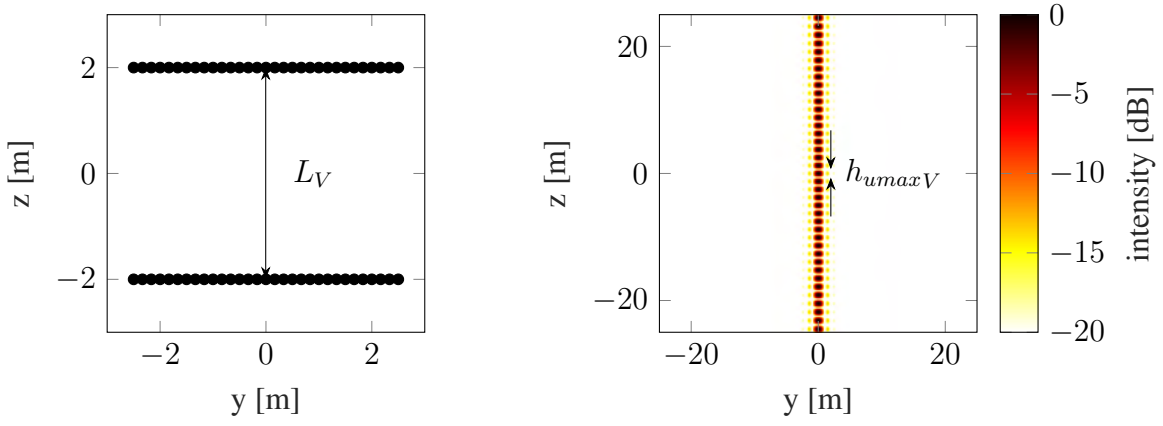

(a) **(b)**

Figure 2.22. InSAR with a long baseline. **(a)** Trajectory, **(b)** 2D cross-range cross-section of 3D PSF.

2.10. Optimization Problem

The solution to the optimization problem is to find the argument of the function (objective function) for which this function reaches an extreme [68]. In the case of minimization, the objective function is called the cost function, and this nomenclature is used later in this thesis. The mathematical notation of the minimization problem is as follows:

$$u_{opt} = \arg\min_{u} k\left(u\right), \tag{2.31}$$

where u_{opt} is the optimized value, u is value and $k(\cdot)$ is the cost function. Optimization problems can be divided by the convexity of the function into a convex optimization problem and a non-convex optimization problem. The former occurs when the cost function is convex in the region of interest and all its minima are global minima. An example of a convex and strictly convex function is shown in Figure 2.23. A strictly convex function has only one global

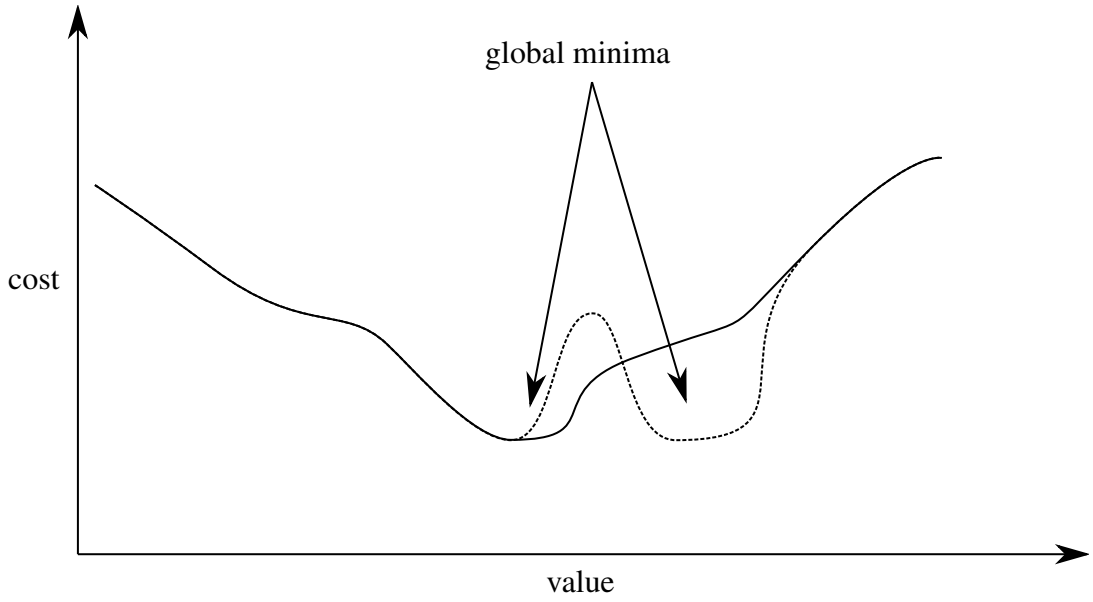

Figure 2.23. An example of a convex (dashed) and strictly convex (solid) function

minimum.

When the cost function is not convex, it is a non-convex optimization problem. In this case, the cost function may have one or more local minima that are not global minima, as well as saddle points. An example of a non-convex cost function is shown in Figure 2.23. For a non-convex cost function, solving the minimization problem does not necessarily lead to a global minimum, as shown in Figure 2.23 – one optimization run ends at the local minimum, one at the saddle point, and one at the global minimum. To increase the probability of reaching the local minimum, where the function's value deviates as little as possible from the global minimum, additional procedures are used, the simplest of which is to run the minimization process for many different positions of the starting point, as shown in Figure 2.23.

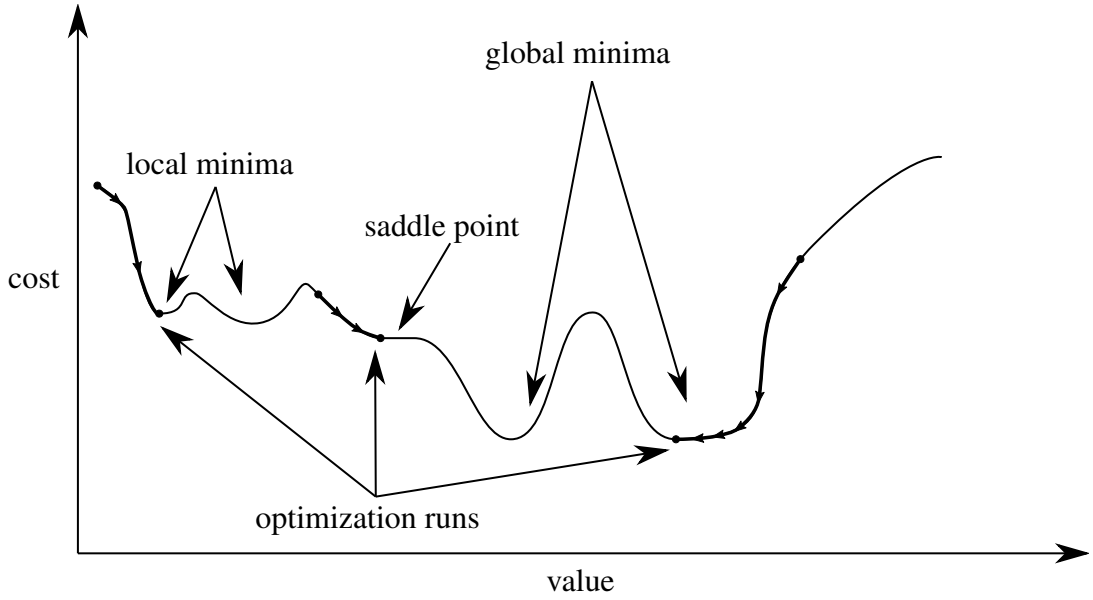

Figure 2.24. An example of a nonconvex function with optimization runs depicted with a thick line

If the cost function is differentiable, a gradient technique can be used to solve the optimization problem – which involves determining the gradient of the cost function at each optimization step and following the steepest slope until the minimum is reached. In the case of a non-differential cost function, determining the gradient is not always possible and another approach, such as the one based on simplex [69], should be used.

The optimization process is as follows:

1. Select a starting point.
2. Calculate the gradient/simplex at the current point.
3. Follow the steepest slope.
4. If the step size or cost change is less than the predefined limit, stop. If not, return to Step 2.

The process of solving the minimization problem is discrete, so in practice it never reaches the actual minimum of the cost function. Three criteria are commonly used to terminate the iterative process:

— The step value of the function's argument is less than some assumed minimum.
— The change in the value of the cost function in the last step is less than some assumed minimum.
— The total number of iterations has reached the assumed maximum.

2.11. Chapter Summary

This chapter presents the theoretical basis for the topics covered in this dissertation, presents basic formulas, symbols, and concepts. Strong emphasis is placed on quality metrics and PSF analysis. The next chapter presents the current state of the art in 3D SAR imaging.

3. State of the Art and Literature Review

At the beginning of this chapter, the historical background of the development of the SAR technique leading to current 3D SAR work is presented. The next section provides a thorough review of existing approaches, along with identification of the problems that underlie the method presented in this dissertation. The final section of this chapter summarizes the conclusions of the literature review.

3.1. Historical Background

The SAR concept was firstly reported in 1951 by Carl A. Wiley [70], then named Doppler Beam Sharpening (DBS) by Wiley himself[1]. Currently, in the literature, the difference between DBS and SAR is the angular coverage – much higher for DBS, which is commonly understood as an advancement of the rotating antenna approach and much lower for SAR, which is commonly understood as an advancement of Side-Looking Airborne Radar (SLAR).

First, a functional simulator was presented the next year, and first airborne SAR system capable of creating SAR images in real-time was finished in 1953. In 1954, Wiley filled a patent application for "Pulsed Doppler Radar Methods and Apparatus", which resulted in a secrecy order from the Patent Office a year later [71]. It remained in force for a decade, although it did not stop Wiley and others from working on SAR, which quickly became an important radar imaging technique.

While the initial motivation to develop SAR was to overcome optical imaging limitations, mainly the dependence on daylight and vulnerability to clouds and fog, nowadays SAR imaging is not a substitute of optical imaging. SAR allows one to extract many target features using various frequency ranges and polarimetry [72]. Radar beams can penetrate not only through foliage, but also structures and even ground.

An essential milestone in the development of SAR was the launch of the Seasat 1 satellite in 1978. This mission provided scientists at the National Aeronautics and Space Administration (NASA) Jet Propulsion Laboratory (JPL) with data for experiments with radar interferometry

[1] *I had the luck to conceive of the basic idea, which I called Doppler Beam Sharpening (DBS), rather than Synthetic Aperture Radar (SAR). Like all signal processing, there is a dual theory. One is a frequency-domain explanation. This is Doppler Beam Sharpening. If one prefers, one can analyze the system in the time domain instead. This is SAR. The equipment remains the same – just the explanation changes.*[70]

[73], and although they were not the first of its kind [74], they contributed to the rapid development of the InSAR technique, which was a synonym for 3D SAR for decades. Currently, many scientists and teams around the world are involved in 3D SAR research, developing this technique in many different directions [75, 76, 77, 78].

3.2. Existing 3D SAR Methods

The simplest method for obtaining 3D imaging – InSAR – is presented in Chapter 2 in Section 2.9. The main disadvantage of this method is the ambiguity of the height determination (see (2.30)). When the height differences in the ROI are not large, it is possible to use phase unwrapping to obtain the correct height map [6]. However, when the height differences are large, especially in urban environments or when imaging infrastructure elements, solving the problem of height determination ambiguity is not possible [79].

This section provides an overview of existing 3D SAR imaging solutions, divided into two subsections. The first one presents the commonly used multi-baseline SAR in general, while the second one thoroughly reviews articles presenting more complex non-rectilinear trajectories. In addition, the third subsection presents a selected paper in the field of UAV trajectory planning not directly concerned with 3D SAR.

3.2.1. Multi-baseline SAR

The simplest approach to solving the ambiguity problem that exists in the InSAR technique is to increase the number of baselines. In the case of consecutive rectilinear flights, this is the MBSAR technique shown in Figure 3.1, and in the case of a spiral flight, it is the CSAR or Tomographic Synthetic Aperture Radar (TomoSAR) technique [80] shown in Figure 3.2. In fact, all these approaches are equivalent to each other and imply the use of multiple parallel horizontal rectilinear apertures. The CSAR and TomoSAR usually refer to aerospace applications, and MBSAR to space applications. In the remainder of this paper, these methods are collectively referred to as MBSAR. The main advantage of MBSAR is that there is no trade-off between resolution and ambiguity in height determination. The resolution depends on the vertical size of the synthetic aperture, that is, the distance between the lowest and highest pass:

$$\delta_V = \frac{\lambda R}{2L_V}, \tag{3.1}$$

where λ is wavelength, R is the distance to the scene and L_V is the distance between the lowest and highest pass. The highest unambiguous height depends on the spacing between successive passes (see also (2.30)):

$$h_{umaxV} = \frac{\lambda R}{d_V}, \tag{3.2}$$

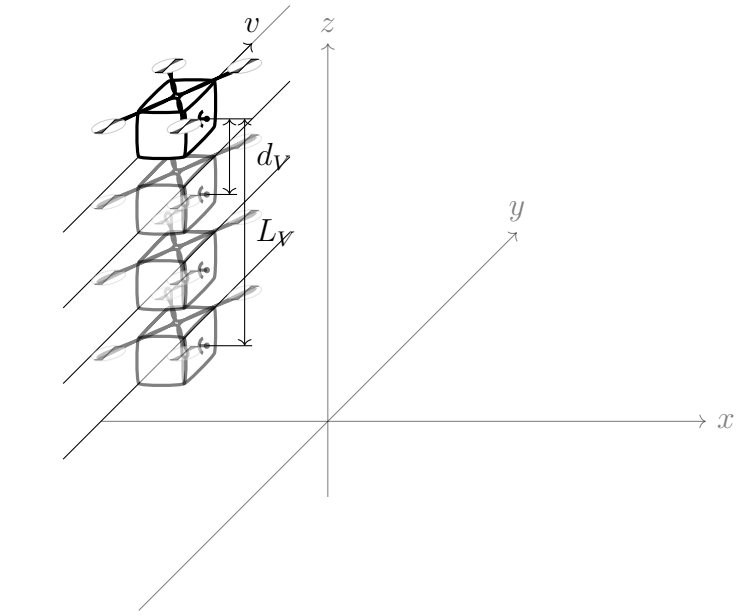

Figure 3.1. MBSAR geometry.

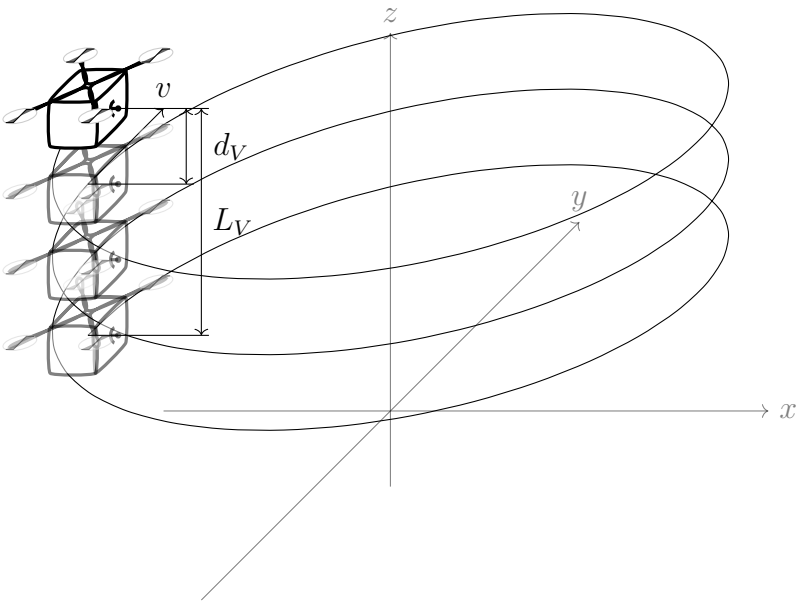

Figure 3.2. CSAR geometry.

where d_V is the spacing between successive passes. An illustration of the relationships (3.1) and (3.2) is shown in Figure 3.3. 3D PSF of an MBSAR trajectory is presented in Figure 3.4. Increasing the vertical aperture size improves the resolution, as shown in Figure 3.5, while decreasing the spacing between successive passes increases the largest unambiguous height, as shown in Figure 3.6. It should be noted that the resolution and largest unambiguous height can be adjusted separately.

Advantages of the MBSAR technique include simple flight planning and signal processing and the possibility of using a single-channel radar, while a significant disadvantage is the long

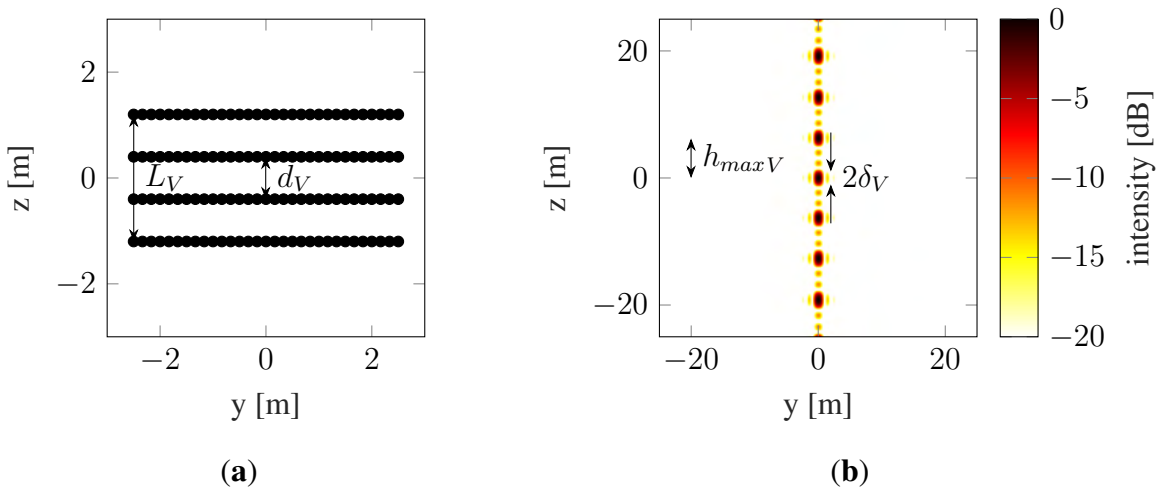

Figure 3.3. MBSAR. **(a)** Trajectory, **(b)** 2D cross-range cross-section of 3D PSF.

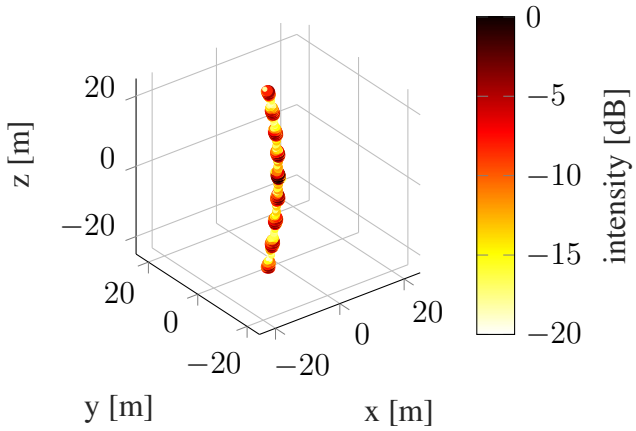

Figure 3.4. MBSAR. 3D PSF. Non-zero bandwidth is assumed for image readability.

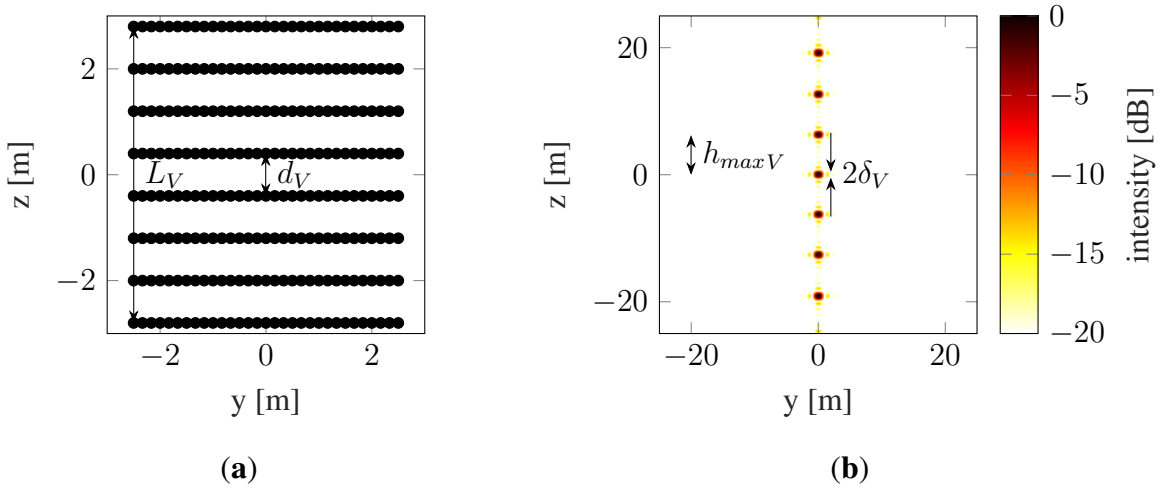

Figure 3.5. MBSAR with increased vertical synthetic aperture size. **(a)** Trajectory, **(b)** 2D cross-range cross-section of 3D PSF.

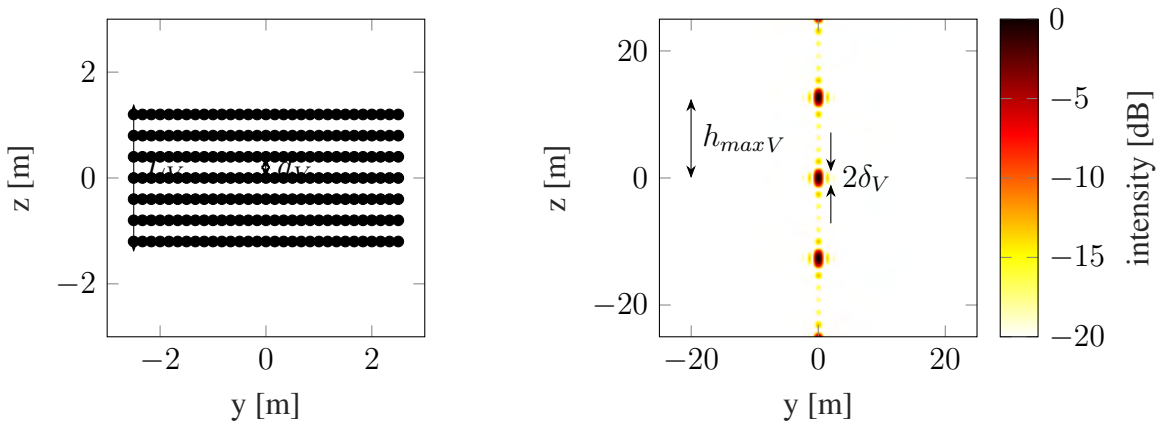

(a) **(b)**

Figure 3.6. MBSAR with decreased vertical synthetic aperture size. **(a)** Trajectory, **(b)** 2D cross-range cross-section of 3D PSF.

trajectory, which translates into large imaging duration and a large amount of collected data. In addition, sources on military applications emphasize that multipass SAR is impractical in these applications [81].

3.2.2. Non-rectilinear trajectories

The previous subsection presents a class of MBSAR techniques that allow obtaining 3D imaging without the drawbacks associated with InSAR. In this subsection, methods using non-rectilinear trajectories are presented.

3.2.2.1. HAT Manouver

Radars with SAR mode are mounted on fighter aircraft to support reconnaissance and target designation for precision munitions. The work [81] describes a method of improving munition targeting accuracy by determining the height of the target. This uses a change in the platform's flight altitude over the target during imaging. The HAT maneuver, shown in Figure 3.7, consists of a push-over with a preset acceleration followed by a pull-up with an acceleration of the same value but opposite sign. The height of the target above the focus plane is proportional to the quadratic phase error contained in the SAR image. The work [81] focuses primarily on military applications, but indicates the possibility of civilian application – the creation of geodetic maps. The PSF of a sample HAT manouver is presented in Figure 3.8 and 3.9.

A significant advantage of the presented method is the acquisition of altitude information using a single-channel radar and a single pass. The problem of ambiguity is also solved. The disadvantages of this method include, first of all, the need to ensure that the push-over has the same parameters as the pull-up.

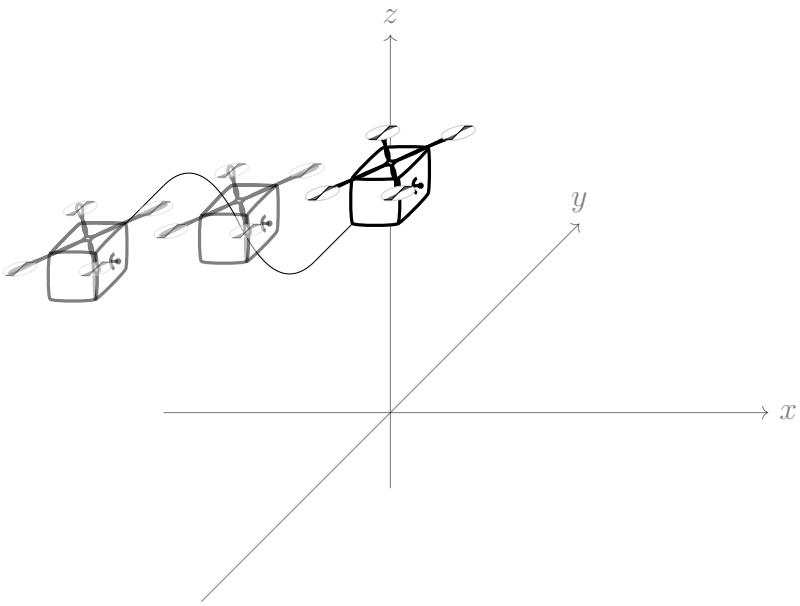

Figure 3.7. HAT

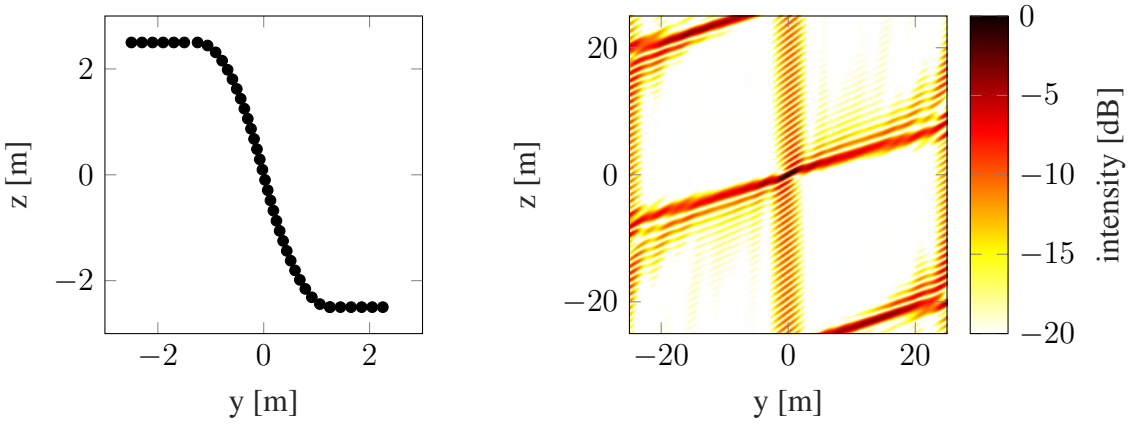

(a) **(b)**

Figure 3.8. HAT. **(a)** Trajectory, **(b)** 2D cross-range cross-section of 3D PSF.

3.2.2.2. Sine-shaped Trajectory

A modification of the HAT Manouver concept is the sine-shaped trajectory [82] presented in Figure 3.10. The publication [82] is an analysis of the feasibility of obtaining 3D imaging for single-pass, non-rectilinear trajectories. The paper primarily contains simulation results showing the trajectories and their corresponding PSFs. The only mathematical formulas presented are those of resolution and ambiguity/grating lobes and are equivalent to (2.17) and (2.30). The paper begins with a presentation of the rectilinear trajectory and an indication that it does not provide 3D resolution. Next, a very dense multipass trajectory is presented, which provides 3D resolution, but it is pointed out that it is impractical due to its length (see also Figure 3.6). Next, the author presents the trajectory in the form of a single sinusoidal waveform

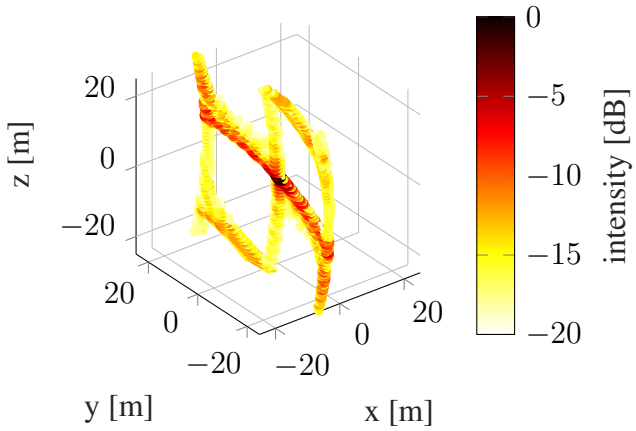

Figure 3.9. HAT. 3D PSF. Non-zero bandwidth is assumed for image readability.

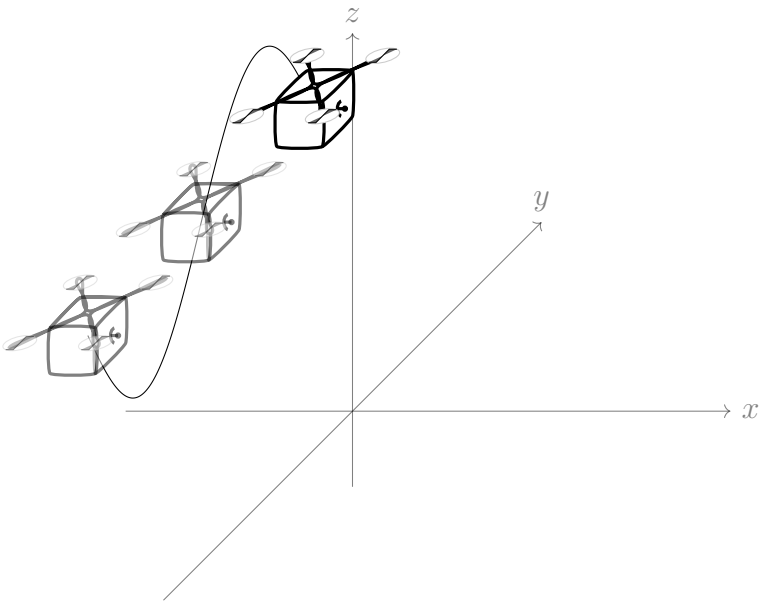

Figure 3.10. Sine SAR.

and the resulting PSF, as presented in Figure 3.11 and 3.12, additionally stating that it is a variant of the HAT [81]. In the next section of the paper, a circular trajectory and a trajectory that is a composite of a circular trajectory and a sinusoidal trajectory are presented. Due to the simulational rather than the analytical nature of the paper, the conclusions are quite general but relevant. The author of the paper emphasizes the generality of the solution – a non-rectilinear trajectory provides resolution in 3D, and depending on the scenario, the horizontal sine function can be replaced by a vertical one. He points out the possible limitations of the platform (although not written explicitly, it can be inferred that the author is considering fixed-wing) and the need to adapt the trajectory parameters to its capabilities. Essential are the proposals for further work, which include the use of PSLR and ISLR for assessing the quality of the imaging,

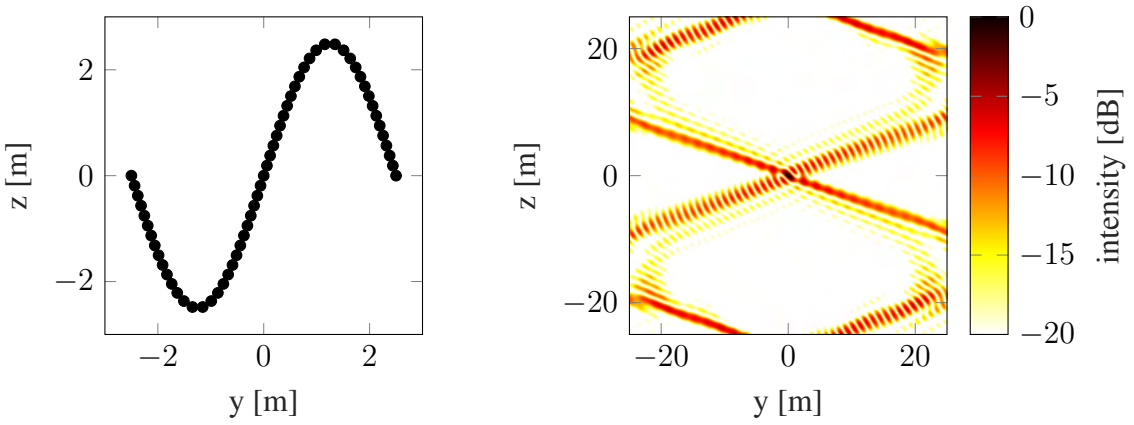

Figure 3.11. Sine-shaped trajectory. **(a)** Trajectory, **(b)** 2D cross-range cross-section of 3D PSF.

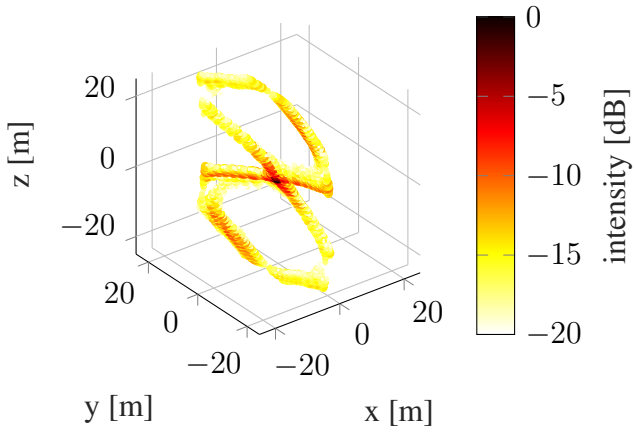

Figure 3.12. Sine-shaped trajectory. 3D PSF. Non-zero bandwidth is assumed for image readability.

investigating the impact of position determination accuracy, experiments using real-life data, and direct comparison with MBSAR.

Because of its great similarity to HAT Manouver, the advantages of this method are the same as listed in the last paragraph of Subsection 3.2.2.1. Since the paper [82] does not explicitly indicate how the altitude is determined, the difficulty of mapping the trajectory of the radar platform cannot be explicitly pointed out as a disadvantage. It should be noted that if the goal of SAR imaging is to obtain a 3D image, both HAT manouver and sine trajectors with the same vertical span provide the same vertical resolution (compare Figure 3.8 and Figure 3.11), and imaging errors result not from inaccuracies in mapping the assumed trajectory, but from errors in determining the position of the radar platform.

3.2.2.3. Parabolic Trajectory

An important work in the field of UAV trajectory planning for 3D SAR is [83]. It assumes a bistatic geometry with a stationary transmitter. Two imaging approaches are presented:

non-parametric, where the criterion for evaluating 3D imaging is the crossrange horizontal and vertical resolution (see (2.17)), and parametric, where the criterion is the Cramer-Rao Lower Bound (CRLB) of scatterer parameter variance. The paper presents simulation results, where a quadratic component is added to a rectilinear trajectory, followed by a skewed trajectory, resulting in 3D imaging. The final result is a two-dimensional trajectory, which can be described by two parameters – the eccentricity of the square component and the angle of inclination. Such a trajectory can be realized by both fixed wing and multirotors, the paper does not specify, and there is no reference to the platform motion model.

Similar to the paper [82], the paper [83] ties together the geometric parameters of the trajectory and the quality of the 3D imaging, which can allow the selection of the trajectory depending on the quality required. Due to the non-periodicity of the trajectory and bistatic geometry, the application of this method is limited to spotlight SAR.

3.2.3. Platform Trajectory Planning

A different approach to planning of the trajectory of a UAV with a SAR sensor is presented in [84]. It focuses exclusively on military missions aimed at reconnaissance and identification of ground targets. This work focuses on fixed-wing UAVs and presents experimental results. It does not assume 3D imaging and therefore does not consider its parameters, but takes into account the area of flight, taking into account the location of targets, obstacles, and enemy forces. One of the main goals of route optimization is to minimize the risk of shooting down the UAV, another goal is to ensure that the length of the synthetic aperture fragment needed for target imaging is adequate.

3.3. Chapter summary

Although there are not many papers dealing strictly with the trajectory determination of a radar platform for 3D SAR imaging, the significant increase in the number of publications on 3D SAR imaging using UAVs in recent years [85, 86] suggests that this is a topic gaining in importance.

The works [81, 82, 83] touch on the problem of creating two-dimensional trajectories, but they have some limitations, which the present work aims to overcome:

— The trajectories obtained are simple functions that are defined by a few parameters, so they have little tuning potential, and they do not fully exploit the maneuverability offered by the multirotor.

— The only imaging quality parameter is resolution (and, in the case of [83], also CRLB), while other quality measures such as PSLR and ISLR are not included, which also makes tuning these trajectories difficult. The work of [82] noted that PSLR and ISLR provide

additional information about the quality of the imaging and indicated the need to use them in future studies.

— Trajectories are described using mathematical functions without considering the platform's motion model. In the case of UAVs, it is common to plan a route using waypoints, so for practical application of the presented methods, it is still necessary to introduce the relationship between waypoint placement and trajectory parameters.

— Although not explicitly written, the trajectories obtained in these works appear to be for fixed-wing and the works do not address the topic of flight time and energy consumption.

The next chapter presents the method of obtaining 3D SAR images that builds on the analysed literature and aims to overcome the limitations of the already presented methods.

4. Method

In this chapter, the method of obtaining 3D SAR images is described. The chapter begins with a brief introduction, and then the design assumptions for the method are presented. The main part of the chapter is a description of the individual steps of the algorithm.

4.1. Introduction

The previous section presents various non-rectilinear radar platform trajectories that can be used to obtain 3D SAR imaging. They allow obtaining 3D images with similar parameters as MBSAR, but with shorter flight times.

The essence of this work is a method for obtaining 3D SAR imaging using non-rectilinear trajectories, which is an extension of the methods presented in the previous chapter. The key part of the method is the determination of the radar platform trajectory based on known radar and platform parameters, as well as assumed imaging quality requirements. The next section presents the assumptions underlying the method.

4.2. Assumptions

In order to fulfil the theses of the dissertation outlined in Section 1.2, it is assumed that the presented method, compared to the existing ones, must meet the following assumptions:

— A larger number of controllable trajectory parameters.
— A trajectory linked to the actual radar platform motion model.
— Use of imaging quality measures other than just resolution.
— Consideration of trajectory tuning to improve trajectory parameters.

These assumptions are described in detail in the following subsections

4.2.1. Number of controllable parameters

For simple trajectories, such as a sinusoidal one, the resolution can be affected by changing the trajectory dimensions, but the shape of the PSF and, in particular, the side lobes does not change. Moreover, a sinusoidal trajectory, due to its periodicity, has very distinct side lobes, as shown in Figure 4.1. Introducing some irregularity into the shape of the trajectory

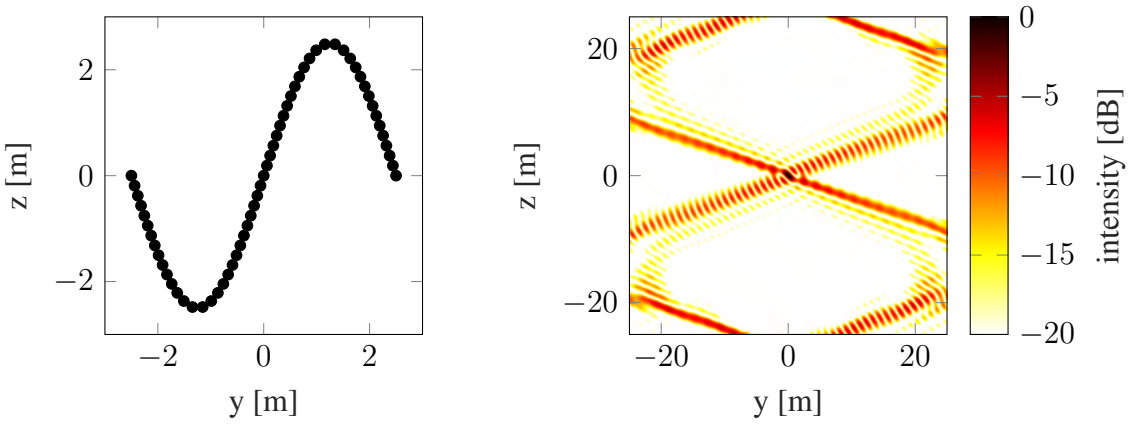

Figure 4.1. Sine-shaped trajectory. **(a)** Trajectory, **(b)** 2D cross-range cross-section of 3D PSF.

allows blurring the side lobes and thus reducing the PSLR, as shown in Figure 4.2. Additional

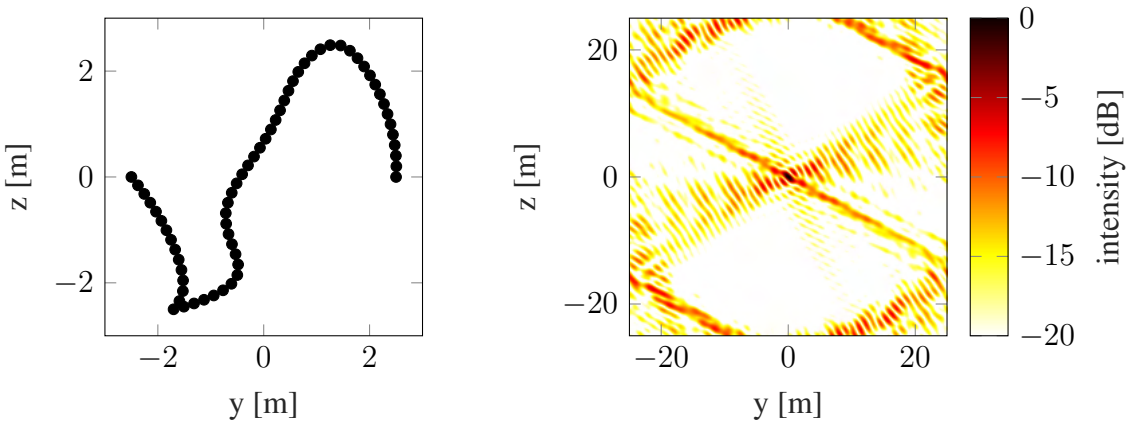

Figure 4.2. Non-periodic trajectory. **(a)** Trajectory, **(b)** 2D cross-range cross-section of 3D PSF.

trajectory parameters allow precise control of the PSF shape.

4.2.2. Radar Carrier Motion Model

Simple trajectories are not always straightforward from the point of view of the radar platform's motion model, and do not necessarily allow one to use platform parameters to reduce flight time. Both HAT and sine trajectories can theoretically be implemented based on acceleration control (with a constant step value in the case of HAT or sinusoidally varying in the case of a sine trajectory), but when considering the influence of the medium (the surrounding air, including the motion caused by wind), on the platform's flight trajectory, they enforce the use of corrections or the need to accept discrepancies between the assumed and realized trajectory. Multirotors use a trajectory planning model based on waypoint following using a jerk limited

motion model [87]. Accurately reproducing a HAT or a sinusoidal trajectory using this model requires the use of a large number of waypoints, so a trajectory model with a smaller number of waypoints should be used, moreover, allowing full use of the maneuverability of the multirotor.

4.2.3. Imaging quality measures

Resolution is the most important parameter of a SAR image, and for traditional trajectories like MBSAR, it is sufficient. However, for non-rectilinear trajectories, the side lobes described by the PSLR and ISLR parameters play an important role. This is pointed out in [82]. Resolution in combination with PSLR and ISLR gives a more complete picture of imaging quality, so that the requirements can be formulated precisely. Figure 4.3 shows two PSFs with equal resolution, but different PSLR and ISLR. The PSF on the left has PSLR=-13.45 dB and ISLR=7.70 dB, while the PSF on the right has PSLR=-7.32 dB and ISLR=17.41.

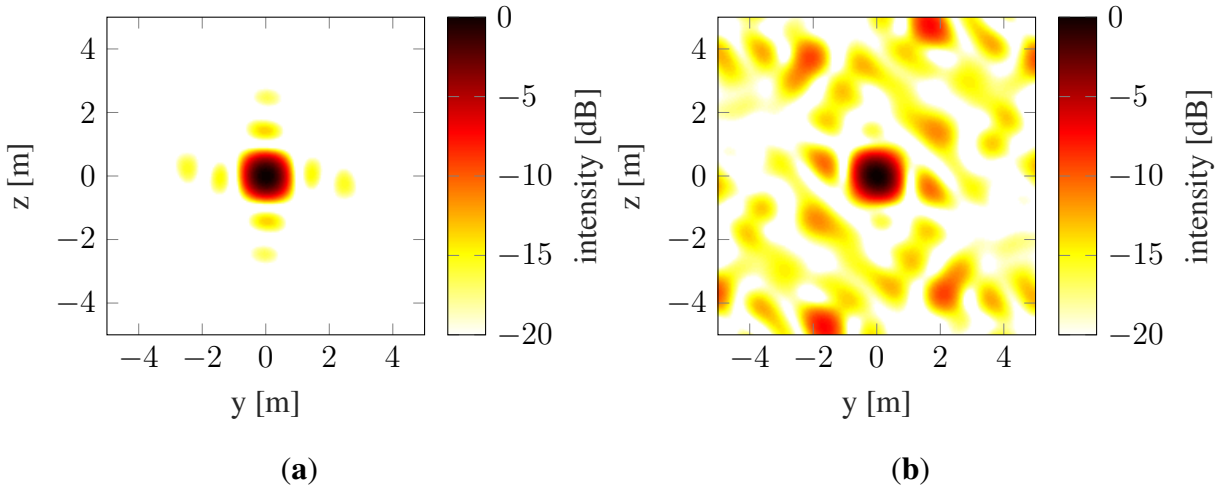

Figure 4.3. Cross-section of PSFs with the same resolution and different PSLR and ISLR. **(a)** Lower PSLR and ISLR, **(b)** higher PSLR and ISLR.

4.3. Trajectory Tuning

Directly relating the resolution to trajectory dimensions is possible [82], but mathematically determining the relationship of ISLR and PSLR to trajectory shape is a complex issue. If it is assumed that the synthetic aperture (sounding points) is some sparse sampling of the theoretical rectangular aperture (aperture area) [11], it can be generally stated that ISLR increases as the sampling density of the aperture area decreases, while PSLR increases as the regularity of the spacing of the sounding points increases, but these general relationships are not enough to produce trajectories with the best possible performance. The use of a minimization algorithm for tuning the trajectory allows its parameters to be improved (by achieving a local minimum of a cost function).

4.4. Overview

The goal of the proposed method is to provide a 3D SAR image of the ROI, that satisfies the assumed quality requirements. The image is created using a synthetic aperture that is formed by a radar platform trajectory. To obtain 3D SAR imaging, a synthetic aperture of at least two dimensions is required - more precisely, a synthetic aperture with two degrees of freedom that are not distance, that is, an aperture with non-zero angular span in the elevation and azimuth directions relative to the ROI. A simplified geometry of the method is presented in Figure 4.4.

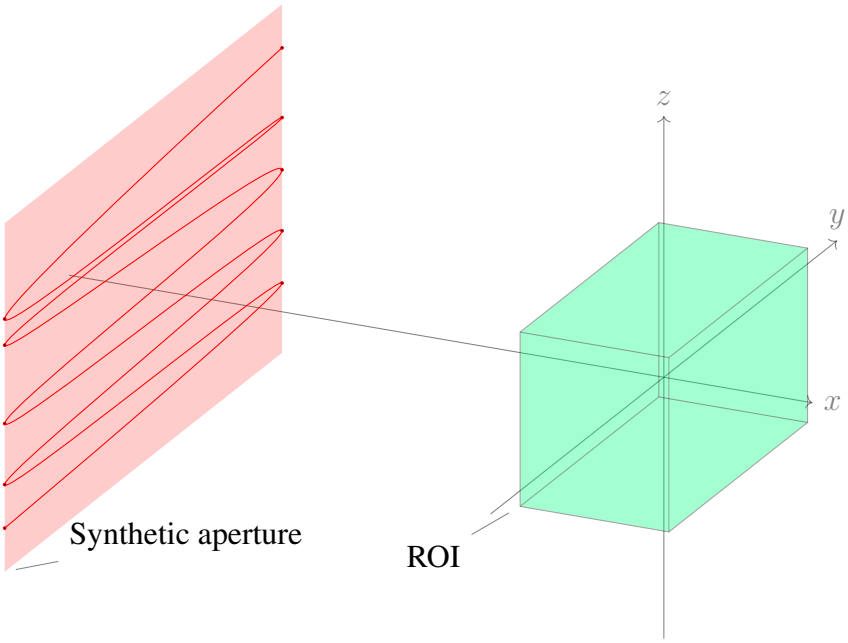

Figure 4.4. 3D SAR geometry

The key point of the method is to create a specific trajectory based on the preliminary information on the ROI and expected imaging quality requirements. The trajectory is then tuned to improve the imaging quality and reduce the trajectory length. The word *tuned* is used in this work instead of *optimized* to stress the complexity of the problem. While the optimal solution certainly exists, given the multitude of conditions and tunable parameters, the method of finding it would be overly complicated. Additionally, there might be more than one optimal solution for a given scenario.

The general diagram of the method is depicted in Figure 4.5.

In the first step of the algorithm, the known parameters of the scenario and the system are identified, and the quality requirements are defined. Next, the position of the synthetic aperture surface is determined such that it can achieve the desired resolution and ensure that the trajectory requirements are met. The subsequent step is to determine the waypoints for the radar platform to determine the trajectory (synthetic aperture). Quality parameters are determined for this

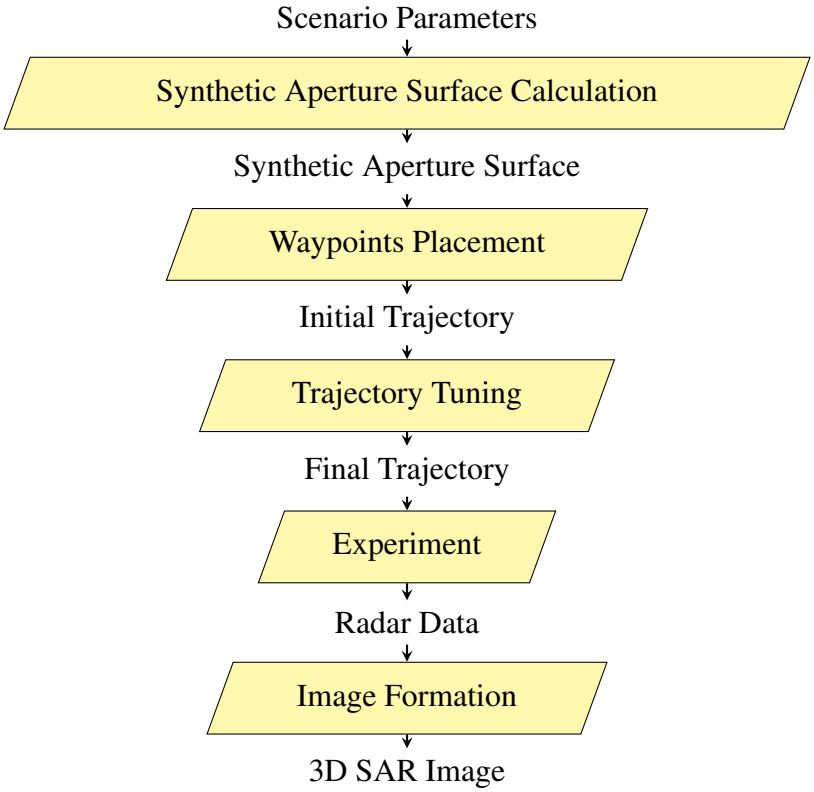

Figure 4.5. General diagram of the method.

initial trajectory. In the next step, the trajectory is tuned, that is, the cost function is minimized. A final trajectory is obtained. Having a final trajectory, an experiment can be conducted, that is, the waypoints are programmed on the radar platform and the reflected echoes are collected. The final step is to create a 3D image from the collected echoes.

4.5. Scenario Parameters

This section describes the main scenario parameters that affect the final trajectory shape.

4.5.1. Geometry

The ROI is assumed to be located in the center of the coordinate system and is observed from the direction of the negative x-axis. The parameters defining the ROI are the horizontal size D_H and the vertical size D_V.

4.5.2. Radar Parameters

The important parameters of the radar are, first and foremost, bandwidth B and the wavelength determined by the formula:

$$\lambda = \frac{c}{f_c}. \tag{4.1}$$

In addition, the horizontal and vertical antenna beam width: θ_H, θ_V and radar range should be known.

4.5.3. Radar Platform Parameters

This dissertation assumes that the radar platform is a multirotor[1]. It is assumed that the radar platform has the ability to steer the antenna beam to the ROI, horizontally by rotating the platform around a vertical axis, and vertically by using a gimball, for example. If beam steering is not possible, it is necessary to increase the distance of the trajectory from the ROI accordingly, so that it is always in the beam.

The radar platform is assumed to use the jerk-limited motion model used in popular UAV controllers, such as PX4 [88]. The jerk-limited motion model assumes that the first, second, and third time derivatives of the position are constrained. Restricting the third derivative theoretically has no effect on the force, but helps reduce unwanted vibrations [87]. The parameters of the motion model are summarized in table 4.1, along with the example values used in the PX4 controller.

Parameter	**Symbol**	**Default value** [89]
Maximum jerk	j_{max}	$8\,\mathrm{m/s^3}$
Maximum horizontal acceleration	$a_{H\,max}$	$5\,\mathrm{m/s^2}$
Maximum upwards acceleration	$a_{V\uparrow max}$	$4\,\mathrm{m/s^2}$
Maximum downwards acceleration	$a_{V\downarrow max}$	$3\,\mathrm{m/s^2}$
Maximum horizontal velocity	$v_{H\,max}$	$12\,\mathrm{m/s}$
Maximum upwards velocity	$v_{V\uparrow max}$	$3\,\mathrm{m/s}$
Maximum downwards velocity	$v_{V\downarrow max}$	$1\,\mathrm{m/s}$

Table 4.1. Motion model parameters used in this dissertation.

An important parameter of the radar platform is the route planning model. The route is defined by a set of ranked waypoints. At each time instant, only one waypoint is active, and the platform follows its direction. When the distance of the platform from the active waypoint is less than or equal to the acceptance radius, the next waypoint becomes active until the last one.

[1] It is possible to use other types of platforms, such as fixed-wing or even a ground vehicle (in the case of Ground-Penetrating Radar (GPR)), but issues related to their movement models are beyond the scope of this work.

An additional parameter that can be taken into account in determining the trajectory is the capacity of the platform's energy source (e.g., batteries), expressed as the flight time from takeoff until the energy source is exhausted (which should be minus the time it takes to safely return to the takeoff point). In addition, the time required to replenish the energy source (e.g., replacing or recharging the battery) can be taken into account, which is important if the resulting trajectory cannot be realized in a single flight.

4.5.4. Image Quality Requirements

Image quality requirements refer to the image quality metrics described in Section 2.8. The main quality requirement is horizontal and vertical resolution: δ_H, δ_V (see Section 2.8.1). Both of these parameters must be specified, otherwise 3D imaging is not possible. Resolution in the distance direction is not specified, as it depends primarily on the bandwidth of the radar, and it is considered invariant. In addition, PSLR (see Section 2.8.2) and ISLR (see Section 2.8.3) can be specified. These parameters are determined for the PSF cross-section, not the full 3D PSF. Calculating the PSF in 3D and tuning the trajectory based on this is possible, but for typically used radar bandwidths it does not significantly improve imaging quality, and is computationally very demanding [28].

4.6. Synthetic Aperture Surface Determination

As stated in Chapter 2, SAR imaging using a non-rectilinear trajectory can be interpreted as imaging using a non-uniformly sampled aperture. This is presented in Figure 4.6, which shows that aperture sampling can be considered separately from the trajectory. Under this assumption,

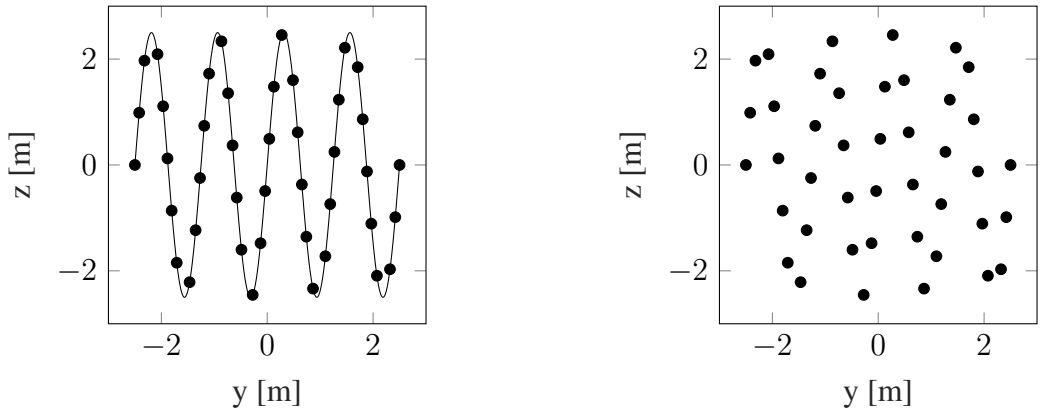

Figure 4.6. Sample non-rectilinear trajectory: **(a)** with indicated flight path, **(b)** without indicated flight path.

the dimensions of the aperture area can be related to the resolution achieved.

In view of this, the first step of the algorithm is to determine the synthetic aperture surface, i.e., its distance from the ROI and its vertical and horizontal spread. The following subsections describe how to determine these parameters.

4.6.1. Distance to ROI

The first parameter of the synthetic aperture surface is its distance from the ROI. On the one hand, the synthetic aperture surface must be as close to the ROI as possible so that the synthetic aperture surface area is as small as possible for a given angular spread. On the other hand, it must also be far enough away so that the entire ROI can fit within the radar beam:

$$R > \frac{D_V}{2} \tan\left(\frac{\theta_V}{2}\right), \tag{4.2}$$

$$R > \frac{D_H}{2} \tan\left(\frac{\theta_H}{2}\right), \tag{4.3}$$

where D_V and D_H are vertical and horizontal dimensions of ROI, and θ_V and θ_H are vertical and horizontal antenna beamwidths.

In addition, it is necessary to ensure that the far-field conditions are met [6]:

$$R \gg D, \tag{4.4}$$

$$R \gg \lambda, \tag{4.5}$$

where R is the distance from the radar to the object and $D = \max(D_V, D_H)$ is the largest ROI dimension.

4.6.2. Synthetic Aperture Surface Span

The synthetic aperture surface span depends on the required resolution. If the requirements for horizontal and vertical resolution are defined, the required angular span of the aperture can be determined directly:

$$\alpha_V = 2 \arctan \frac{\lambda}{4\delta_V}, \tag{4.6}$$

$$\alpha_H = 2 \arctan \frac{\lambda}{4\delta_H}. \tag{4.7}$$

If the distance of the aperture surface from the ROI is known, the angular span can be translated into linear dimensions:

$$L_V = 2r \tan\left(\frac{\alpha_V}{2}\right) = \frac{r\lambda}{2\delta_V}, \tag{4.8}$$

$$L_H = \frac{r\lambda}{2\delta_H}. \tag{4.9}$$

Parameters L_V and L_H are analogous to the synthetic aperture length of 2D SAR.

4.7. Trajectory calculation

The previous section describes the steps leading to the definition of a synthetic aperture surface that, if sampled to satisfy the (2.15) condition, would ensure that the requirements for imaging resolution are met.

This section shows how to determine the synthetic aperture (trajectory) and the PSF parameters associated with it. The trajectory is derived from the platform's motion model and the placement of waypoints, while the placement of sounding points results directly from the PSF.

4.7.1. Waypoint Placement on the Synthetic Aperture Surface

In the previous section, it is shown that a synthetic aperture is created by sampling the synthetic aperture surface through a certain trajectory. Trajectory is defined by waypoints $(\boldsymbol{P_W}) = \boldsymbol{P_{W1}}, \boldsymbol{P_{W2}}, ..., \boldsymbol{P_{WN}}$ where N is the number of waypoints and

$$\boldsymbol{P_{Wn}} = \begin{pmatrix} P_{Wnx} \\ P_{Wny} \\ P_{Wnz} \end{pmatrix} \tag{4.10}$$

specifies waypoint coordinates. This work proposes the following method of placing waypoints on the synthetic aperture surface: waypoints distributed along one of the dimensions of the synthetic aperture surface, placed alternately on opposite sides of the synthetic aperture surface, visited by the platform according to a zig-zag pattern, as presented in Figure 4.7 and Figure 4.8. The initial and final points' positions are:

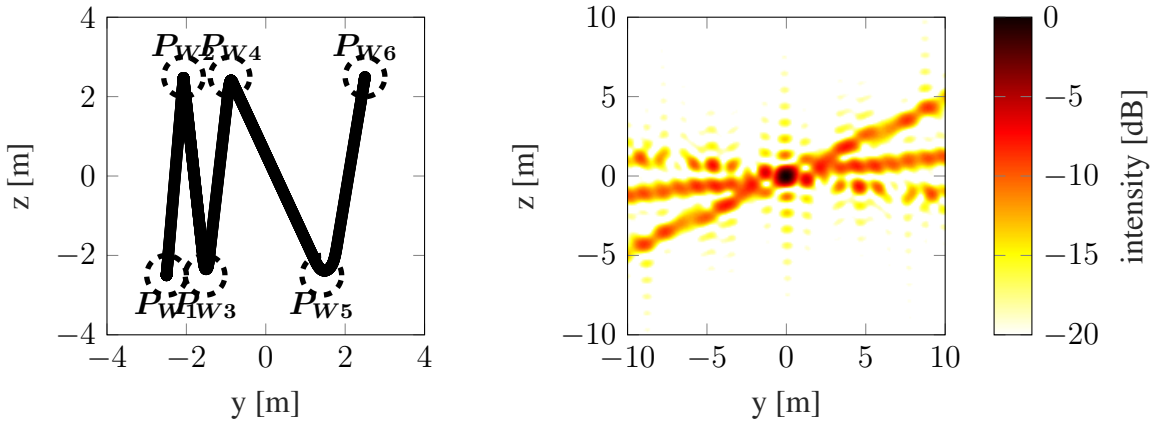

(a) **(b)**

Figure 4.7. Zig-zag with uneven waypoint placement. **(a)** Trajectory, **(b)** 2D cross-range cross-section of 3D PSF.

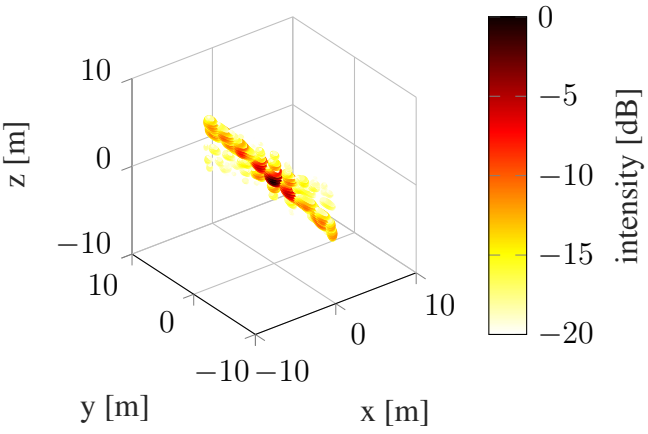

Figure 4.8. Zig-zag with uneven waypoint placement. 3D PSF.

$$\boldsymbol{P_{W1}} = \begin{pmatrix} -r \\ -\frac{L_H}{2} \\ -\frac{L_V}{2} \end{pmatrix}, \tag{4.11}$$

$$\boldsymbol{P_{WN}} = \begin{cases} \begin{pmatrix} -r \\ \frac{L_H}{2} \\ \frac{L_V}{2} \end{pmatrix} & \text{if } 2 \mid N, \\ \begin{pmatrix} -r \\ \frac{L_H}{2} \\ -\frac{L_V}{2} \end{pmatrix} & \text{if } 2 \nmid N, \end{cases} \tag{4.12}$$

and the remaining points' positions:

$$P_{Wnx} = -r, \tag{4.13}$$

$$P(P_{Wny} < t) = \begin{cases} 0 & \text{for } t \leq -\frac{L_H}{2}, \\ \frac{t}{L_H} + \frac{1}{2} & \text{for } -\frac{L_H}{2} < t \leq \frac{L_H}{2}, \\ 1 & \text{for } t > \frac{L_H}{2}, \end{cases} \tag{4.14}$$

$$P_{Wiy} \leq P_{Wjy} \forall i < j, \tag{4.15}$$

$$P_{Wnz} = \begin{cases} -\frac{L_V}{2} & \text{for } 2 \mid n, \\ \frac{L_V}{2} & \text{for } 2 \nmid n. \end{cases} \tag{4.16}$$

A random distribution of points compared to a uniform one provides a lowering of the PSLR. If the points were distributed uniformly, a trajectory similar to a sine wave would be obtained, which is characterized by a very prominent side lobe. This can be observed by comparing Figure 4.7 and Figure 4.9. It can be seen, that the side lobes are smeared, effectively reducing

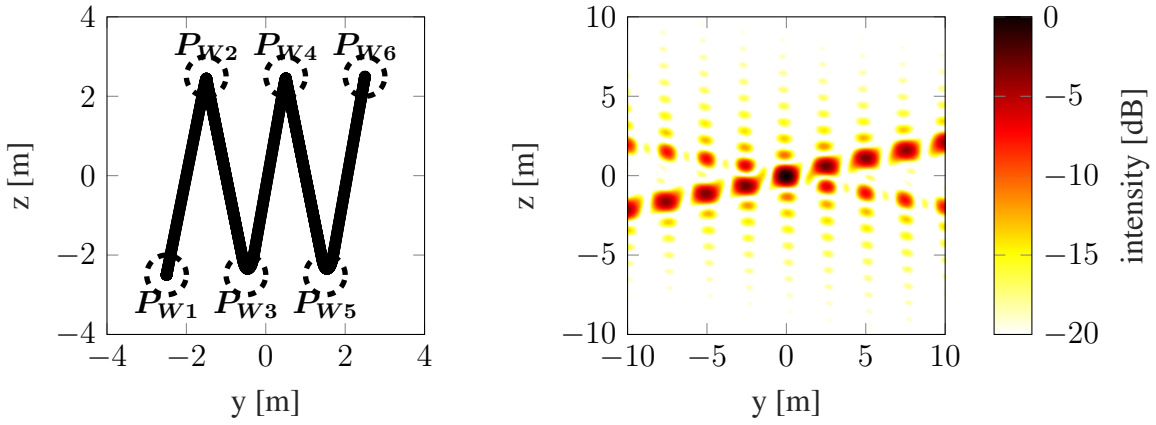

(a) **(b)**

Figure 4.9. Zig-zag with even waypoint placement. **(a)** Trajectory, **(b)** 2D cross-range cross-section of 3D PSF.

the PSLR.

4.7.2. Waypoints following

The waypoint following model assumed in this dissertation is presented in Figure 4.10. It is defined as follows: at each moment of the platform's movement, only one waypoint is active, the speed and acceleration are selected so that the platform can stop when it reaches the waypoint. An acceptance radius is defined for each waypoint, if the distance of the platform to the waypoint is less than the acceptance radius, the next waypoint becomes active. If the radius is set to zero, the trajectory consists of straight lines. Such an approach can be used when the time of flight is less important than simple processing and when the parameters of the platform motion model are not exactly known. Figure 4.11 shows three apertures (trajectories) for the same waypoint placement and different values of the acceptance radius.

At each discrete time moment, t waypoint following process must determine the current active waypoint or qualify the trajectory as complete. Distance to the nth waypoint is calculated as

$$d_n = \left\| \boldsymbol{P_P}(t) - \boldsymbol{P_{Wn}} \right\|, \tag{4.17}$$

where $\boldsymbol{P_P}(t)$ is the position of the platform at time t, $\boldsymbol{P_{Wn}}$ is the nth waypoint. If the distance to the current waypoint is less than the acceptance circle radius r_a, then the next waypoint is selected, and the process is repeated until a distant waypoint is found or the trajectory is deemed complete (all N waypoints were visited by the radar platform), as depicted in Algorithm 1. The movement between waypoints can be divided into 7 phases, which are shown in Figure 4.12:

1. Increasing acceleration with maximum jerk until maximum acceleration is reached.
2. Increasing speed with maximum acceleration.

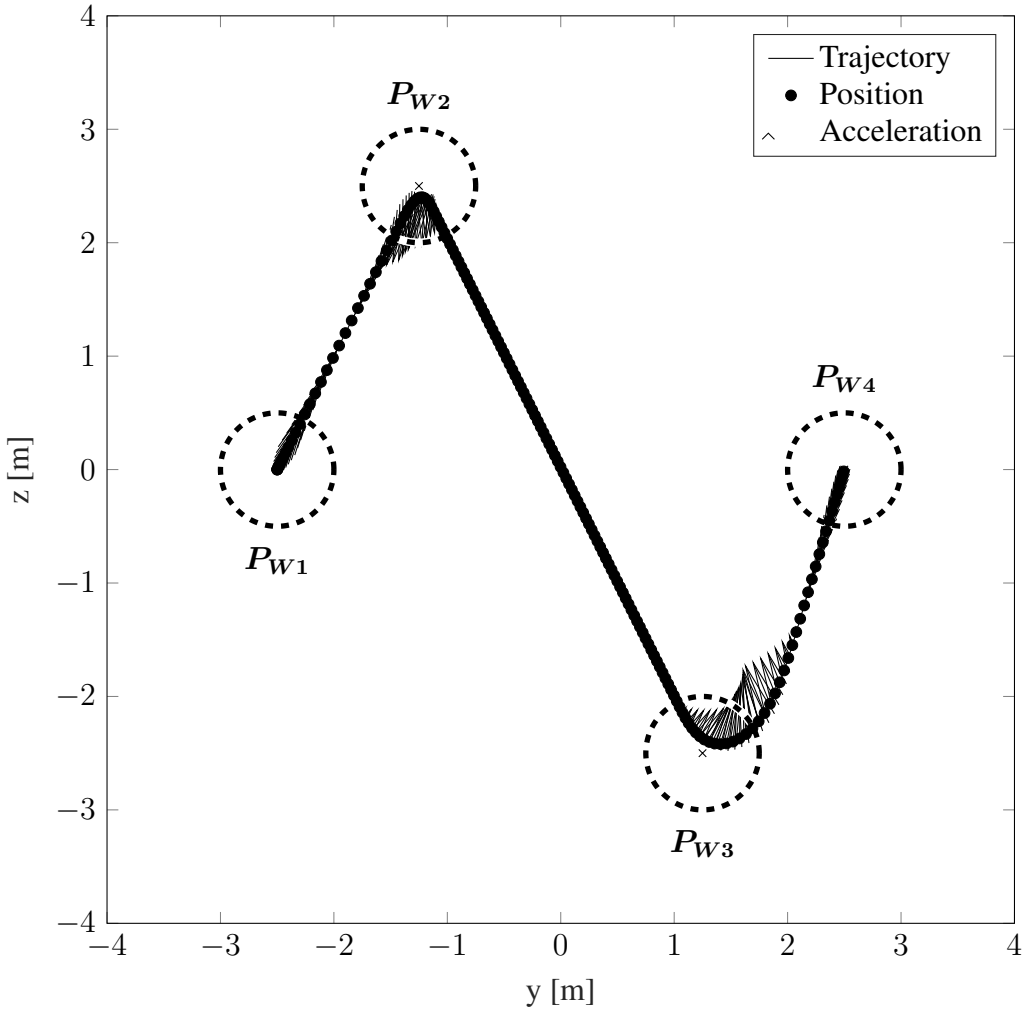

Figure 4.10. An example of the waypoint following the model using jerk-limited motion model with acceleration is shown in the figure. Waypoints are denoted by P_{Wn} and the acceptance circles are marked with a dotted line.

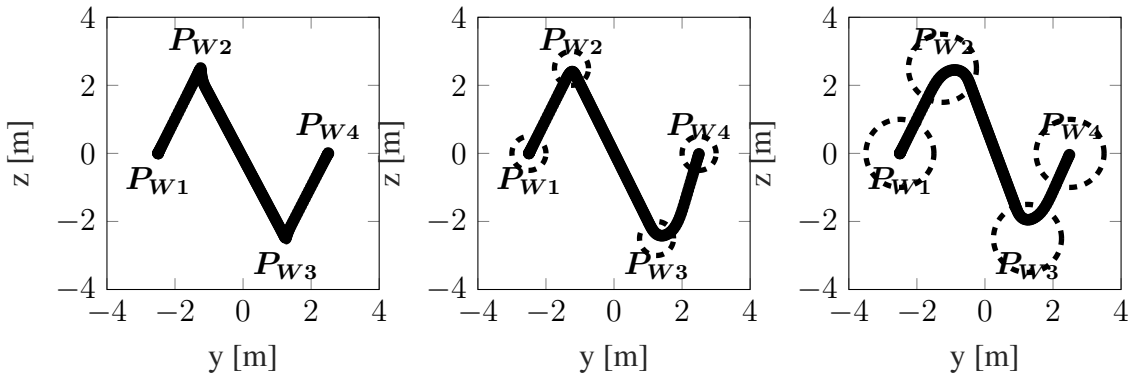

(**a**) (**b**) (**c**)

Figure 4.11. Example trajectories for the same waypoint placement and different acceptance radii. (**a**) $r_a = 0.1\,\mathrm{m}$, (**b**) $r_a = 0.5\,\mathrm{m}$, (**c**) $r_a = 1\,\mathrm{m}$.

compute d_n
while $d_n < r_a$ **do**
  $n \leftarrow n + 1$
  compute d_n
  if $n > N$ **then**
    break, trajectory is complete
  end if
end while

Algorithm 1: Waypoints following.

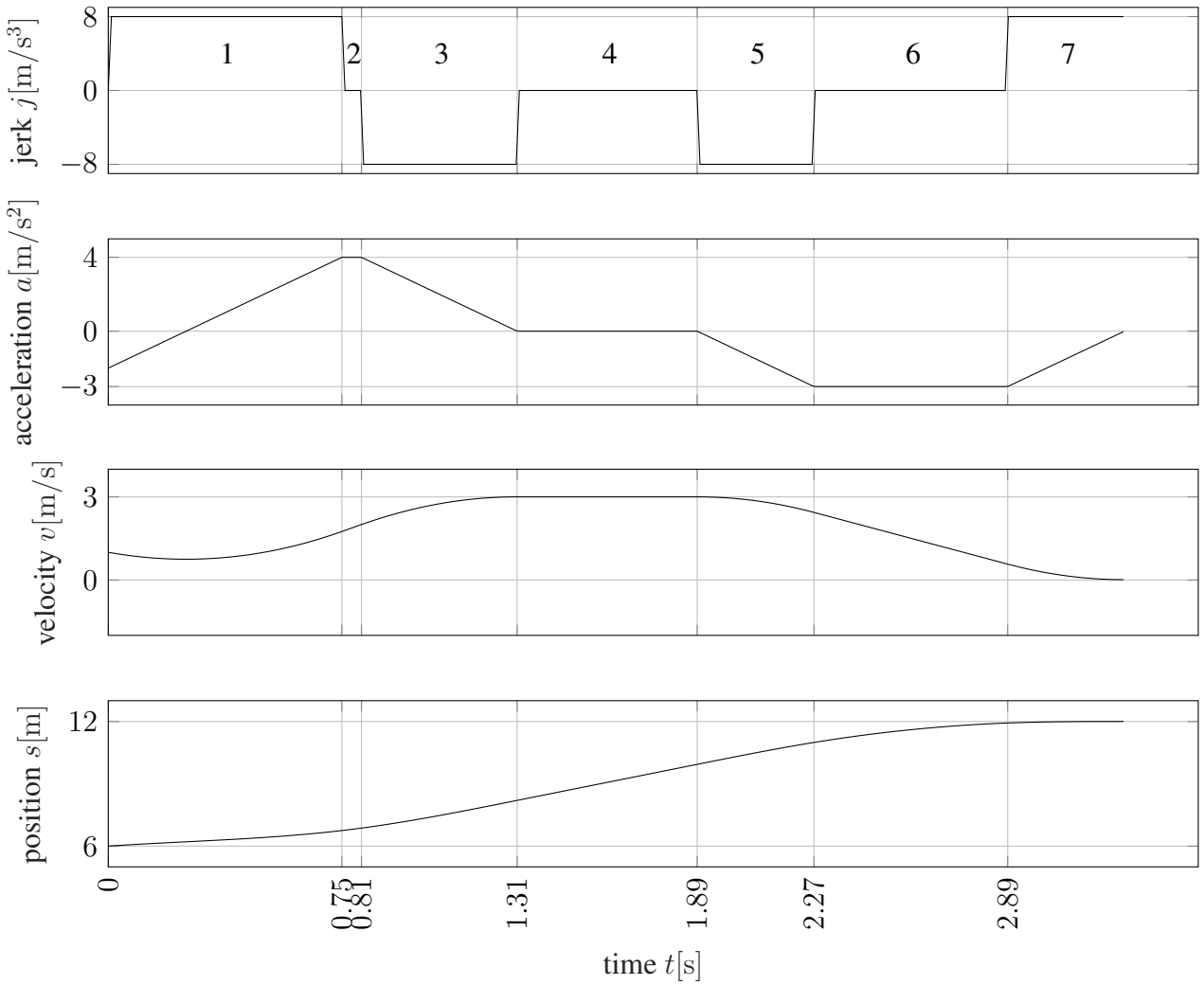

Figure 4.12. Detailed example of jerk-limited motion model.

3. Decreasing acceleration with maximum jerk until zero acceleration and maximum speed is reached.
4. Uniform motion with maximum speed.
5. Increasing deceleration until maximum deceleration is reached.

6. Decreasing speed with maximum deceleration.
7. Decreasing deceleration with maximum jerk until zero acceleration and zero velocity are reached.

Of course, the above description applies when the distance from the nearest waypoint is large enough. As the distance decreases, phase 4 is shortened. If phase 4 is shortened to zero, phases 2 and 6 are shortened concurrently. If they too reach zero, the remaining phases 1, 3, 5, 7 are shortened.

From a practical point of view, it is not reasonable to determine the platform movement parameters for the entire route to reach a waypoint, because:

1. Except for the last one, the waypoint is never reached, and the route would have to be recalculated after reaching the acceptance circle.
2. Controlling the platform's flight parameters is always subject to errors, hence corrections would have to be made. Even in the theoretical case of fully precise control, the influence of the center on the movement of the platform cannot be eliminated.
3. It would be necessary to take into account the initial conditions, since the platform has non-zero velocity and acceleration when it reaches the acceptance circle.

Taking this into account, the motion parameters (velocity, acceleration, and jerk) are determined at each time instant according to the following algorithm.

First, the vector of the remaining distance to be traveled is determined:

$$\boldsymbol{d} = \boldsymbol{P_P}(t) - \boldsymbol{P_{Wn}}, \tag{4.18}$$

and the distance, which is the norm of this vector:

$$d = \|\boldsymbol{d}\|. \tag{4.19}$$

Directional vectors along and across the route are also determined:

$$\boldsymbol{x}_{\parallel} = \frac{\boldsymbol{d}}{d}, \tag{4.20}$$

$$\boldsymbol{x}_{\perp} = \begin{cases} \frac{\boldsymbol{x}_{\parallel} \times \boldsymbol{v} \times \boldsymbol{x}_{\parallel}}{\left\| \boldsymbol{x}_{\parallel} \times \boldsymbol{v} \times \boldsymbol{x}_{\parallel} \right\|} & \text{if } \left\| \boldsymbol{x}_{\parallel} \times \boldsymbol{v} \right\| \neq 0, \\ \frac{\boldsymbol{x}_{\parallel} \times \boldsymbol{a} \times \boldsymbol{x}_{\parallel}}{\left\| \boldsymbol{x}_{\parallel} \times \boldsymbol{a} \times \boldsymbol{x}_{\parallel} \right\|} & \text{if } \left\| \boldsymbol{x}_{\parallel} \times \boldsymbol{v} \right\| = 0 \text{ and } \left\| \boldsymbol{x}_{\parallel} \times \boldsymbol{a} \right\| \neq 0, \\ [0,0,0]^T & \text{otherwise,} \end{cases} \tag{4.21}$$

where $\boldsymbol{v}$ is the radar platform velocity vector, $\boldsymbol{a}$ is the radar platform acceleration vector and $\times$ denotes the cross product.

Then the current components of the motion parameters along and across the route at a given time instant t are determined:

$$\boldsymbol{a}_{\parallel} = \boldsymbol{a} \cdot \boldsymbol{x}_{\parallel}, \tag{4.22}$$

$$\boldsymbol{v}_{\parallel} = \boldsymbol{v} \cdot \boldsymbol{x}_{\parallel}, \tag{4.23}$$

$$\boldsymbol{a}_{\perp} = \boldsymbol{a} \cdot \boldsymbol{x}_{\perp}, \tag{4.24}$$

$$\boldsymbol{v}_{\perp} = \boldsymbol{v} \cdot \boldsymbol{x}_{\perp}, \tag{4.25}$$

and their scalar values:

$$a_{\parallel} = \left\|\boldsymbol{a}_{\parallel}\right\|, \tag{4.26}$$

$$v_{\parallel} = \left\|\boldsymbol{v}_{\parallel}\right\|, \tag{4.27}$$

$$a_{\perp} = \left\|\boldsymbol{a}_{\perp}\right\|, \tag{4.28}$$

$$v_{\perp} = \left\|\boldsymbol{v}_{\perp}\right\|. \tag{4.29}$$

The braking distance along the route, that is, the minimum distance the platform travels before it reaches zero speed and acceleration in the direction along the route, is determined. The first step is to determine $a_{0\parallel}$, which is the theoretical minimum acceleration value that is achieved during braking:

$$a_{0\parallel} = -\sqrt{v_{\parallel} j + \frac{1}{2} a_{\parallel}^2}. \tag{4.30}$$

Then, depending on whether such acceleration can be achieved, the distance is calculated:

$$d_b = \begin{cases} v_{\parallel} \frac{a_{\parallel} - a_{0\parallel}}{j} + \frac{1}{2} a_{\parallel} \left(\frac{a_{\parallel} - a_{0\parallel}}{j}\right)^2 - \frac{1}{6} \left(\frac{a_{\parallel} - a_{0\parallel}}{j}\right)^3 - \frac{1}{6} \frac{a_{0\parallel}^3}{j^2} & \text{if } a_{0\parallel} < a_{min}(x_{\parallel}), \\ v_{\parallel} \frac{a_{\parallel} - a_{min}(x_{\parallel})}{j} + \frac{1}{2} a_{\parallel} \left(\frac{a_{\parallel} - a_{min}(x_{\parallel})}{j}\right)^2 - \frac{1}{6} \left(\frac{a_{\parallel} - a_{min}(x_{\parallel})}{j}\right)^3 + \frac{1}{8} \frac{a_{\parallel}^4}{a_{min}(x_{\parallel}) j^2} + \\ \quad - \frac{1}{4} \frac{a_{\parallel}^2 a_{min}(x_{\parallel})}{j^2} - \frac{1}{2} \frac{v_{\parallel}^2}{a_{min}(x_{\parallel})} - \frac{1}{6} \frac{a_{min}^3(x_{\parallel})}{j^2} & \text{otherwise,} \end{cases} \tag{4.31}$$

where $a_{min}(x_{\parallel})$ denotes maximum acceleration in the direction opposite to $x_{\parallel}$ and is always negative.

When the braking distance d_b and peak negative acceleration $a_{0\parallel}$ are known, it is possible to determine the target acceleration according to algorithm 2.

In the direction across the route, it is necessary to reduce the speed and acceleration to zero. The maximum braking acceleration is determined analogous to the along the route direction (see (4.30)):

$$a_{0\perp} = -\sqrt{v_{\perp} j + \frac{1}{2} a_{\perp}^2}, \tag{4.32}$$

and then the target acceleration is determined according to algorithm 3.

compute d_b and $a_{0\parallel}$
if $a_{0\parallel} < a_{min}(x_\parallel)$ **then**
  $a_{0\parallel} \leftarrow a_{min}(x_\parallel)$
end if
if $d_n \leq d_b$ **then**
  if $d_n \leq -\frac{1}{6}\frac{a_{0\parallel}^3}{j^2}$ **then**
    $a_{T\parallel} \leftarrow 0$
  else
    $a_{T\parallel} \leftarrow a_{0\parallel}$
  end if
else if $a_\parallel^2 \geq 2j\left(v_{max}(x_\parallel) - v_\parallel\right)$ **then**
  $a_{T\parallel} \leftarrow 0$
else
  $a_{T\parallel} \leftarrow a_{max}(x_\parallel)$
end if

Algorithm 2: Target acceleration in the direction along the route.

compute $a_{0\perp}$
if $a_{0\perp} < a_{min}(x_\perp)$ **then**
  $a_{0\perp} \leftarrow a_{min}(x_\perp)$
end if
if $v_\perp > \frac{1}{2}\frac{a_{0\perp}^2}{j}$ **then**
  $a_{T\perp} \leftarrow a_{0\perp}$
else
  $a_{T\perp} \leftarrow 0$
end if

Algorithm 3: Target acceleration in the direction across the route.

At the last step, the jerk at a time instant t is determined:

$$\boldsymbol{j}_\parallel = \begin{cases} 0 & \text{if } a_{T\parallel} \approx 0, \\ j \operatorname{sgn} a_{T\parallel} & \text{otherwise}, \end{cases} \tag{4.33}$$

$$\boldsymbol{j}_\perp = \begin{cases} 0 & \text{if } a_{T\perp} \approx 0, \\ j \operatorname{sgn} a_{T\perp} & \text{otherwise}, \end{cases} \tag{4.34}$$

$$\boldsymbol{j} = \boldsymbol{j}_\parallel + \boldsymbol{j}_\perp, \tag{4.35}$$

where sgn is a sign function. The rest of the motion parameters at the next time instant are determined by the laws of physics:

$$\boldsymbol{a}(t+\Delta t) = \boldsymbol{a}(t) + \boldsymbol{j}(t)t, \tag{4.36}$$

$$\boldsymbol{v}(t+\Delta t) = \boldsymbol{v}(t) + \boldsymbol{a}(t)t + \frac{1}{2}\boldsymbol{j}(t)t^2, \tag{4.37}$$

$$\boldsymbol{d}(t+\Delta t) = \boldsymbol{d}(t) + \boldsymbol{v}(t)t + \frac{1}{2}\boldsymbol{a}(t)t^2 + \frac{1}{6}\boldsymbol{j}(t)t^3. \tag{4.38}$$

The above calculations are repeated for all time moments Δt apart until the last waypoint is reached.

4.8. PSF and Quality Metrics Calculation

Once the trajectory (aperture) is established, it is possible to determine its PSF, enabling the calculation of quality metrics and facilitating tuning. The PSF calculation takes place on the $x = 0$ plane, within the range

$$y \in \left(-\frac{D_H}{2}, \frac{D_H}{2}\right), \tag{4.39}$$

$$z \in \left(-\frac{D_V}{2}, \frac{D_V}{2}\right). \tag{4.40}$$

The PSF is determined according to (2.8):

$$s(\boldsymbol{p}) = \sum_{n=1}^{n=N} \exp\left(j2\pi\frac{r_n}{\lambda}\right) \mathrm{sinc}\left(\frac{r_n}{\frac{c}{2B}}\right). \tag{4.41}$$

When the PSF is determined, it is possible to proceed to the determination of measures of imaging quality, namely SR, PSLR, ISLR. Main lobe extraction is required to determine these parameters. The following subsections describe the procedure for numerical main lobe extraction and determination of imaging quality parameters.

4.8.1. Main lobe Extraction

The extraction of the main lobe is necessary to determine its size, which is directly related to the resolution, and it also allows one to determine which PSF points belong to the main lobe and which to the side lobe, so that PSLR and ISLR can be calculated. The flood fill algorithm, described in Algorithm 4, is used for extraction. An exemplary result of the main lobe extraction algorithm is presented in Figure 4.13.

Initialize empty queue;
push $(0, 0)$ into queue;
while *queue not empty* **do**
    pop n from queue;
    mark $n \in ML$;
    foreach $\delta_n \in (1, 0), (0, 1), (-1, 0), (0, -1)$ **do**
        if $n + \delta_n$ *not in queue* **and** $I(n + \delta_n) \leq I(n)$ **and** $(n + \delta_n) \notin ML$ **then**
            push $(n + \delta_n)$ into queue;
        end
    end
end

Algorithm 4: Flood Fill.

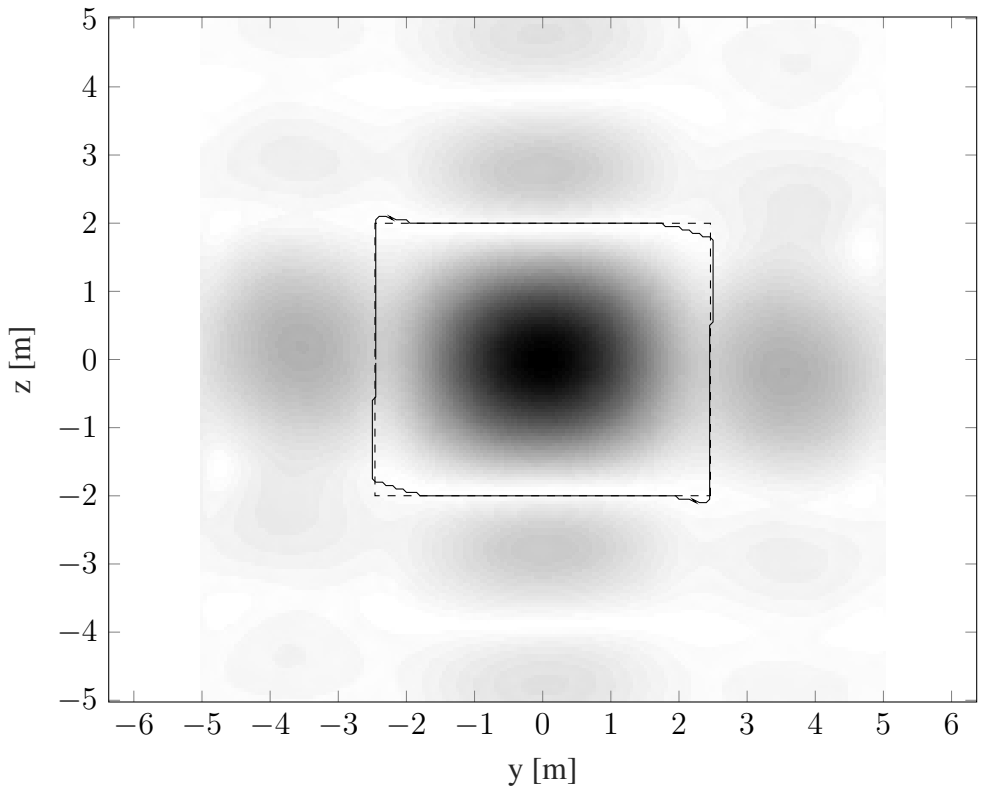

Figure 4.13. Main Lobe extraction. Solid line outlines the extracted main lobe, the dashed line presents the equivalent rectangular main lobe for resolution estimation

4.8.2. Spatial Resolution Estimation

Since in the case of uneven sampling of the synthetic aperture surface, the shape of the main lobe deviates from a rectangle, it is necessary to develop an equivalent measure of resolution. It

is determined as $\tilde{\delta_V}(\alpha_0)$ and $\tilde{\delta_H}(\alpha_0)$ where:

$$\alpha_0 = \underset{\alpha \in (0, \frac{\pi}{2})}{\arg\min} \left(\arctan\left(\frac{\tilde{\delta_V}(\alpha)}{\tilde{\delta_H}(\alpha)} \right) - \alpha \right), \tag{4.42}$$

and

$$\tilde{\delta_V}(\alpha) = |\bar{p_{oVz}}|, \tag{4.43}$$

$$\tilde{\delta_H}(\alpha) = |\bar{p_{oHy}}|. \tag{4.44}$$

Vertical and horizontal outlines p_{oVz} and p_{oHy} are the z and y coordinates of the point sets defined as:

$$\boldsymbol{p_{oi}} \in \boldsymbol{p_{oV}} \Leftrightarrow \arctan|\frac{p_{oiz}}{p_{oiy}}| > \alpha, \tag{4.45}$$

$$\boldsymbol{p_{oi}} \in \boldsymbol{p_{oH}} \Leftrightarrow \arctan|\frac{p_{oiz}}{p_{oiy}}| < \alpha. \tag{4.46}$$

The main lobe outline is obtained by determining such PSF pixels that do not belong to the main lobe, but are adjacent to pixels belonging to the main lobe:

$$\boldsymbol{p_i} \in \boldsymbol{p_o} \Leftrightarrow \boldsymbol{p_i} \notin \boldsymbol{p_{ML}} \wedge \exists \boldsymbol{p_j} \in \boldsymbol{p_{ML}} : \boldsymbol{p_j} = \boldsymbol{p_i} + \boldsymbol{\delta}, \boldsymbol{\delta} \in \{(1,0),(0,1),(-1,0),(0,-1)\}. \tag{4.47}$$

This provides a measure of the equivalent resolution that would be achieved with a theoretical PSF with a main lobe of rectangular shape closest to the PSF under analysis.

4.8.3. PSLR and ISLR Estimation

When the main lobe is extracted, PSLR can be calculated according to the Formula (2.20):

$$\mathrm{PSLR} = 20\log_{10}\left(\frac{\max\limits_{\boldsymbol{p} \in \boldsymbol{p_{SL}}} [s(\boldsymbol{p})]}{\max\limits_{\boldsymbol{p} \in \boldsymbol{p_{ML}}} [s(\boldsymbol{p})]} \right), \tag{4.48}$$

and ISLR according to the Formula (2.21):

$$\mathrm{ISLR} = 20\log_{10}\left(\frac{\sum\limits_{\boldsymbol{p} \in \boldsymbol{p_{SL}}} [s(\boldsymbol{p})]}{\sum\limits_{\boldsymbol{p} \in \boldsymbol{p_{ML}}} [s(\boldsymbol{p})]} \right), \tag{4.49}$$

where $s(\boldsymbol{p})$ is the PSF at the point $\boldsymbol{p}$, $\boldsymbol{p} \in \boldsymbol{p_{SL}}$ denotes points in the side lobe and $\boldsymbol{p} \in \boldsymbol{p_{ML}}$ denotes points in the main lobe.

4.9. Cost Function

Once the values of the quality parameters are known, the last step needed to tune the aperture is to determine its cost. The value of the cost function for a given trajectory is the sum of the products of the transfer function values for each parameter and their weights:

$$k = w_{\delta_H} k_{\delta_H} + w_{\delta_V} k_{\delta_V} + w_{PSLR} k_{PSLR} + w_{ISLR} k_{ISLR} + w_t k_t, \tag{4.50}$$

where:

— k_{δ_H} is the cost related to the horizontal resolution,

— k_{δ_V} is the cost related to the vertical resolution,

— k_{PSLR} is the cost related to the PSLR,

— k_{ISLR} is the cost related to the ISLR,

— k_t is the cost related to the trajectory length,

and w_{δ_H}, w_{δ_V}, w_{PSLR}, w_{ISLR}, w_t are the corresponding weighting factors.

The weighting factors and fractional cost functions must be defined in a way that ensures the proper optimization goal, that the optimizers main goal is to ensure the proper imaging quality, and that the others costs do not prevail.

4.9.1. Transfer functions

Transfer functions are used to assign each trajectory parameter a cost value that is comparable in magnitude so that the cost of the trajectory can be determined. Two types of transfer functions are used in the model presented in this paper – a range-type transfer function and a step-type transfer function.

4.9.1.1. Range Transfer Function

The range-type transfer function is shown in Figure 4.14 and is defined by the formula:

$$k = \begin{cases} 0 & \text{if } u < u_L, \\ \frac{u-u_L}{u_U-u_L} & \text{if } u_L \leq u \leq u_U, \\ 1000\frac{u-u_U}{u_U-u_L} + 1 & \text{if } u_U < u, \end{cases} \tag{4.51}$$

where k is cost, u is value, u_L is the lower bound of the accepted parameter range, and u_U is the upper bound. This function should be applied to parameters for which an acceptable range of values can be specified, namely, resolution, PSLR, and ISLR. In the range between u_L and u_U, changing the value of the parameter has little effect on the cost, crossing the upper threshold of the range causes a significant increase in cost, while crossing the lower threshold does not affect the cost. It can be seen that by giving u_L equal to zero, it is possible to minimize one of the parameters without a lower limit, and by giving $u_L = u_U$ a threshold value is obtained.

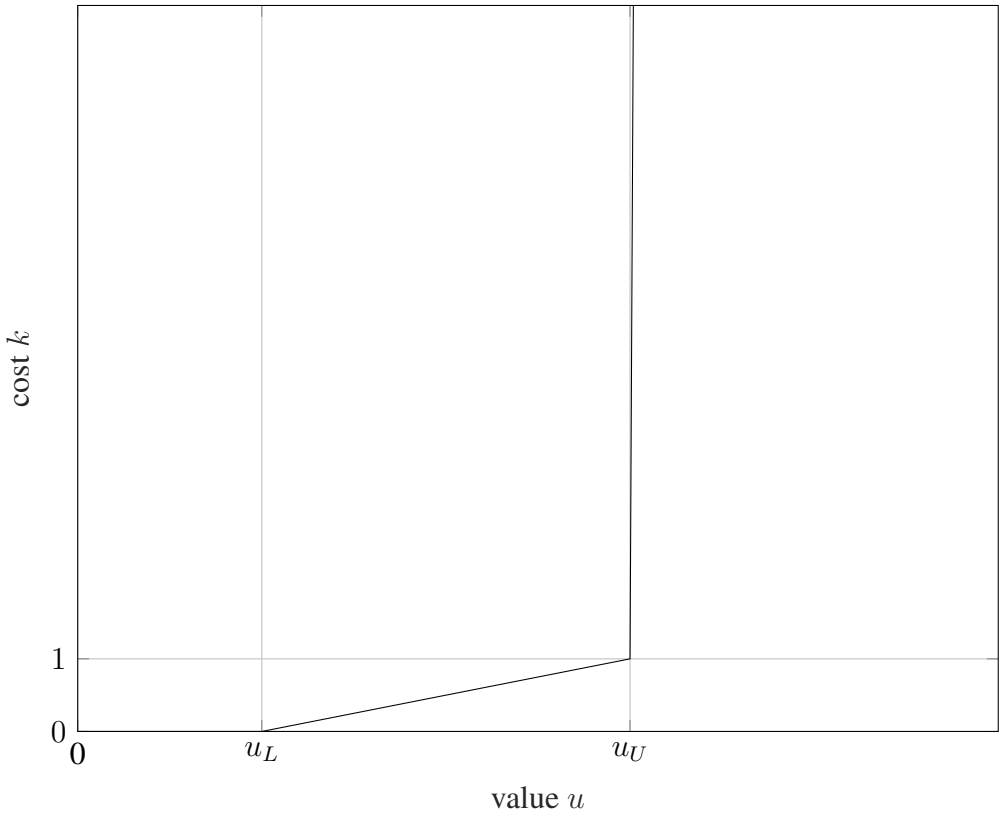

Figure 4.14. Range-type transfer function.

4.9.1.2. Step-type Transfer Function

Step-type transfer function is presented in Figure 4.15 and is defined by the formula:

$$k = \begin{cases} \lfloor \frac{u}{u_U} \rfloor (1 + k_s) + \frac{\text{mod } (u,u_U)}{u_U} & \text{if} \quad \text{mod } (u, u_U) \leq u_U - \frac{k_S u_U}{1000}, \\ \lfloor \frac{u}{u_U} \rfloor (1 + k_s) + 1000 \frac{\text{mod } (u,u_U)}{u_U} + 1 + k_S - 1000 & \text{otherwise}, \end{cases} \tag{4.52}$$

where u_U is the platform operating time provided by the full energy source, with a margin to return to the starting point, k_s is the value corresponding to the cost of charging or replacing the platform's energy source relative to the cost of depleting the entire energy source, and $\text{mod } (a, b)$ denotes modulo operator defined as the remainder of a division a/b. This function is designed to determine the cost associated with the duration of the platform's flight along the trajectory, taking into account the finite capacity of the energy source and the non-zero cost of replacing/charging the energy source[2].

[2] In this work, the term energy source replacement/recharging is used to refer to an electrically powered platform. In the case of a platform with another type of propulsion system, the term should be understood as "a set of activities aimed at restoring the platform's energy source to its original state," i.e. in the case of a fuel-powered platform, it would be filling the tank with fuel, for example.

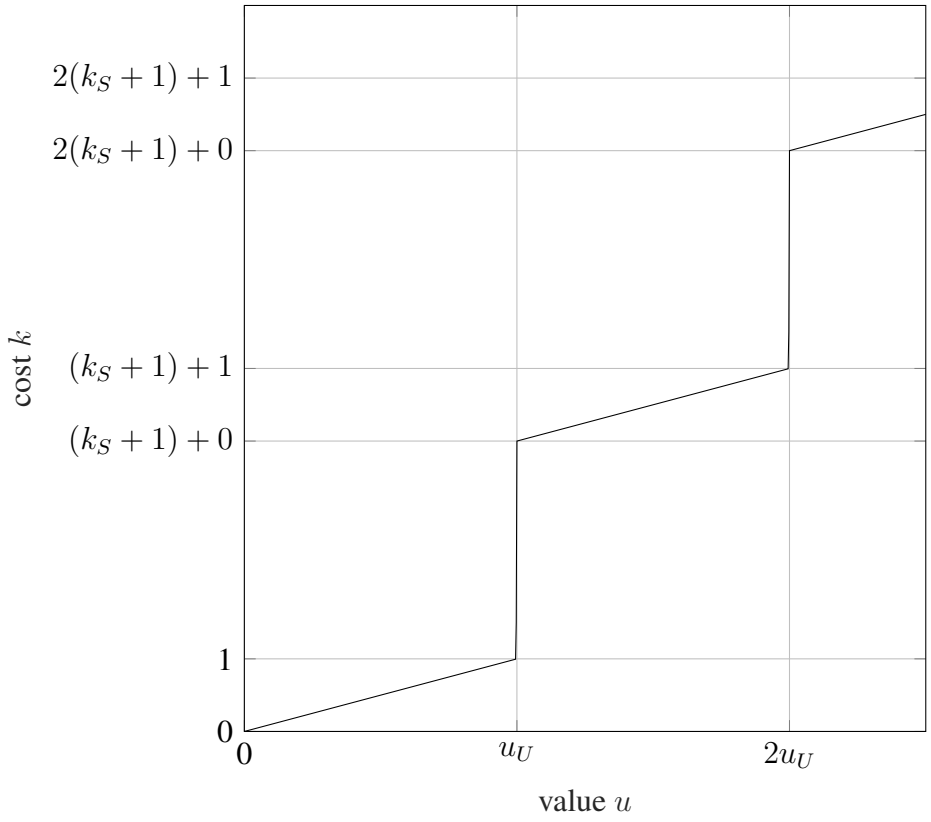

Figure 4.15. Step-type transfer function.

4.9.2. Weights

The weights are used to determine which aperture parameter is most important. In this study, the sum of the weights is assumed to be equal to one:

$$\sum w = w_{\delta_H} + w_{\delta_V} + w_{PSLR} + w_{ISLR} + w_t = 1. \tag{4.53}$$

Some weights may be zero when some parameters affecting the cost are irrelevant to the scenario, for example, when only PSLR and not ISLR is relevant.

4.10. Trajectory tuning

Trajectory optimization involves minimizing a multidimensional, nonlinear, non-convex cost function whose argument is the waypoint location:

$$\boldsymbol{P_{WOpt}} = \arg\min_{\boldsymbol{P}} k(\boldsymbol{P}), \tag{4.54}$$

where $\boldsymbol{P_{WOpt}}$ is the set of optimized waypoints and $\boldsymbol{P}$ is the superset of the set of waypoints covered by the optimization procedure. There are numerous algorithms for optimizing convex problems [69]. Some of them require the function to be differentiable, and others do not. A much more serious issue is non-convex optimization. There are various approaches, the most

popular of which is to divide the function area into subareas, using different starting points, and applying convex optimization. Subarea partitioning can be implemented in a way that ensures that a global extremum is reached, but it requires a deep analysis of the function. In this paper, the approach of using different starting points is used.

The optimization of the cost function is carried out using the Nelder-Mead algorithm [90], which is available in the MATLAB package[91]. This algorithm is suitable for minimizing non-differentiable functions as it does not require the calculation of a gradient. The algorithm works by using a simplex, which is a 2N-dimensional shape in the input data space (two coordinates of N waypoints form a 2N-dimensional space). The algorithm determines the values of the minimized function at the vertices of the simplex and subsequently moves the simplex or changes its shape to reach a local minimum. The algorithm minimizing function $c(\boldsymbol{P})$ consists of the following steps [29]:

1. Initial simplex: create a simplex consisting of $2N + 1$ points around a starting point, including the starting point.
2. Sort the points so that the function values are in ascending order $c(\boldsymbol{P_1}) \leq c(\boldsymbol{P_2}) \leq \ldots \leq c(\boldsymbol{P_{2N+1}})$.
3. Determine the centroid $\boldsymbol{P_0}$ of the simplex, excluding the worst point $\boldsymbol{P_{2N+1}}$: $\boldsymbol{P_0} = \mathrm{A}(\boldsymbol{P_1} \ldots \boldsymbol{P_{2N}})$, where $\mathrm{A}(\cdot)$ denotes mean.
4. Reflection: determine the reflected point $\boldsymbol{P_r} = \boldsymbol{P_0} + k_\alpha(\boldsymbol{P_0} - \boldsymbol{P_{2N+1}})$, where k_α is the reflection coefficient. If $\boldsymbol{P_r}$ is the best point $c(\boldsymbol{P_r}) < c(\boldsymbol{P_1})$, go to step 5. If it is the worst point $c(\boldsymbol{P_r}) > c(\boldsymbol{P_{2N+1}})$, go to step 6. If it is the second worst $c(\boldsymbol{P_{2N}}) < c(\boldsymbol{P_r}) < c(\boldsymbol{P_{2N+1}})$, go to step 7. Otherwise, add it to the simplex in place of $\boldsymbol{P_{2N+1}}$ and go back to step 1.
5. Expansion: determine the expanded point: $\boldsymbol{P_e} = \boldsymbol{P_0} + k_\gamma(\boldsymbol{P_r} - \boldsymbol{P_0})$, where k_γ is the expansion coefficient. If it is better than reflected, add it in place of $\boldsymbol{P_{2N+1}}$. Otherwise, add reflected. Return to step 1.
6. Contract inside: determine the contracted point $\boldsymbol{P_c} = \boldsymbol{P_0} + k_\rho(\boldsymbol{P_{2N+1}} - \boldsymbol{P_0})$, where k_ρ is the contraction coefficient, and if it is not the worst, put it in place of the worst and return to step 1. Otherwise, go to step 8.
7. Contract outside: determine the contracted point $\boldsymbol{P_c} = \boldsymbol{P_0} + k_\rho(\boldsymbol{P_r} - \boldsymbol{P_0})$, where k_ρ is the contraction coefficient, and if it is better than reflected, replace the worst with it and return to step 1. Otherwise, go to step 8.
8. Shrink: reduce the size of the simplex: $\forall i > 1 : \boldsymbol{P_i} = \boldsymbol{P_1} + k_\sigma(\boldsymbol{P_i} - \boldsymbol{P_1})$, where k_σ is shrink coefficient.

The algorithm stops when the iteration limit has been reached or when both the simplex size and the difference between the function values are below certain thresholds: $\max(|\boldsymbol{P_i} - \boldsymbol{P_j}|) <$

T_P and $|c(\boldsymbol{P_{2N+1}}) - c(\boldsymbol{P_1})| < T_c$, where T_P is the argument step threshold, and T_c is the function step threshold. The values used in this work are as follows: the iteration limit is 3000, the argument step threshold and the function step threshold $T_P = T_c = 0.0001$, and the coefficients used in the algorithm are $k_\alpha = 1$, $k_\gamma = 2$, $k_\rho = 0.5$, $k_\sigma = 0.5$.

4.10.1. Final trajectory

The final trajectory is the one with the lowest cost. It should be noted that the actual trajectory realized by the radar platform may differ from the simulated one, mainly due to the influence of the environment, but thanks to the use of a real motion model of the platform in the simulation, the differences are not significant.

5. Results and Discussion

In this chapter, the results of the algorithm are presented - in the first section, simulation results showing the performance of the algorithm in a certain assumed scenario and analysing the impact of the algorithm's parameters on its performance. The second section presents the results of an actual experiment using a radar platform simulator to demonstrate 3D SAR imaging using a real radar system.

5.1. Simulations

5.1.1. Scenario Overview

In the assumed scenario, the distance to the object is assumed to be 1000 meters, well above the typical lidar range, which is usually a few hundred meters. A K-band radar with a bandwidth of 3 GHz is used as the sensor. These parameters replicate the actual radar that is used for experiments with the multi-rotor [92]. The radar and scenario parameters are shown in Table 5.1. The platform's motion parameters are the same as in Table 4.1. Expected resolution is set to 0.2 by 0.5 meters.

5.1.2. Simulation Flow – First Tuning Process with Strict Requirements

To determine the initial parameters of the trajectory to be tuned, an MBSAR trajectory called the reference trajectory is determined for the given scenario requirements, the dimensions of which are determined according to (4.8) and (4.9):

$$L_V = \frac{r\lambda}{2\delta_V}, \tag{5.1}$$

$$L_H = \frac{r\lambda}{2\delta_H}. \tag{5.2}$$

Such dimensions ensure that the desired resolution is achieved. The distance between successive runs is determined by(3.2):

$$d_V = \frac{\lambda R}{D_V}. \tag{5.3}$$

This spacing ensures that the distance from the imaging center to the first grating lobe is no less than the vertical dimension of the ROI. The reference trajectory for the test scenario and its

Parameter	Symbol	Value
ROI horizontal dimension	D_H	$10\,\mathrm{m}$
ROI vertical dimension	D_V	$5\,\mathrm{m}$
distance to ROI	r_0	$1000\,\mathrm{m}$
Carrier Frequency	f_c	$24\,\mathrm{GHz}$
Bandwidth	B	$3\,\mathrm{GHz}$
horizontal beamwidth	θ_H	$10\,^\circ$
vertical beamwidth	θ_V	$20\,^\circ$
Maximum jerk	j_{max}	$8\,\mathrm{m/s^3}$
Maximum horizontal acceleration	$a_{H\,max}$	$5\,\mathrm{m/s^2}$
Maximum upwards acceleration	$a_{V\uparrow max}$	$4\,\mathrm{m/s^2}$
Maximum downwards acceleration	$a_{V\downarrow max}$	$3\,\mathrm{m/s^2}$
Maximum horizontal velocity	$v_{H\,max}$	$12\,\mathrm{m/s}$
Maximum upwards velocity	$v_{V\uparrow max}$	$3\,\mathrm{m/s}$
Maximum downwards velocity	$v_{V\downarrow max}$	$1\,\mathrm{m/s}$
Expected horizontal resolution	$\delta_{H\,\mathrm{ref}}$	$0.2\,\mathrm{m}$
Expected vertical resolution	$\delta_{V\,\mathrm{ref}}$	$0.5\,\mathrm{m}$

Table 5.1. Radar system and scenario parameters used in simulation.

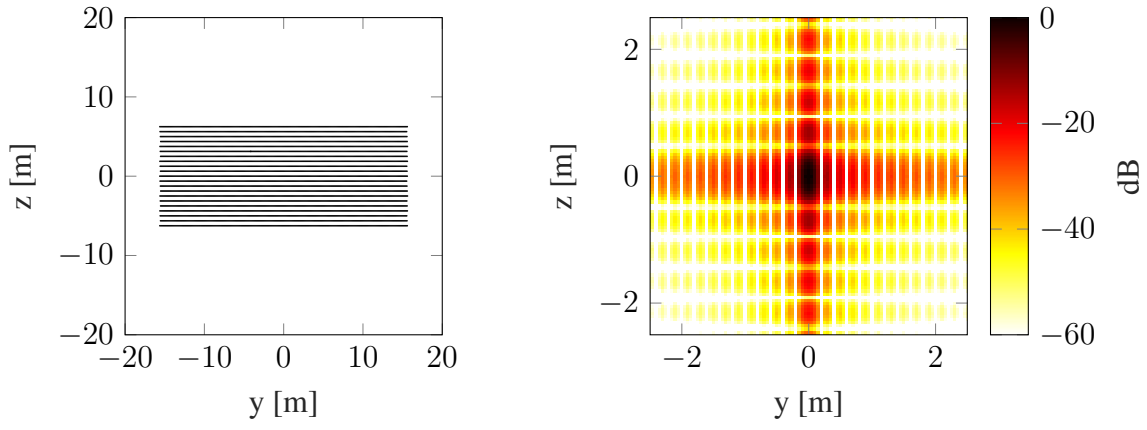

(a) **(b)**

Figure 5.1. Reference trajectory. **(a)** Trajectory, **(b)** 2D cross-range cross-section of 3D PSF.

PSF is shown in Figure 5.1. 3D PSF of that trajectory with limited dynamic range, along with a matching cross-section is presented in Figure 5.2.

The PSF of the reference trajectory is the starting point for tuning, as the parameters of the cost function are determined from it. In order to demonstrate the performance of the algorithm, it is assumed that the quality parameters of SR and PSLR should not be worse by more than 10 percent than the reference and need not be better by more than 10 percent, while ISLR is

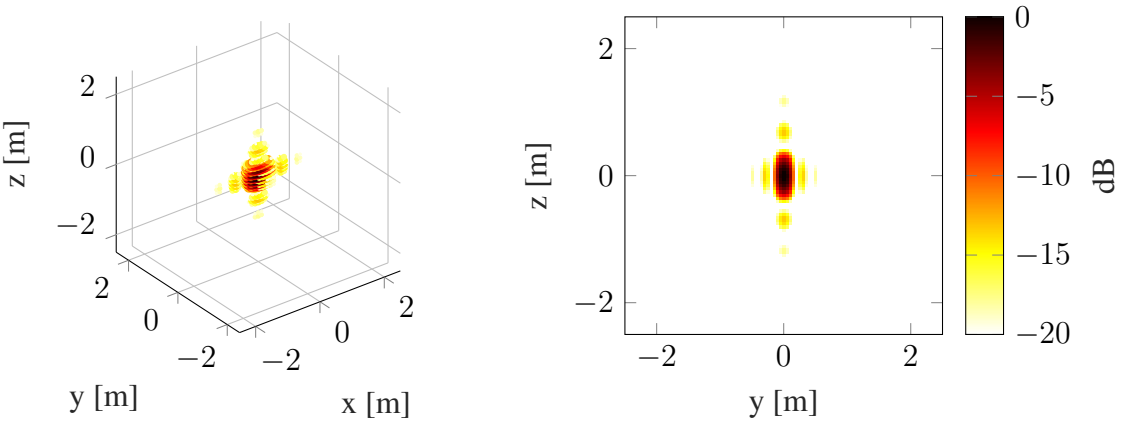

(a) **(b)**

Figure 5.2. Reference trajectory. **(a)** 3D PSF, **(b)** 2D cross-range cross-section of 3D PSF.

specified to be no worse than 500 percent of the reference value. Such a difference is a direct result of the fact that ISLR is very strongly determined by the number of synthetic aperture points, and since, according to the essence of the algorithm, the resulting trajectory should be shorter than the reference, its ISLR is larger. It is assumed that the measurement time must be as short as possible and, in particular, no greater than the reference time. The reference parameters are collected in Table 5.2.

Parameter	**Lower value**	**Upper value**	**Weight**
δ_H	$0.9\delta_{H\,\mathrm{ref}}$	$1.1\delta_{H\,\mathrm{ref}}$	0.3
δ_V	$0.9\delta_{V\,\mathrm{ref}}$	$1.1\delta_{V\,\mathrm{ref}}$	0.3
PSLR	$0.9\mathrm{PSLR}_{\mathrm{ref}}$	$1.1\mathrm{PSLR}_{\mathrm{ref}}$	0.2
ISLR	$\mathrm{ISLR}_{\mathrm{ref}}$	$5\mathrm{ISLR}_{\mathrm{ref}}$	0.1
t	-	t_{ref}	0.1

Table 5.2. Tuning goals – strict requirements.

Another important step in defining the parameters of the tuning process is the choice of weights. It depends solely on the specific requirements of the scenario; in this case, the highest weight is assigned to the resolution, the middle weight to the PSLR, and the lowest to the ISLR and flight time - see Table 5.2.

When all input parameters are defined, the algorithm can start working. The first step is to determine the number of waypoints according to the formula:

$$N = \left\lfloor \frac{L_V D_V}{\lambda r_0} \right\rfloor, \tag{5.4}$$

where L_V is the vertical span of the synthetic aperture and D_V is the vertical size of the ROI. A preliminary trajectory is then determined, which is then tuned.

To increase the chance of the tuning process achieving a local minimum with a value close to the global minimum, tuning is carried out repeatedly for different initial trajectories. At the end, the final trajectory with the lowest cost from all tuning processes is selected.

In this experiment, 10 tuning processes were carried out. Figure 5.3 shows the dependence of the cost function value on the number of function calls of each process.

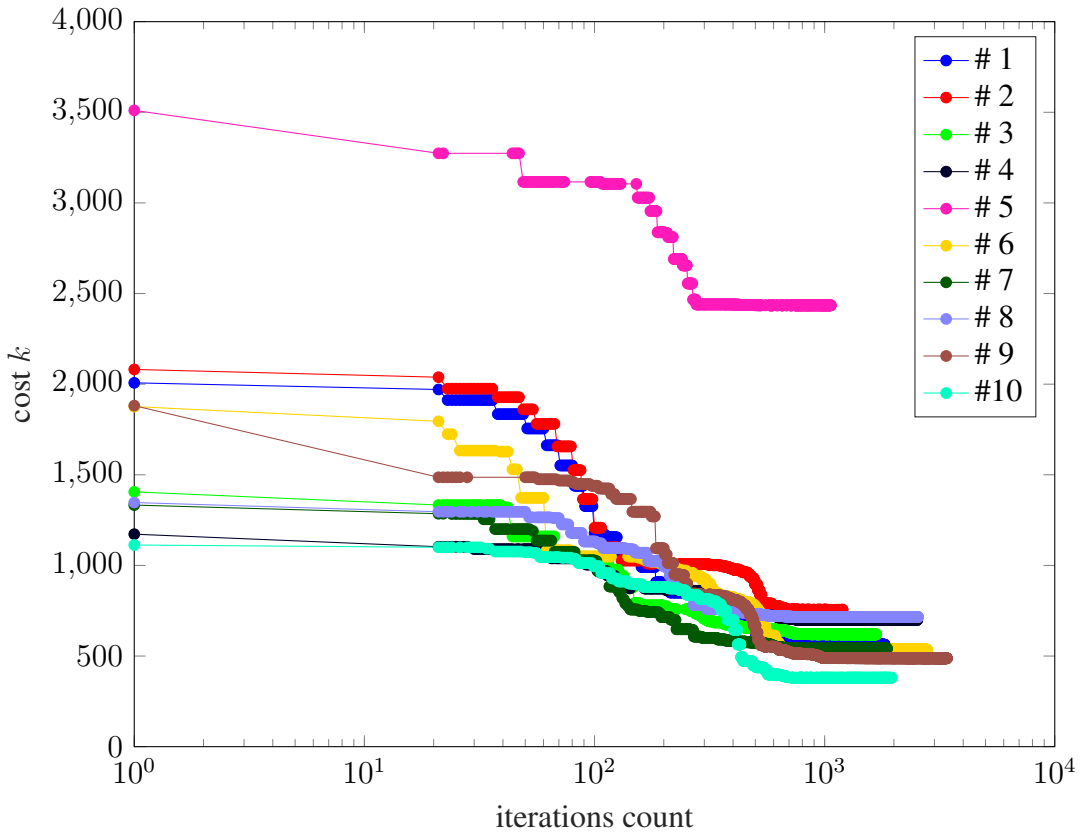

Figure 5.3. Cost versus function calls for a tuning process with strict requirements. Different runs are denoted with different colors.

It can be seen that with the requirements defined this way, for none of the runs the cost reaches a value of 1, i.e., the one at which all parameters are within an acceptable range. The starting and ending parameters for these runs are shown in Table 5.3.

5.1.3. Second Tuning Process with Relaxed Requirements

In order to see what effect the selection of requirements has on the tuning process, it is decided to relax the requirements, particularly for PSLR and ISLR – the new requirements are shown in Table 5.4.

To make the comparison meaningful, in this experiment, the runs have the same starting points. The relationship of the cost function value to the number of function calls for this experiment is shown in Figure 5.4.

run #	δ_H		δ_V		PSLR		ISLR		cost c	
	ini	fin	ini	fin	ini	fin	ini	fin	ini	fin
1	0.25	0.31	0.39	0.60	0.63	0.33	8.07	6.83	2007.29	562.54
2	0.26	0.28	0.39	0.40	0.65	0.34	7.57	8.18	2081.23	755.37
3	0.25	0.27	0.54	0.52	0.51	0.35	4.99	4.81	1405.89	619.55
4	0.29	0.30	0.57	0.57	0.40	0.37	5.52	4.92	1172.32	699.29
5	0.47	0.29	1.26	1.11	0.23	0.37	1.92	2.36	3510.53	2435.00
6	0.28	0.26	0.53	0.56	0.55	0.31	6.44	5.29	1876.36	534.95
7	0.25	0.29	0.48	0.50	0.49	0.34	6.54	5.69	1332.94	541.20
8	0.25	0.26	0.40	0.53	0.49	0.37	7.86	6.62	1346.87	715.48
9	0.25	0.25	0.78	0.62	0.39	0.33	3.83	3.93	1881.45	487.89
10	0.46	0.38	0.41	0.50	0.43	0.31	5.77	5.36	1112.73	380.09

Table 5.3. Initial and final quality requirements of ten runs – strict requirements.

Parameter	Lower Value	Upper Value	Weight
δ_H	$0.9\delta_{H\mathrm{ref}}$	$1.1\delta_{H\mathrm{ref}}$	0.3
δ_V	$0.9\delta_{V\mathrm{ref}}$	$1.1\delta_{V\mathrm{ref}}$	0.3
PSLR	$\mathrm{PSLR}_{\mathrm{ref}}$	$\mathbf{2}\mathrm{PSLR}_{\mathrm{ref}}$	0.2
ISLR	$\mathrm{ISLR}_{\mathrm{ref}}$	$\mathbf{10}\mathrm{ISLR}_{\mathrm{ref}}$	0.1
t	-	t_{ref}	0.1

Table 5.4. Tuning goals – relaxed requirements. Values changed with respect to strict requirements are **bold**.

run #	δ_H		δ_V		PSLR		ISLR		cost c	
	ini	fin	ini	fin	ini	fin	ini	fin	ini	fin
1	0.25	0.36	0.39	0.73	0.63	0.37	8.07	5.97	208.40	0.53
2	0.26	0.28	0.39	0.53	0.65	0.43	7.57	6.81	217.18	5.92
3	0.25	0.26	0.54	0.60	0.51	0.33	4.99	4.75	126.55	0.73
4	0.29	0.25	0.57	0.57	0.40	0.34	5.52	5.00	83.98	0.68
5	0.47	0.30	1.26	1.09	0.23	0.32	1.92	2.32	2528.21	1510.99
6	0.28	0.28	0.53	0.52	0.55	0.37	6.44	5.67	239.08	0.65
7	0.25	0.31	0.48	0.53	0.49	0.37	6.54	5.87	62.57	0.42
8	0.25	0.22	0.40	0.58	0.49	0.33	7.86	5.90	77.36	0.47
9	0.25	0.26	0.78	0.73	0.39	0.33	3.83	3.56	865.09	240.69
10	0.46	0.28	0.41	0.49	0.43	0.40	5.77	5.72	21.08	0.64

Table 5.5. Cost versus function calls for ten different runs of the tuning procedure.

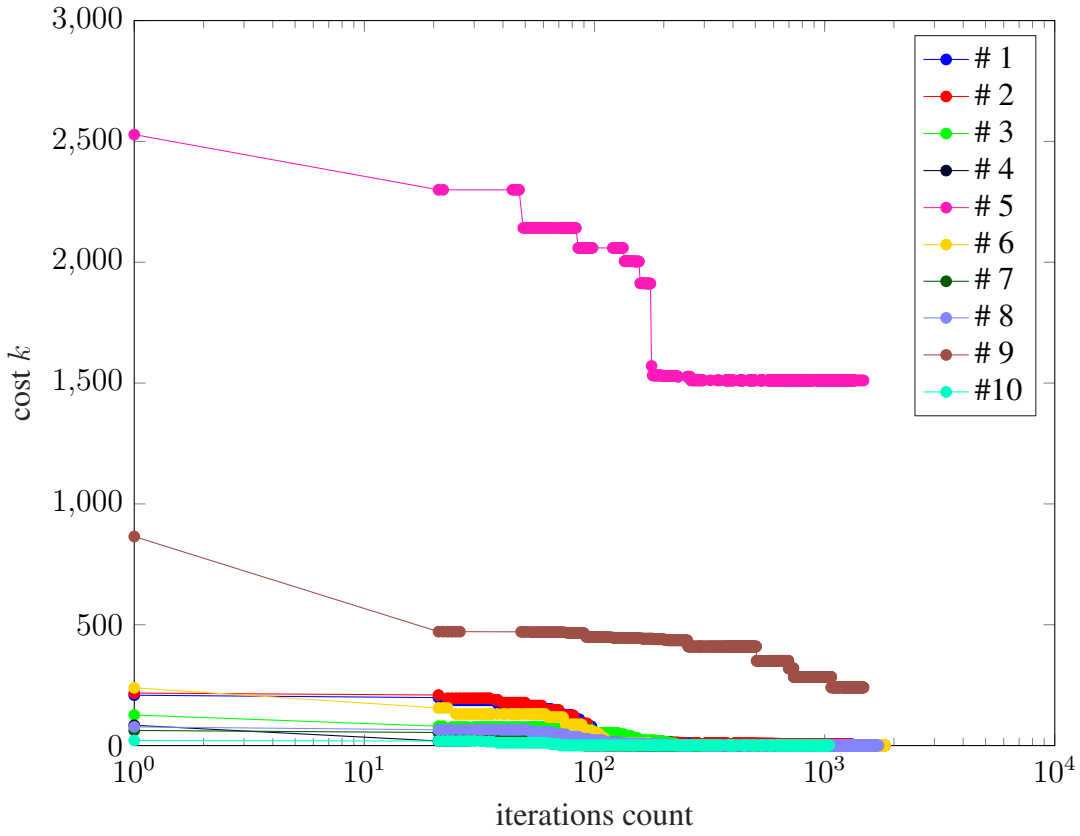

Figure 5.4. Cost versus function calls for a tuning process with relaxed requirements. Different runs are denoted with different colors.

It can be seen that, as in the previous case, the cost values for run # 5 are significantly higher than the other runs. In addition to this, run #9 also deviates from the others, which means that adjusting tuning goals changes the way the cost is determined and as a result also changes the course of the optimization process. In this particular case, the reason lies in the way the goals are changed – the main component of the high cost for run #5 and run #9 comes from the high value of vertical resolution, and the goal values of resolution were not changed. In the case of the other runs, the cost decreased significantly because it is high due to PSLR and ISLR, and the goals regarding those parameters were significantly relaxed. Detailed values of the parameters for each run are shown in Table 5.5.

To illustrate the final phase of the tuning process, Figure 5.5 shows the same relationship, but in a limited range of the y-axis. It can be seen that low cost values are reached long before

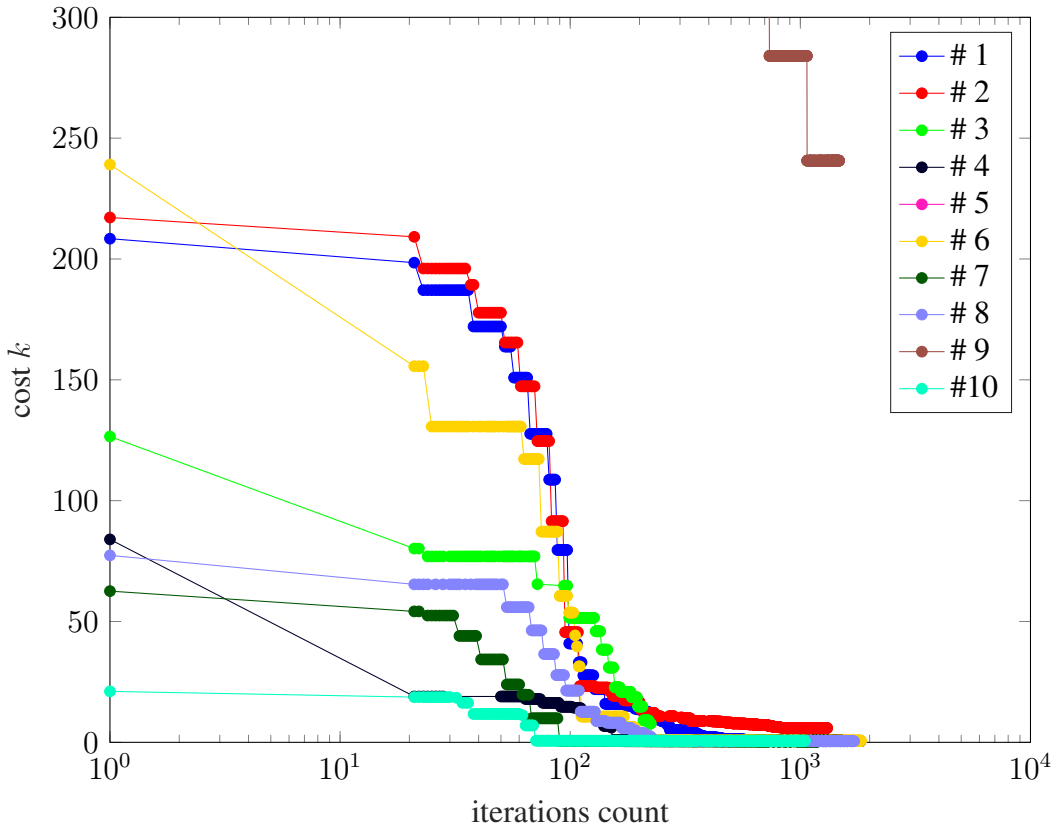

Figure 5.5. Cost versus function calls for a tuning process with relaxed requirements – reduced y-axis range. Different runs are denoted with different colors.

the tuning is completed. This leads to another experiment on tuning stop conditions.

run #	δ_H		δ_V		PSLR		ISLR		cost c	
	ini	fin	ini	fin	ini	fin	ini	fin	ini	fin
1	0.25	0.36	0.39	0.73	0.63	0.37	8.07	5.96	208.40	0.53
2	0.26	0.28	0.39	0.53	0.65	0.43	7.57	6.81	217.18	5.92
3	0.25	0.26	0.54	0.60	0.51	0.33	4.99	4.75	126.55	0.73
4	0.29	0.25	0.57	0.57	0.40	0.34	5.52	5.00	83.98	0.68
5	0.47	0.30	1.26	1.09	0.23	0.32	1.92	2.31	2528.21	1511.07
6	0.28	0.28	0.53	0.52	0.55	0.37	6.44	5.67	239.08	0.65
7	0.25	0.31	0.48	0.53	0.49	0.37	6.54	5.87	62.57	0.42
8	0.25	0.22	0.40	0.58	0.49	0.33	7.86	5.90	77.36	0.47
9	0.25	0.26	0.78	0.73	0.39	0.33	3.83	3.56	865.09	240.69
10	0.46	0.28	0.41	0.49	0.43	0.40	5.77	5.72	21.08	0.64

Table 5.6. Cost versus function calls for ten different runs of the tuning procedure.

5.1.4. Increased Tolerance – Third Experiment

To investigate how limiting the number of function calls would affect the results, the values of the parameters T_P and T_c were increased to 0.001. The results of the experiment are shown in Figure 5.1.4 and Table 5.6.

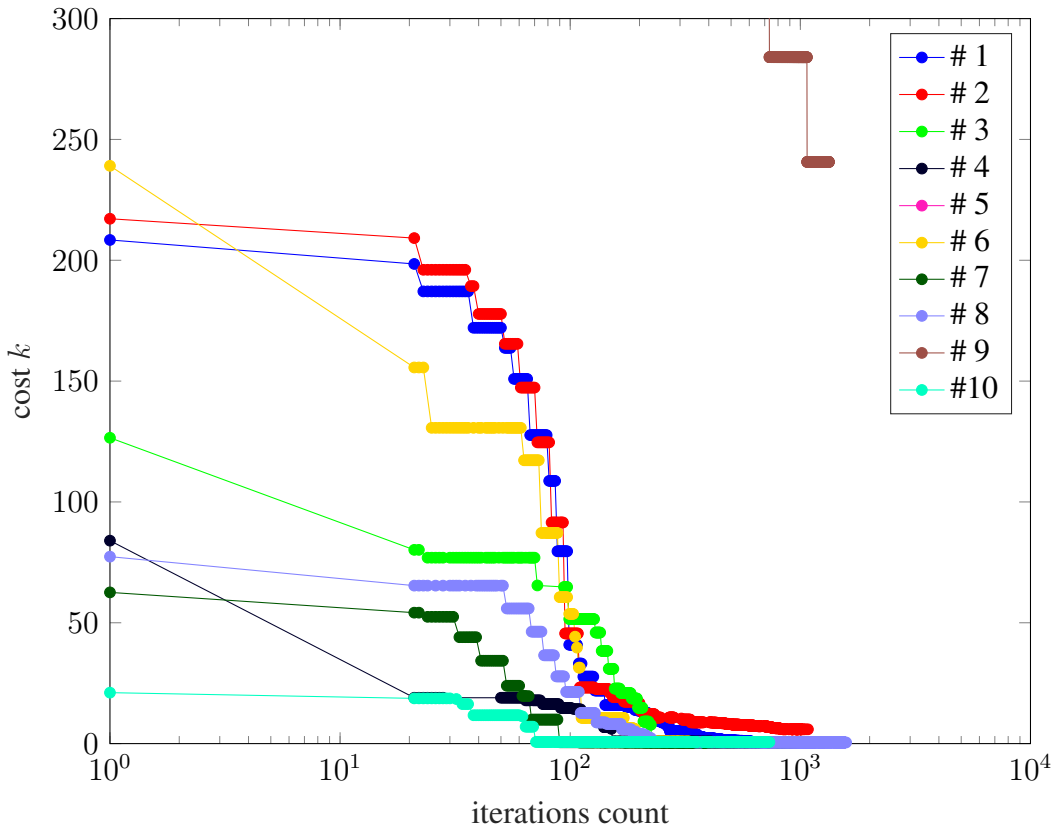

Figure 5.6. Cost versus function calls for a tuning process with relaxed requirements and reduced tolerance. Different runs are denoted with different colors.

5.1.5. Results

The results indicate that run #10 yielded the optimal outcome for meeting strict requirements, whereas run #7 produced the best outcome for meeting relaxed requirements. To illustrate the comparison, Figures 5.7 and 5.8 show the initial trajectory and its PSF for run #10, Figures 5.9 and 5.10 show the final trajectory for run #10 and strict requirements, and Figures 5.11 and 5.12 show the final trajectory for run #10 and relaxed requirements. Analogous results for run #7 are shown in Figures 5.13 and 5.14, 5.15 and 5.16, and 5.17 and 5.18 respectively.

It can be seen that in the case of strict requirements, the obtained parameters were better, but this is at the cost of a much higher number of function calls. This is due to the fact that in the case of strict requirements, the tuning process works on a section of the transfer function

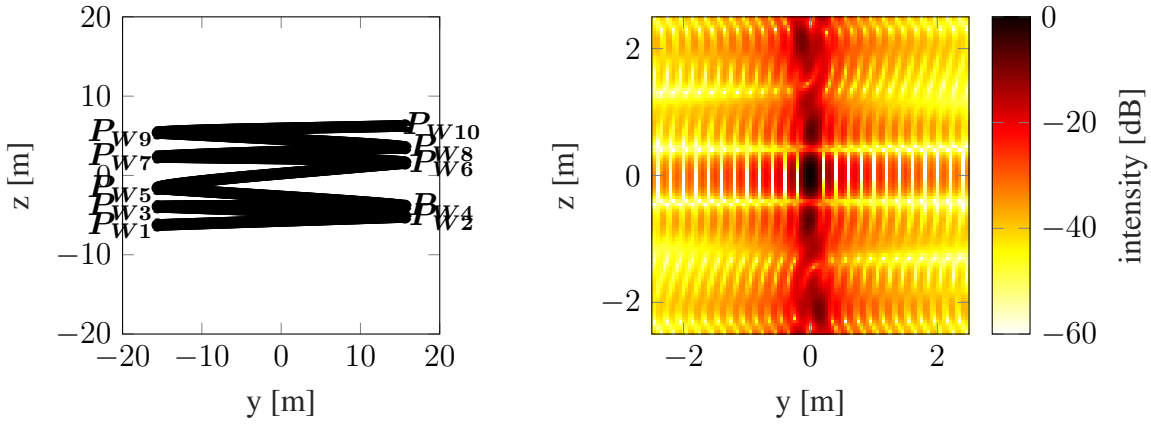

(a) **(b)**

Figure 5.7. Run #10 initial. **(a)** Trajectory, **(b)** 2D cross-range cross-section of 3D PSF.

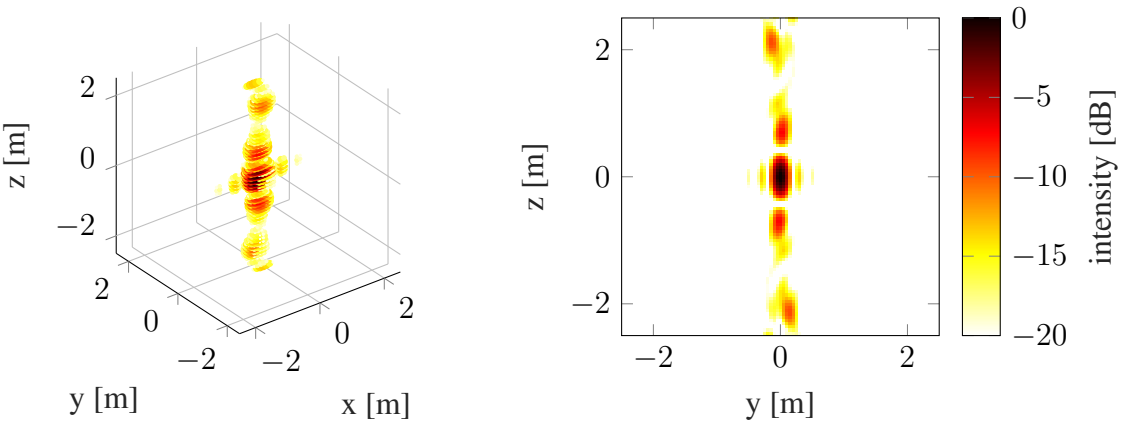

(a) **(b)**

Figure 5.8. Run #10 initial. **(a)** 3D PSF, **(b)** 2D cross-range cross-section of 3D PSF.

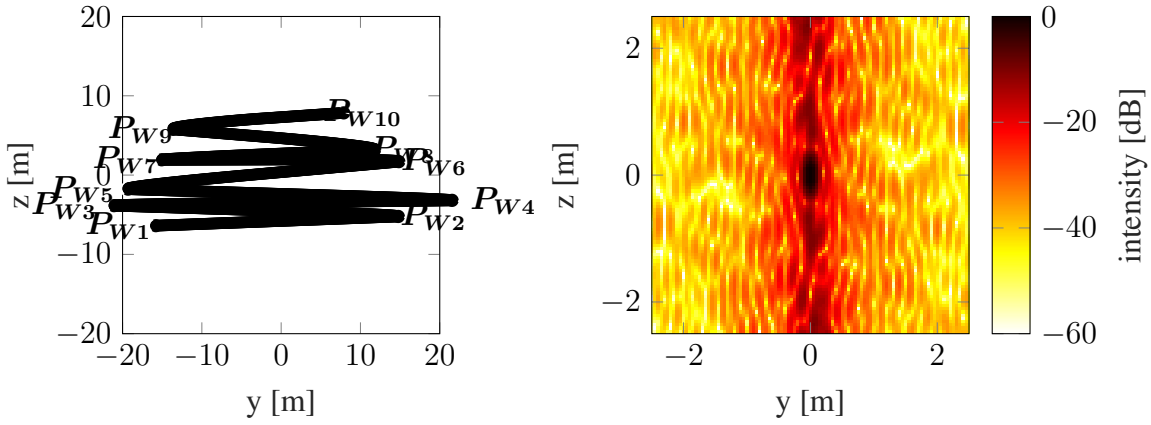

(a) **(b)**

Figure 5.9. Run #10 final for strict requirements. **(a)** Trajectory, **(b)** 2D cross-range cross-section of 3D PSF.

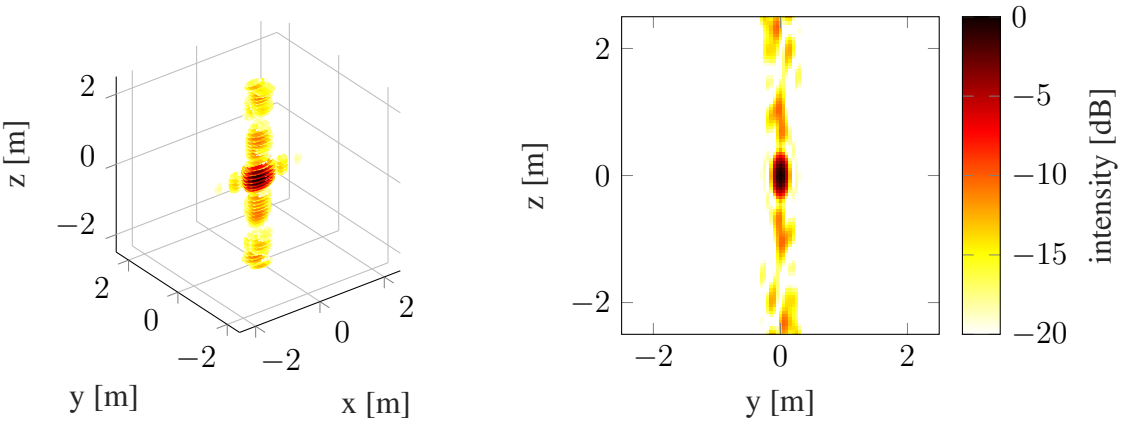

(a) **(b)**

Figure 5.10. Run #10 final for strict requirements. **(a)** 3D PSF, **(b)** 2D cross-range cross-section of 3D PSF.

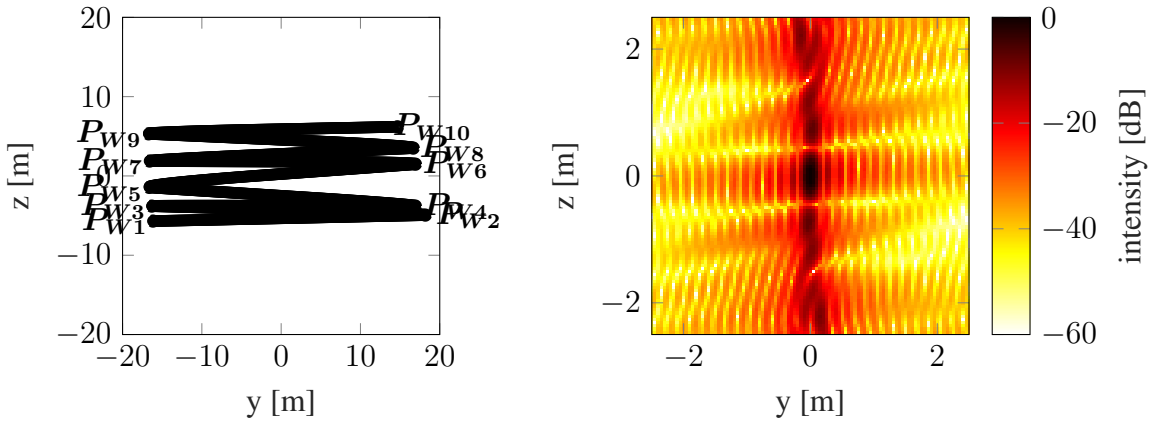

(a) **(b)**

Figure 5.11. Run #10 final for relaxed requirements. **(a)** Trajectory, **(b)** 2D cross-range cross-section of 3D PSF.

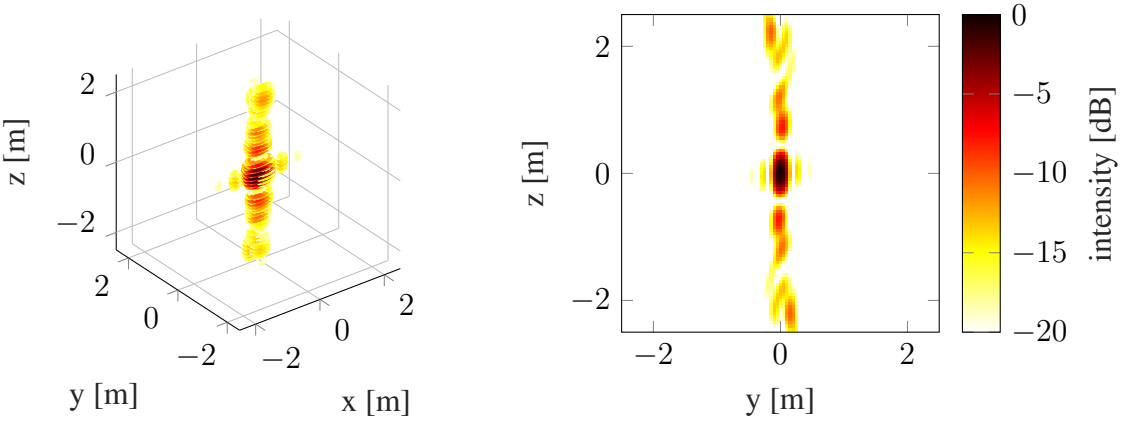

(a) **(b)**

Figure 5.12. Run #10 final for relaxed requirements. **(a)** 3D PSF, **(b)** 2D cross-range cross-section of 3D PSF.

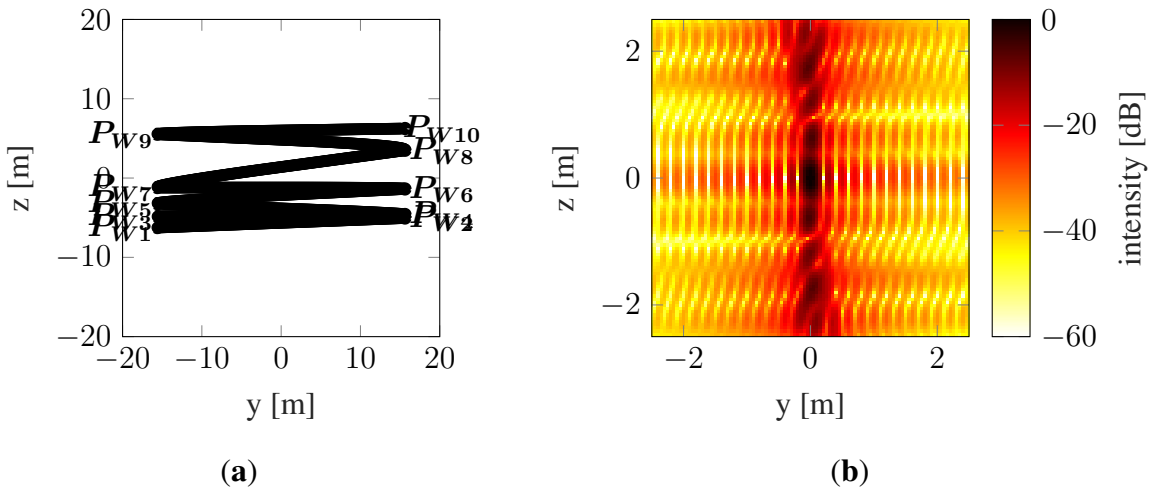

(a) **(b)**

Figure 5.13. Run #7 initial. **(a)** Trajectory, **(b)** 2D cross-range cross-section of 3D PSF.

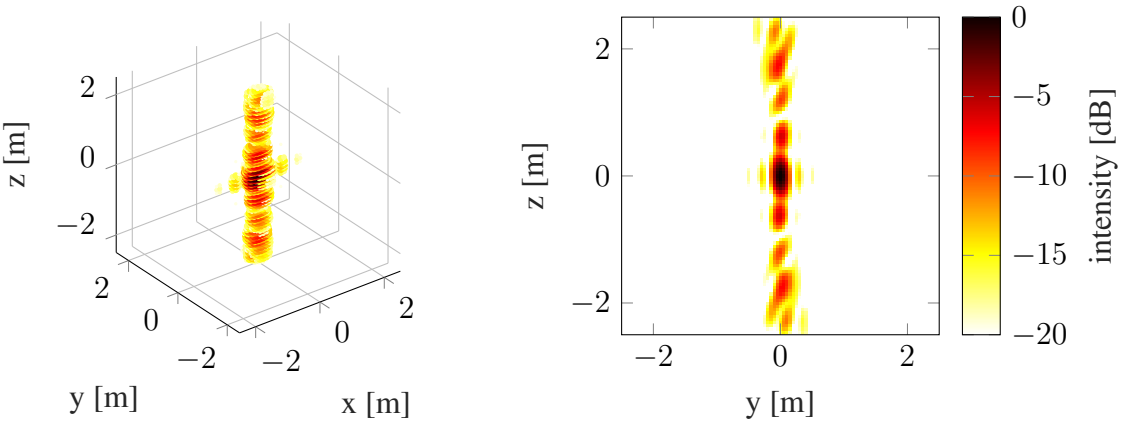

(a) **(b)**

Figure 5.14. Run #7 initial. **(a)** 3D PSF, **(b)** 2D cross-range cross-section of 3D PSF.

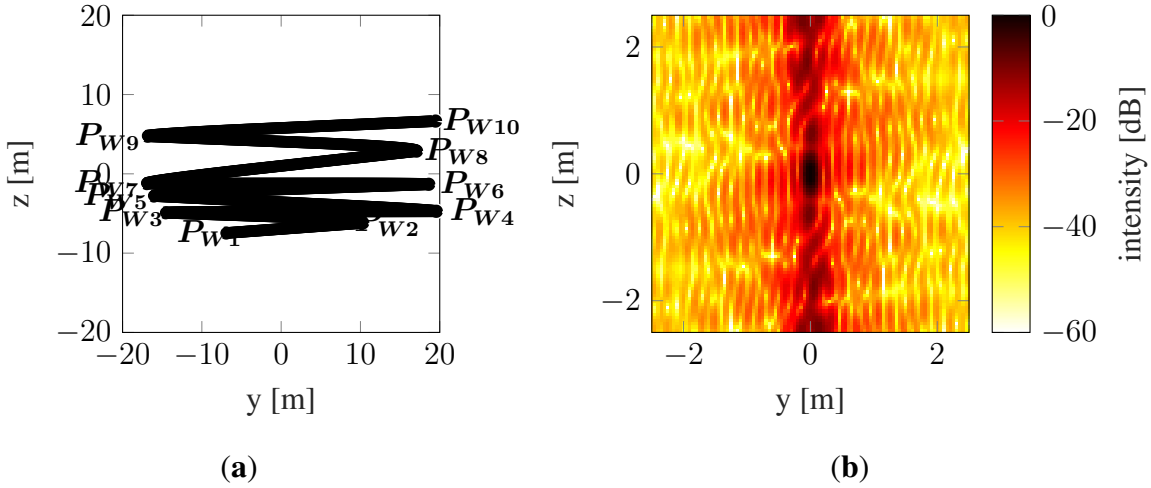

(a) **(b)**

Figure 5.15. Run #7 final for strict requirements. **(a)** Trajectory, **(b)** 2D cross-range cross-section of 3D PSF.

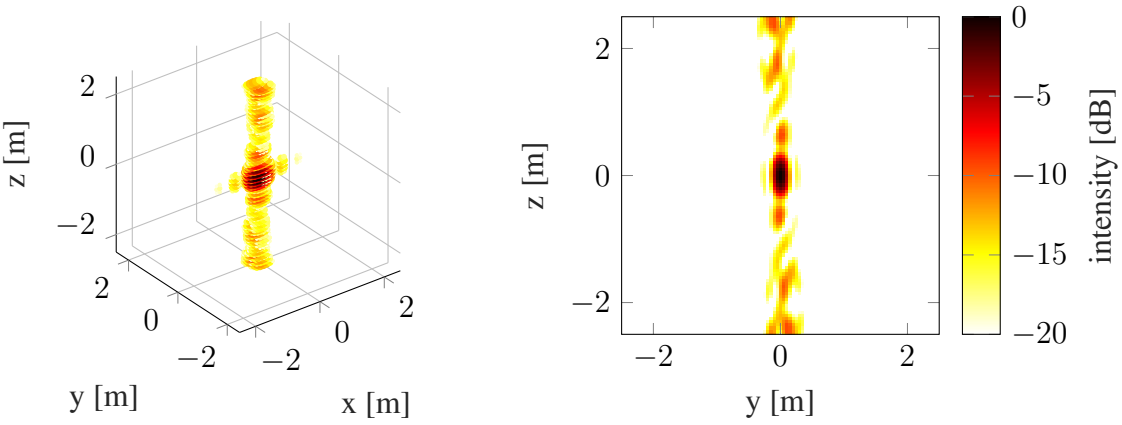

(a) **(b)**

Figure 5.16. Run #7 final for strict requirements. **(a)** 3D PSF, **(b)** 2D cross-range cross-section of 3D PSF.

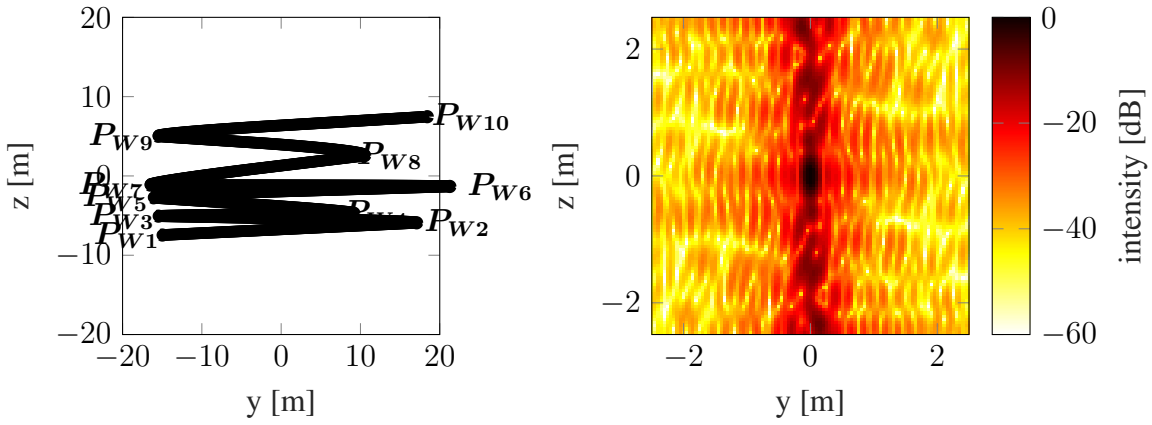

(a) **(b)**

Figure 5.17. Run #7 final for relaxed requirements. **(a)** Trajectory, **(b)** 2D cross-range cross-section of 3D PSF.

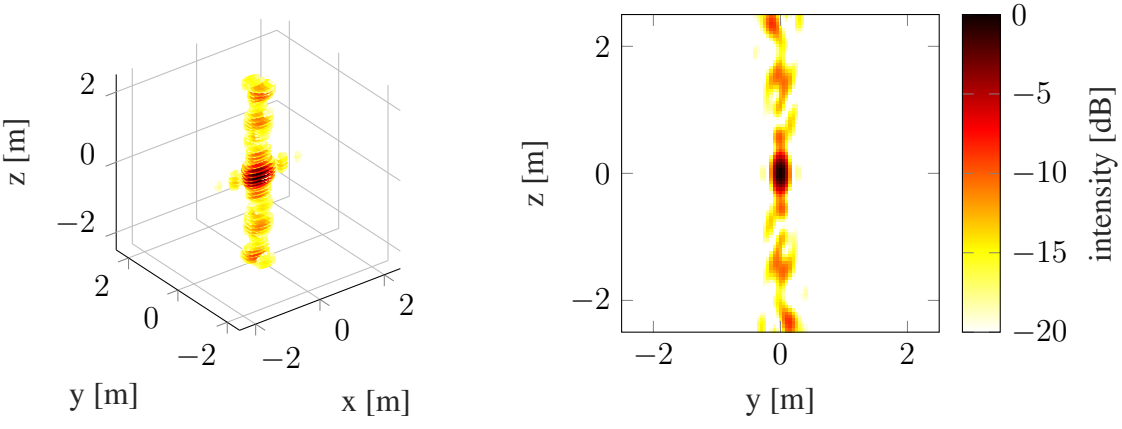

(a) **(b)**

Figure 5.18. Run #7 final for relaxed requirements. **(a)** 3D PSF, **(b)** 2D cross-range cross-section of 3D PSF.

with a slope of 1000, which makes it difficult to meet the conditions for interrupting the tuning process.

It can be noted that the final PSF does not have the periodicity characteristic of the initial and reference PSFs. This is because the periodic PSF is characterized by higher PSLR and ISLR than the non-periodic one, and minimizing these parameters is the goal of the tuning procedure.

To illustrate the performance of the tuning procedure, Figures 5.19, 5.20 and 5.21 show the start and end trajectories for strict and relaxed requirements for runs #5, #7, and #10. Run #5 has the worst start and end parameters for both sets of requirements, run #7 has the best end parameters for relaxed requirements, and run #10 has the best end parameters for strict requirements.

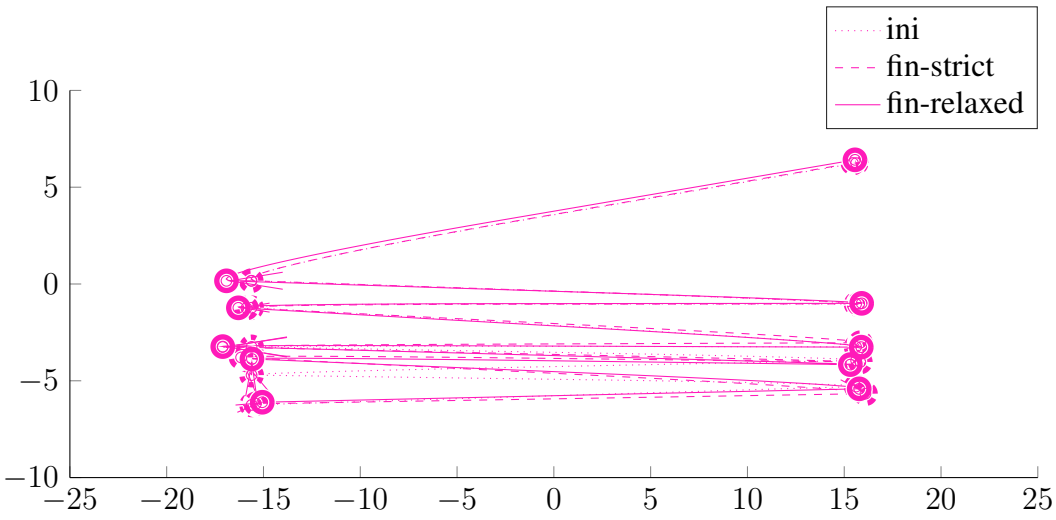

Figure 5.19. Initial trajectory and final trajectories for both requirement sets – run #5.

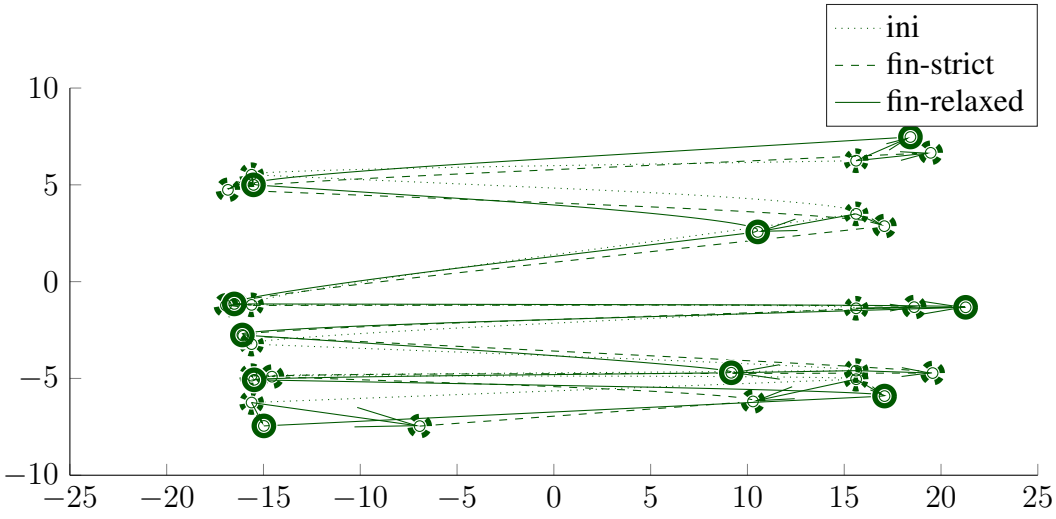

Figure 5.20. Initial trajectory and final trajectories for both requirement sets – run #7.

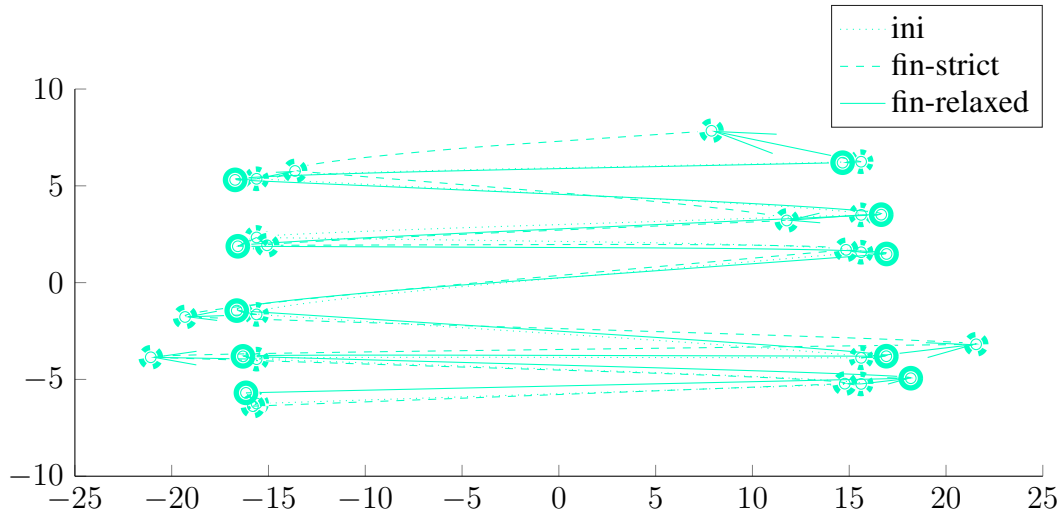

Figure 5.21. Initial trajectory and final trajectories for both requirement sets – run #10.

It can be seen that the tuning of runs #7 and #10 led to a significant change in the trajectory, while for run #5 the final trajectory is not significantly different from the initial one. The initial trajectory and its PSF for run #5 are shown in Figures 5.22 and 5.23, while final trajectory and its PSF for the same run are shown in Figures 5.24 and 5.25.

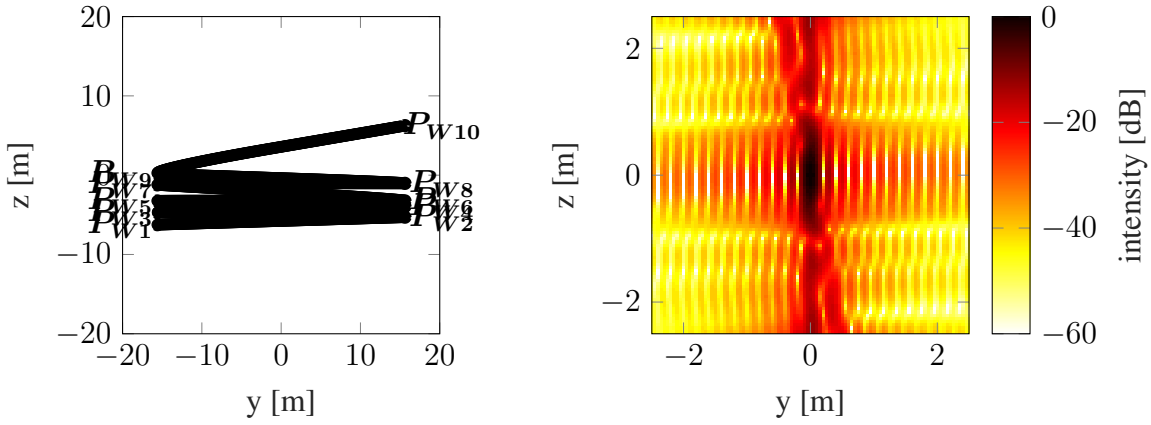

(a) **(b)**

Figure 5.22. Run #5 initial. **(a)** Trajectory, **(b)** 2D cross-range cross-section of 3D PSF.

It can be noted that an important component of the high cost of the trajectory is the vertical resolution, which the tuning algorithm is unable to improve because the starting point is near an unfavourable local minimum. This allows one to make the conclusion that among the selected starting points, those whose cost significantly deviates from the others do not promise well and the tuning process in their case does not need to be carried out.

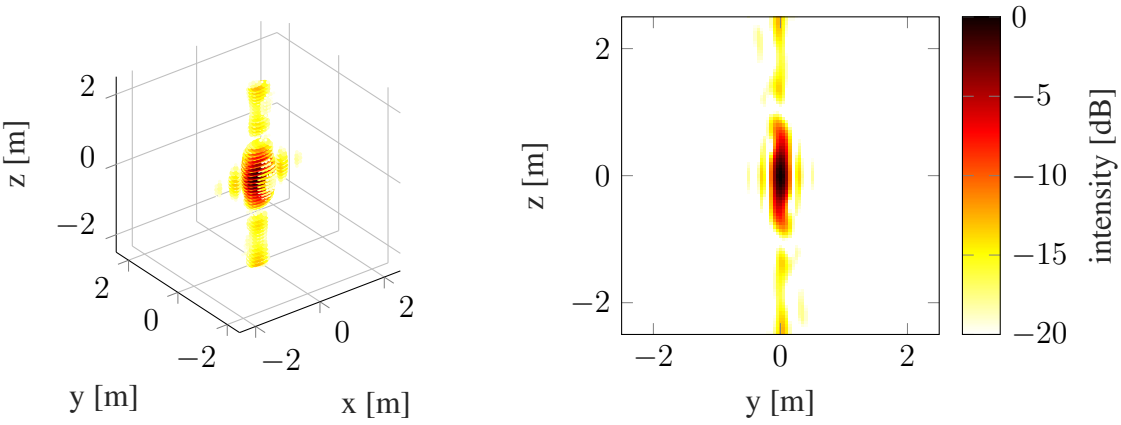

(a) **(b)**

Figure 5.23. Run #5 initial. **(a)** 3D PSF, **(b)** 2D cross-range cross-section of 3D PSF.

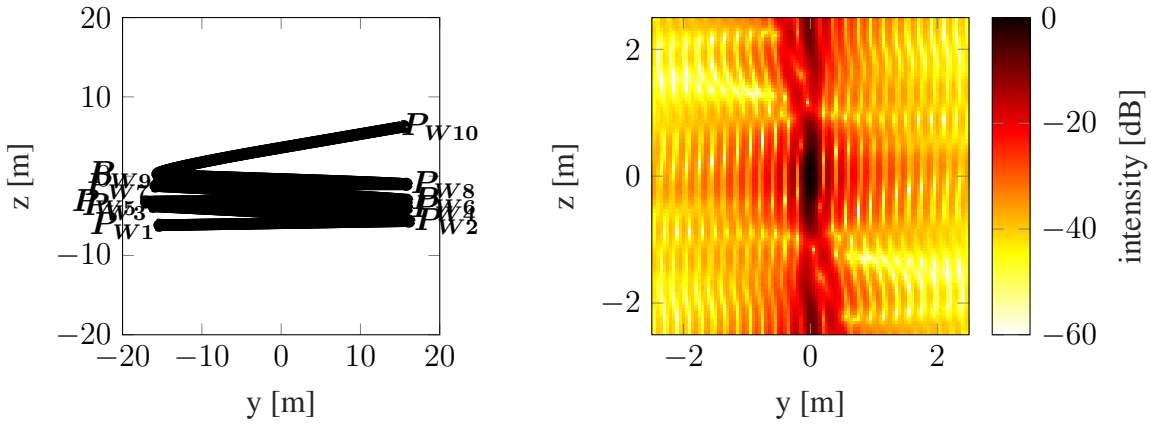

(a) **(b)**

Figure 5.24. Run #5 final for strict requirements. **(a)** Trajectory, **(b)** 2D cross-range cross-section of 3D PSF.

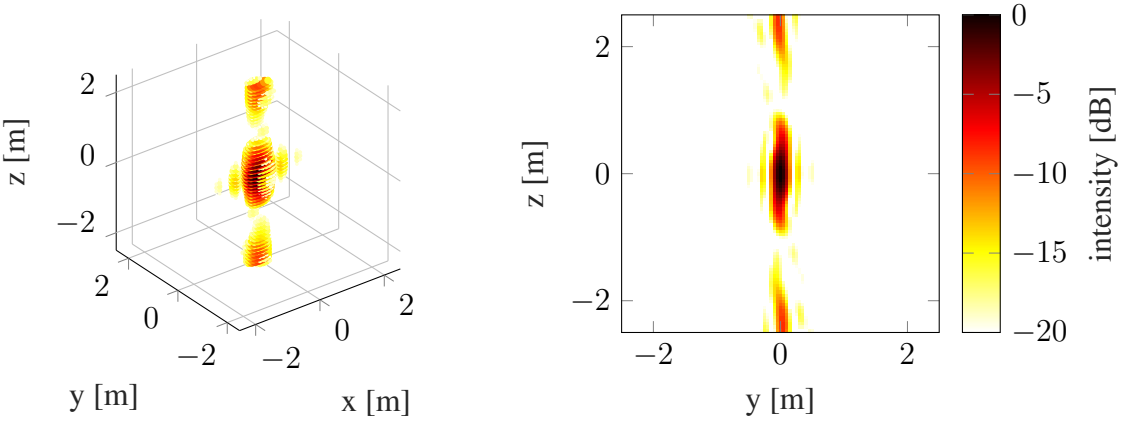

(a) **(b)**

Figure 5.25. Run #5 final for strict requirements. **(a)** 3D PSF, **(b)** 2D cross-range cross-section of 3D PSF.

5.2. Comparison with MBSAR

In order to compare the results achieved by the developed method with the existing 3D SAR imaging method, MBSAR, the PSF is determined over the full imaging range ($10\times10\,\mathrm{m}$) for the best case from the previous section (run #7, see Figure 5.17) and for the reference aperture (see Figure 5.1) with different numbers of runs. PSLR and ISLR are determined for each of these trajectories. The dependence of PSLR and ISLR on the number of passes for MBSAR is shown in Figures 5.26 and 5.27. The same figures indicated the values of the PSF parameters of the

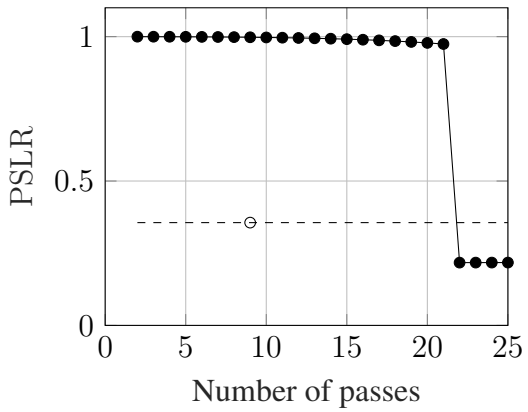

Figure 5.26. MBSAR – PSLR versus number of passes (solid line), simulation run #7 final PSLR value marked with dashed line. Circle indicates that the time reqired for following the trajectory is approximately equal to the time needed to follow a 9-pass MBSAR trajectory.

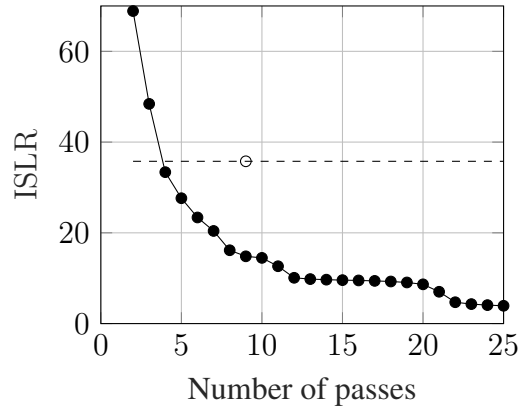

Figure 5.27. MBSAR – ISLR versus number of passes (solid line), simulation run #7 final ISLR value marked with dashed line.

developed method. The characteristic sharp drop in PSLR at 22 passes is observed, indicating that the first grating lobe is outside the imaging area. If, for the sake of comparison, it is assumed that the flight time for the trajectory obtained by the developed method is approximately equal to that of the MBSAR trajectory with 9 passes, it can be seen that the developed method reduced

the time required for the PSLR to fall to an acceptable level by more than two times, while at the same time increasing the ISLR. The 3D PSF of the MBSAR trajectories for 9, 21, and 22 passes, and the 3D PSF of the trajectory of run 7 were shown in Figure 5.28. It is observed that

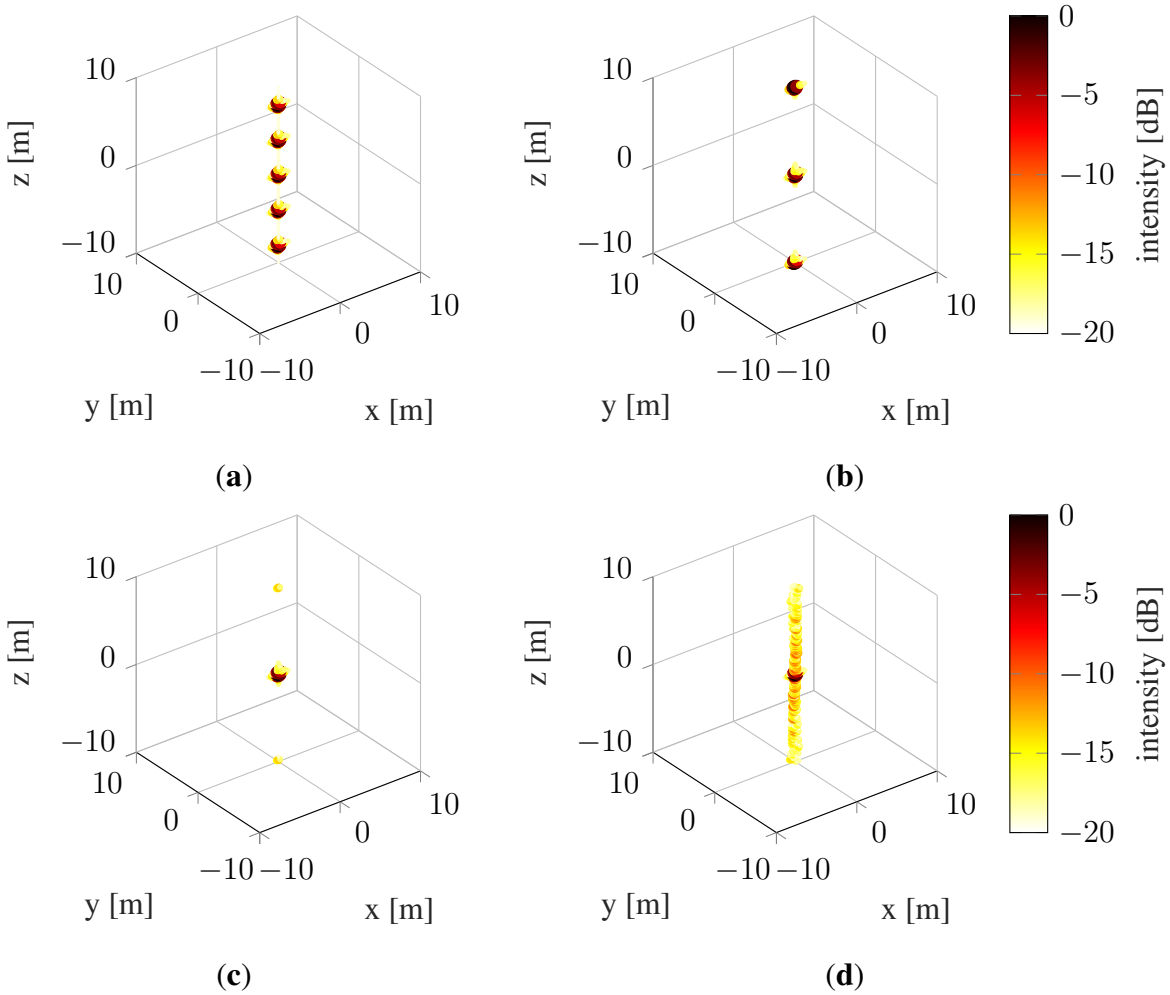

Figure 5.28. 3D PSF in extended region. **(a)** 9-pass MBSAR, **(b)** 21-pass MBSAR, **(c)** 22-pass MBSAR, **(d)** run #7.

as the number of passes increases, the distance between successive grating lobes also increases, and thus the distance from the main lobe to the first grating lobe (see 2.13). The first grating lobe is outside the imaging area if there are at least 22 passes, while in the case of a non-rectilinear trajectory, there are no clear grating lobes and the side lobe is blurred, making the ISLR larger than in the case of MBSAR.

5.3. Experiment

This section describes an experiment conducted with a real-life radar.

5.3.1. Objective

The objective of the experiment is to confirm the applicability of the developed method and to identify and describe potential problems. The experiment did not use an actual UAV equipped with radar, since the author does not have such an apparatus, and constructing it would be a separate complex project requiring several iterations. Instead, a simple radar platform simulator was used and a corresponding scenario was designed. The result of the experiment is the actual results obtained with the radar platform simulator, which are similar in nature to the results that would have been produced with a radar-equipped multirotor.

5.3.2. Scenario

Drawing upon the author's experience in testing radar systems, the experiment was designed to take place on the terrace of the C wing of the building of the Faculty of Electronics and Information Technology of the Warsaw University of Technology, which housed the radar equipment. The target, in turn, was positioned on the parking lot below. A diagram of the experiment location is shown in Figure 5.29, and the simulated geometry is shown in Figure 5.30

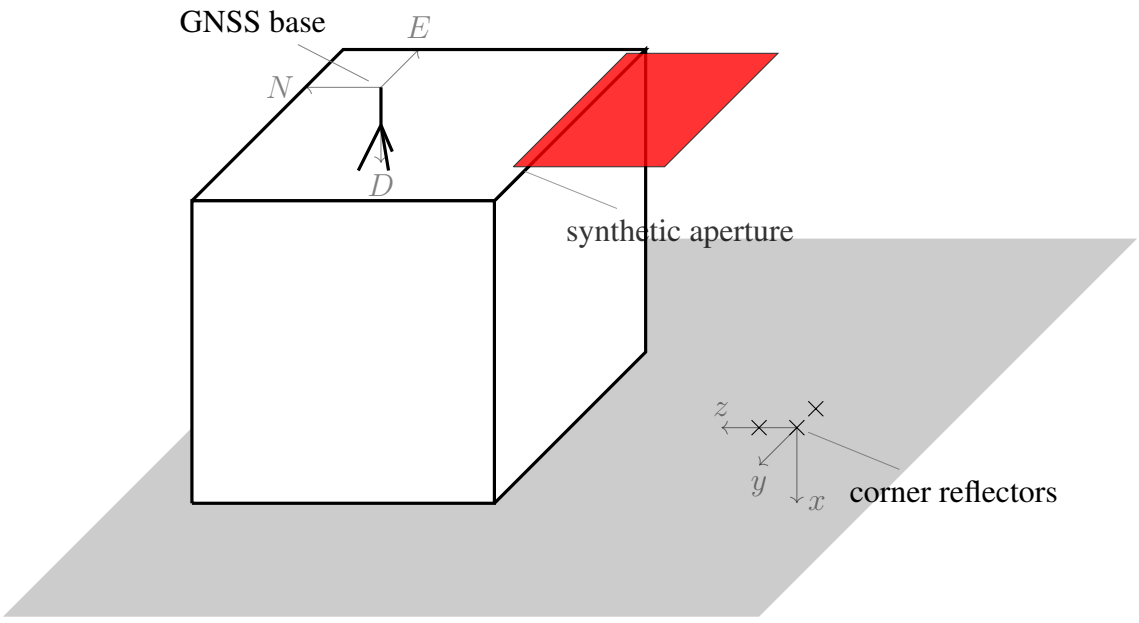

Figure 5.29. Schematic of the experiment geometry.

The movement of the radar platform was simulated using a radar platform simulator moved manually within the synthetic aperture, and the imaged object was created with three corner reflectors placed on the ground. The view from the object to the radar is shown in Figure 5.31 and the view from the radar to the object along with a close-up of the corner reflectors is shown in Figure 5.32. A detailed plan of the experiment with the trajectory generated by the 3dsar-sim simulator [30] is shown in Figure 5.33.

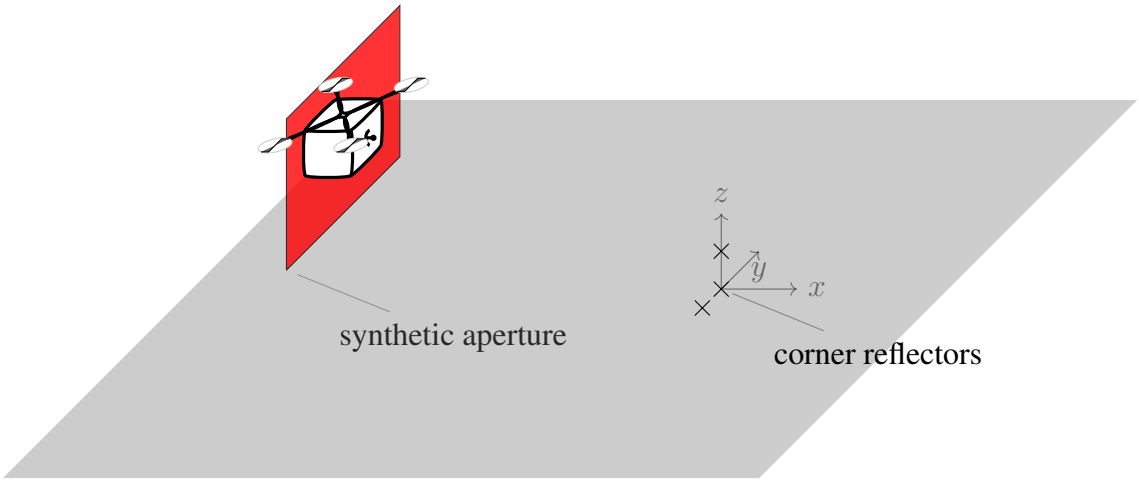

Figure 5.30. The geometry simulated in the experiment.

Figure 5.31. Synthetic aperture from the perspective of the corner reflectors.

5.3.3. Apparatus Overview

5.3.3.1. Radar Platform Simulator

The radar platform hardware simulator is a set of two antennas – a transmitting and a receiving antenna – placed on a long pole, moved by hand. The simulator is shown in Figure 5.34.

In addition to the antennas, Radio Frequency (RF) transmitting and receiving amplifiers, a Global Navigation Satellite System (GNSS) antenna placed as close as possible to the RF antennas, and a control Personal Computer (PC) with a ublox C9-M8P module connected to it were also placed on the pole.

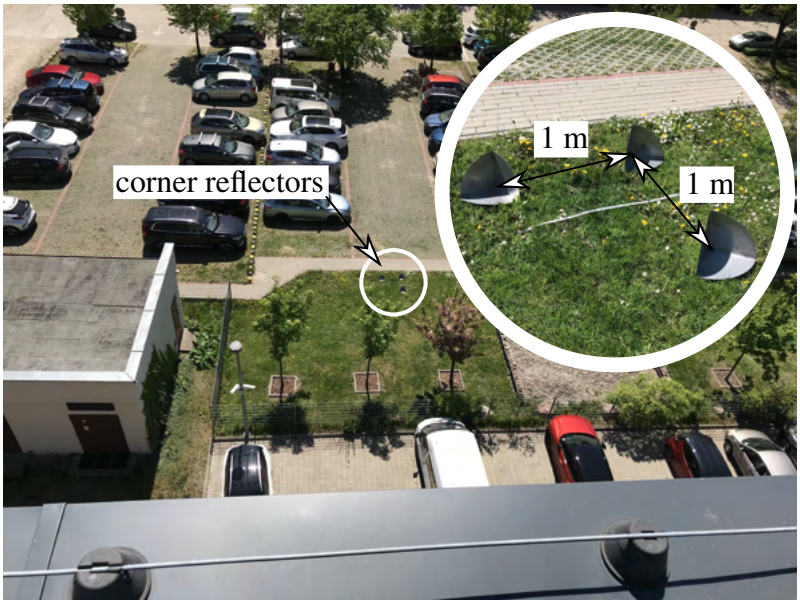

Figure 5.32. Corner reflectors from the perspective of the radar.

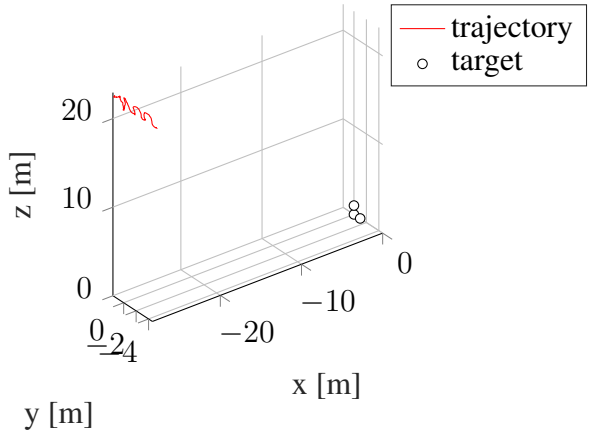

Figure 5.33. Scenario overview generated by the software simulator.

5.3.3.2. Radar System

The versatile C-Band Frequency Modulated Continuous Wave (FMCW) Radar Demonstrator [93], shown in Figure 5.35, was used. This demonstrator is responsible for generating the FMCW signal and recording the echoes. Time synchronization between the radar system and GNSS module was achieved by equipping the demonstrator with a Global Positioning System (GPS) time synchronization module coupled to a GPS Disciplined Oscillator (GPSDO), which provided time stamps recorded along with the echoes.

5.3.3.3. GNSS System

A ublox C9-M8P set consisting of two modules operating in Real-Time Kinematic (RTK) mode – *base* and *rover* – was used for precise determination of the position of the hardware

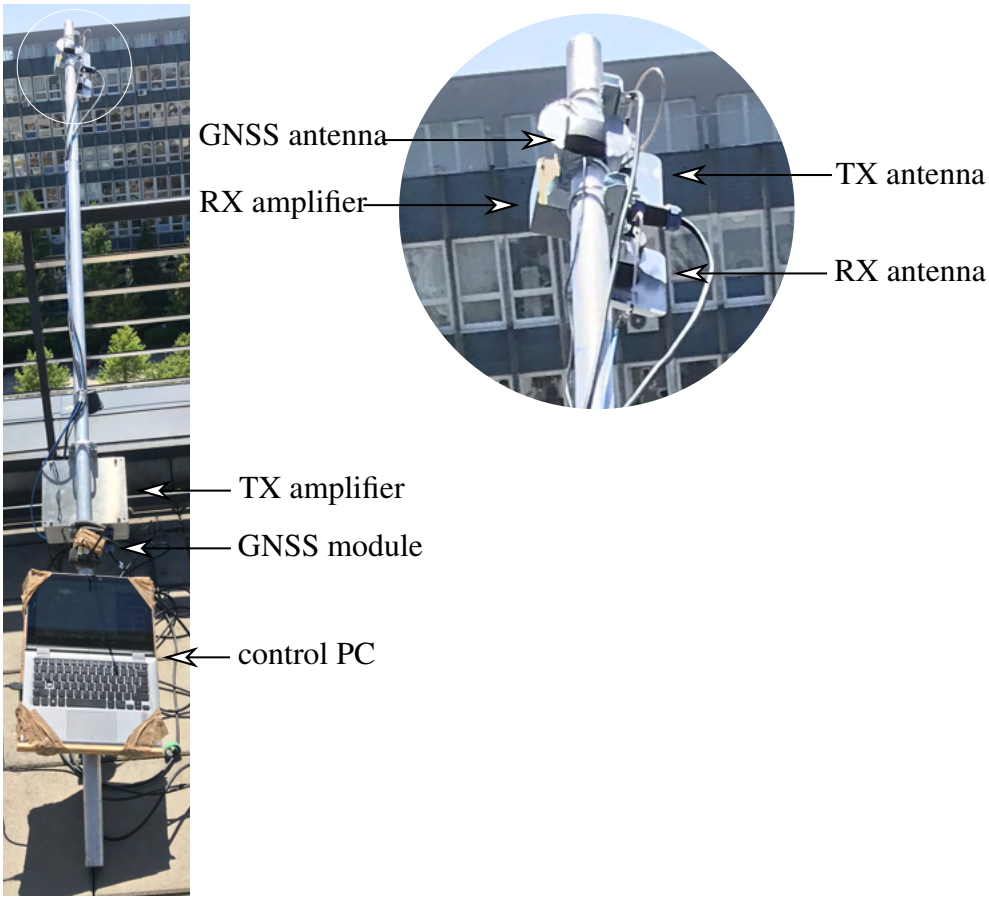

Figure 5.34. Radar platform simulator.

simulator's antennas. The module operating in *base* mode was placed on a high mast on the terrace, near the simulator's radar platform movement area. The *base* placement is shown in Figure 5.36.

The GNSS antenna was placed high to minimize the negative impact of the building's metal structures on GNSS signal reception. The Industrial, Scientific, Medical (ISM) antenna module was placed lower, near the battery.

A module operating in *rover* mode determines its position relative to the base with centimeter accuracy, thanks to corrections received via the ISM connection operating at 2.4 GHz. The *rover*'s position is recorded by the control PC at a frequency of 5 Hz.

5.3.4. The Course of the Experiment

5.3.4.1. Preparation

Preparations began with setting up and powering up the GNSS *base* module. It was ensured that the module was receiving signals from a sufficient number of satellites and was in GPS fix mode. Corner reflectors were then placed at appropriate locations and the GNSS *rover* module was placed on the reference corner reflector and left for the time needed for the module to enter

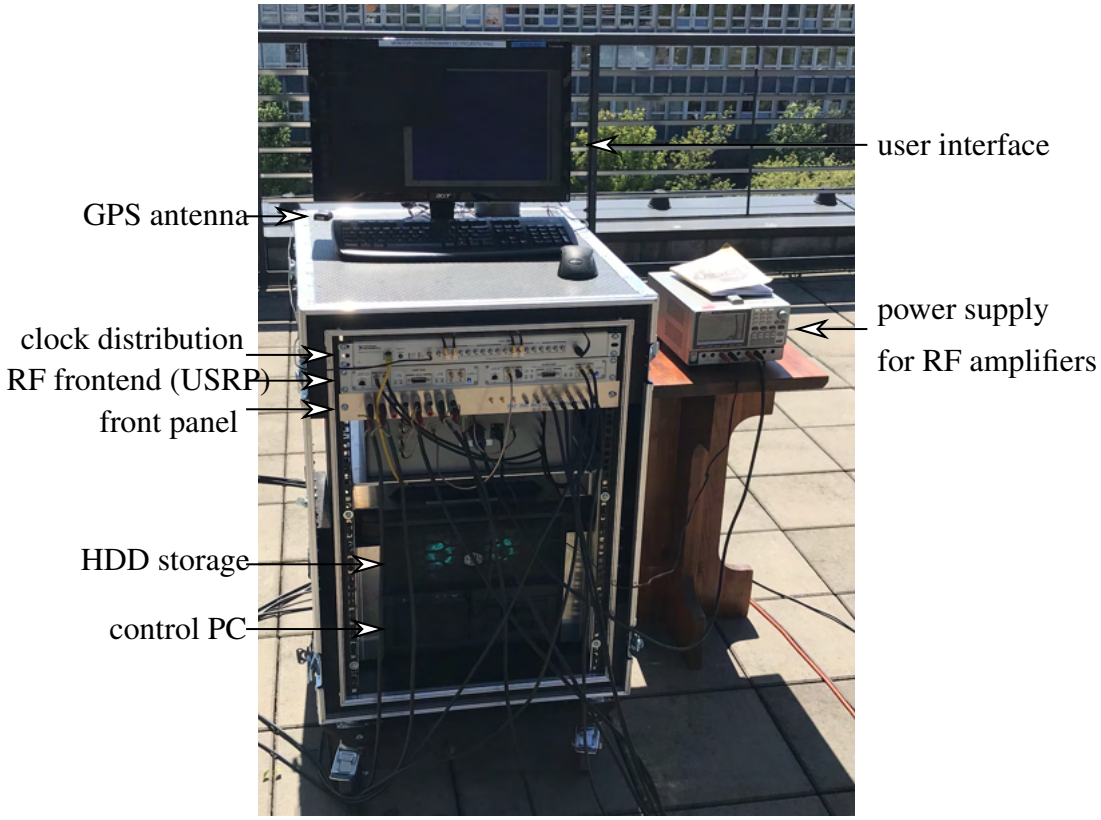

Figure 5.35. Radar system.

GPS fix mode. The position of the module was recorded for more than 50 seconds. The result of this measurement is shown in Figure 5.37. It can be noted that in GPS fix mode, the fluctuation of position does not exceed a few centimeters. The averaged values of measurements in GPS fix mode determine the position of the center of the coordinate system.

The next step was to get the GNSS *rover* module up and running. Despite repeated attempts in different positions and with different antennas, it was not possible to keep the module in GPS fix mode while moving. It was decided to perform the experiment in GPS float mode. The recorded position of the module was observed in the real-time in the Sensor Explorer software, into which a schematic plan of the terrace was loaded.

The final part of the preparation was the start-up of the radar system. The operating parameters were set according to Table 5.3.4.1 and the generated range-Doppler map was observed in real-time. After ensuring that the radar was functioning properly, the actual experiment proceeded.

5.3.4.2. Execution

During the experiment, the operator moved the radar platform simulator in the synthetic aperture area, reproducing a zig-zag pattern. The initial idea was to load the trajectories generated using the developed algorithm into the Sensor Explorer software and move the

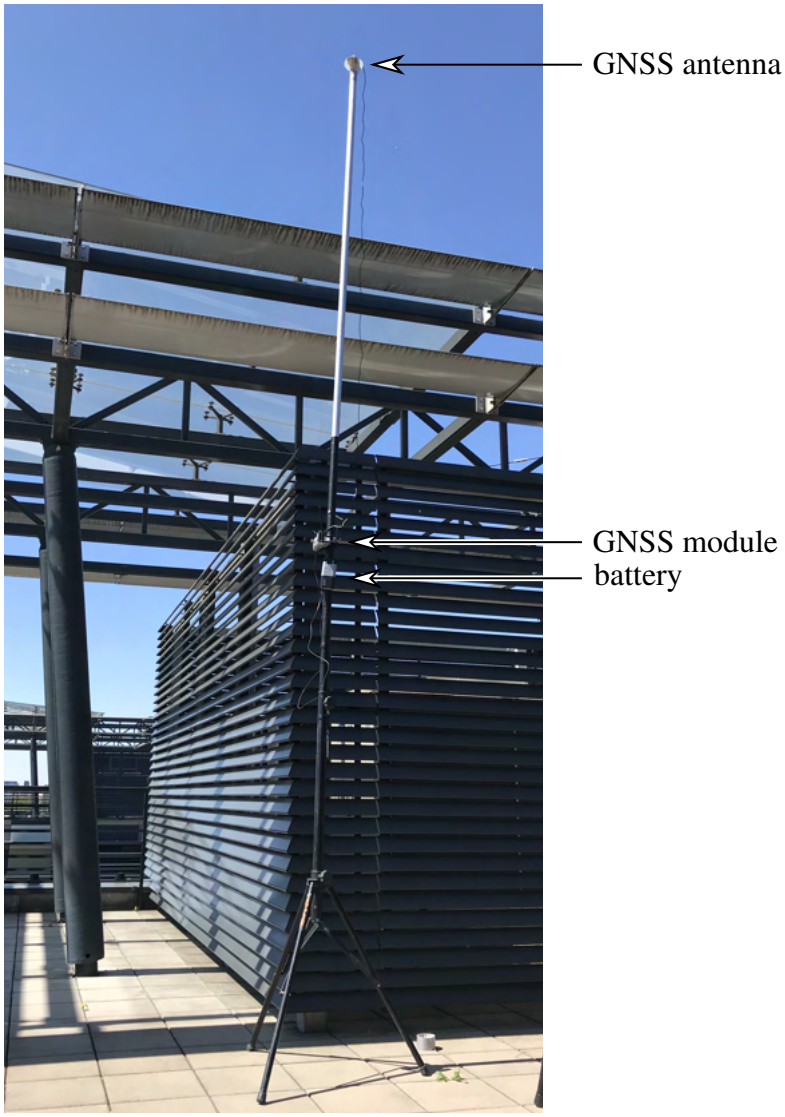

Figure 5.36. GNSS RTK system base.

Parameter	**Symbol**	**Value**
Carrier Frequency	f_c	5.52 GHz
Bandwidth	B	1.344 GHz
Sampling Frequency	f_s	5 MHz

Table 5.7. Radar system parameters.

simulator along them, but due to the large mass (and therefore inertia) of the simulator and the delay in the display of data by the Sensor Explorer software, this proved too difficult and was limited to moving the simulator inside the designated synthetic aperture area. The operator during the execution of the experiment is shown in Figure 5.38. This way, several different waveforms were recorded for later processing.

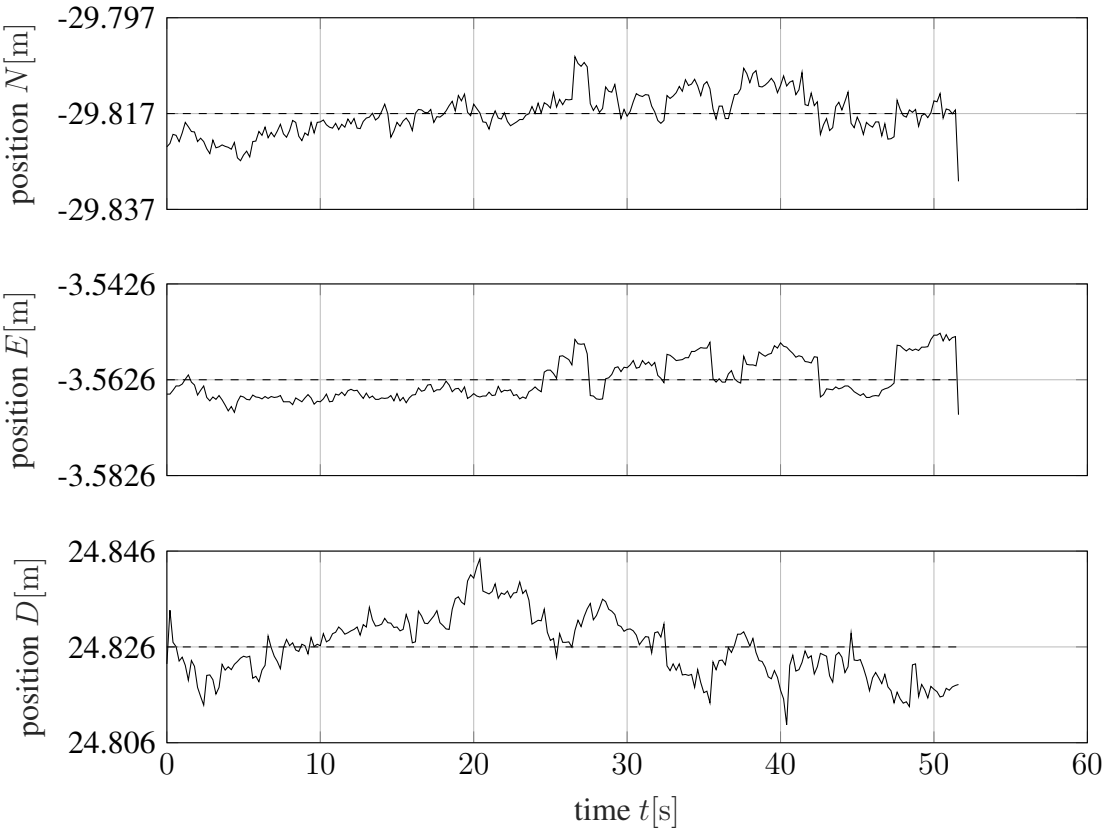

Figure 5.37. Position of the corner reflector with respect to the base – North-East-Down coordinates.

5.3.4.3. Processing

The first step is to synchronize the time stamp of the position recording and the recording of the echoes. The position data contains a time stamp in GPS Time Of Week (TOW) format, i.e., millisecond numbers since the beginning of the week, while the recorded echoes contain a time stamp in Portable Operating System Interface for UNIX (POSIX) TIME 64 format, i.e. nanosecond since the beginning of the Unix era. In view of this, the echoes' time stamp is converted to a format specific to GNSS time, according to the formula:

$$t_{\text{echo}}[\text{ms}] = \frac{\text{timestamp64}}{10^6} - 10^3 t_{\text{POSIX}}(\text{SOW}), \tag{5.5}$$

where timestamp64 is the input timestamp of the data, and $t_{\text{POSIX}}(\text{SOW})$ is the number of seconds from the beginning of the Unix era to the beginning of the week.

The next step is to select for each position measurement point the echo closest to it in time. Since the radar operates at a PRF of $2\,\text{kHz}$ and position recording is done at $5\,\text{kHz}$, approximately every 400th echo is selected. Assuming that the platform simulator is moving at a speed of no more than $0.5\,\text{m/s}$, it can be determined that the maximum error in position determination due to the lack of accurate synchronization is:

$$\delta_{rMAX} = 0.5 \times 2\,\text{kHz} \times 0.5\,\text{m/s} = 0.5\,\text{mm}, \tag{5.6}$$

Figure 5.38. Operator during the experiment, carefully controlling module position and GNSS status.

that is an order of magnitude less than the advertised accuracy of the GNSS module's position determination and two orders of magnitude less than the radar carrier wavelength.

5.3.5. Results

A range-time map of the selected portion of the registration is shown in Figure 5.39. For comparison, Figure 5.40 shows the simulation results from the 3dsar-sim simulator for equal radar parameters and equal trajectory. It can be observed that the main lobe is not visible in the recorded signal due to the imperfection of the radar frontend and the requirement to filter out strong stationary interference. However, its higher harmonics are distinctly visible, unlike in the simulated signal. Therefore, it can be inferred that a signal recorded using an alternative frontend would closely match the simulated signal.

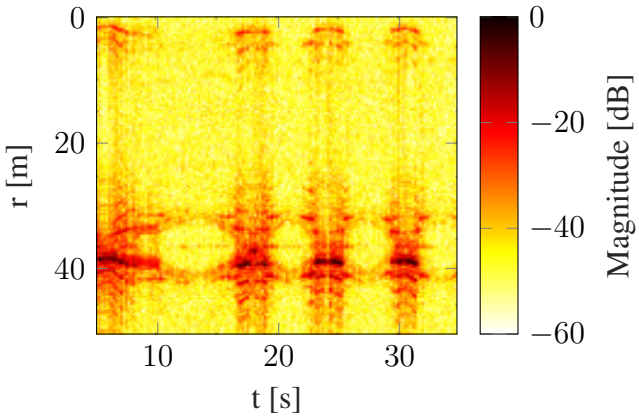

Figure 5.39. Range-time map of the experiment – recorded.

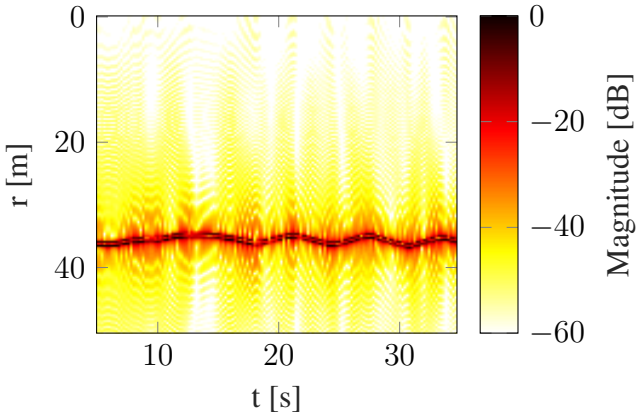

Figure 5.40. Range-time map of the experiment – simulated.

The trajectory and its PSF are shown in Figure 5.41, while the 3D imaging generated from the simulated data is shown in Figure 5.42. It should be noted that, despite having a very strong side lobe, the PSF still allows for clear visualization of the main lobe. Both the 3D imaging and its cross-section reveal that the height of the side lobes is below -10 dB, while the scatterers remain distinctly visible. It is worth emphasizing once again that the trajectory used is not a result of the described method but rather aims to demonstrate the feasibility of achieving 3D imaging through a non-rectilinear trajectory.

5.4. Discussion

The results of the simulation experiments show that trajectory tuning is indeed an essential component of the developed method. The initial trajectory did not provide the expected requirements in any case, which means that random trajectory selection is not a sufficient approach. Observing the comparison of the initial trajectory and the final variants, it can be seen that the changes are not great, which indicates that the cost is strongly non-convex as a

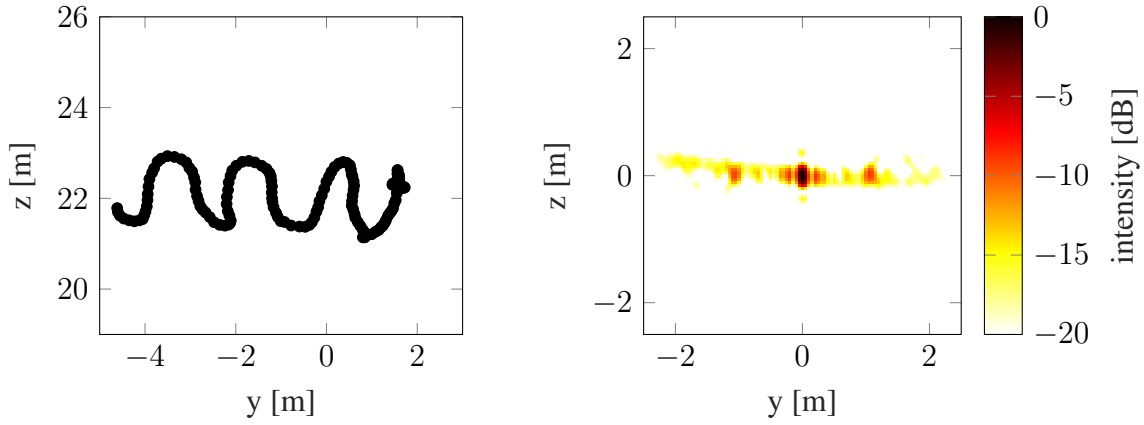

(a) **(b)**

Figure 5.41. Experiment. **(a)** Trajectory, **(b)** 2D cross-range cross-section of 3D PSF.

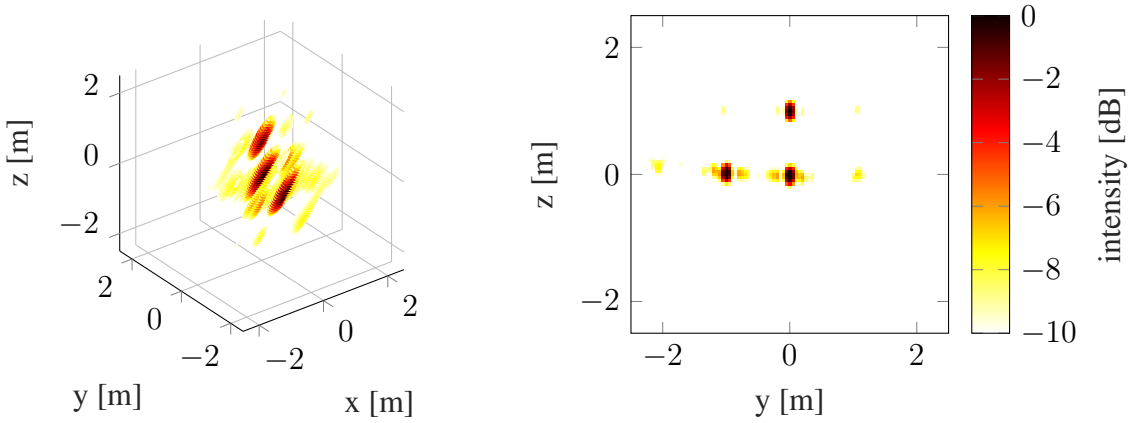

(a) **(b)**

Figure 5.42. Simulated experiment result. **(a)** 3D view, **(b)** Cross-section.

function of the placement of waypoints. In addition, the different direction of tuning depending on the adopted requirements indicates the significant influence of the requirements on the shape of the cost function.

Analyzing the tabular comparison of the cost before and after tuning for all trajectories, it can be seen that the main effect of tuning is to lower the PSLR while maintaining the other requirements. Such a view allows one to interpret the essence of the developed method in a different way – replacing the traditional trajectory with a shorter zig -zag-shaped one, which, as it sparsely fills the surface of the synthetic aperture, is characterized by a high PSLR, and in the next step (tuning) reducing the PSLR by appropriate modification of the trajectory.

The purpose of the experiment using the hardware simulator is not to demonstrate the performance of the algorithm. First of all, it shows that obtaining an imaging using a non-straight trajectory is possible. In addition, the experiment has highlighted the essential issue of the accuracy of determining the position of the radar platform – when very high accuracy is

required, it is necessary to use the Inertial Measurement Unit (IMU) and the Kalman filter in addition, and to make sure that all additional sources of inaccuracy have been eliminated (such as movements of the base antenna due to wind gusts).

6. Summary

The dissertation presents a method for obtaining 3D SAR imaging using a single channel radar sensor and radar platform trajectory tuning. The advantage of the presented method over existing 3D SAR imaging methods, i.e., MBSAR, is the significant reduction of the platform flight time. The method combines the topics of SAR imaging with a motion model of unmanned, autonomous and semi-autonomous flying platforms (the example of such a platform used in this work is a multi-rotor aircraft).

6.1. Conclusions

The dissertation has two theses. The initial one is as follows:

> It is possible to obtain three-dimensional radar imaging of a region of interest using a single single-channel radar and a non-rectilinear trajectory of the radar platform.

This thesis is confirmed by the analysis of the state of the art and the experiments. The second thesis of the dissertation states:

> It is possible to tune the trajectory of the radar platform to improve imaging quality or reduce sounding time, if the radar parameters, radar platform motion model, dimensions of the area of interest, and required imaging quality parameters are known.

It is confirmed by the analysis of simulation experiments, that shows that the presented trajectory tuning algorithm can improve the quality of the acquired imaging and reduce the flight time of the radar platform.

The key contributions of the dissertation are:

— A novel method of obtaining 3D SAR imaging with a single-channel radar sensor, using non-rectilinear radar platform trajectory.
— An original algorithm of radar platform trajectory tuning to improve imaging quality and reduce flight time.
— The use of a real-life jerk limited motion model of the radar platform (multi-rotor).
— Inclusion of three measurable image quality parameters – resolution, PSLR, and ISLR.
— An algorithm of determining the equivalent resolution for non-rectangular main lobe.

— Experiments with software simulation and a real radar system.

The dissertation presents an overview of existing approaches to 3D SAR imaging, with a particular focus on those that use non-rectilinear trajectories, such as sine SAR and HAT. Shortcomings of these approaches are identified, including the lack of an actual motion model of the platform and a focus solely on the resolution of the resulting imaging, without considering ISLR and PSLR, which are critical for non-rectilinear trajectories.

To address these shortcomings, the proposed method directly applies the jerk-limited motion model, commonly used not only in multi-rotorcraft but also in autonomous fixed-wing. This method considers not only resolution but also PSLR and ISLR as imaging quality criteria. Based on these quality criteria, a trajectory tuning algorithm is developed to further enhance imaging parameters.

The essence of the dissertation, the proposed method, is tested in a series of simulations. The results are compared with those of the well-established MBSAR technique, and the impact of the set requirements on the results is investigated. The results demonstrate that the proposed method makes it possible to reduce the platform's flight time while maintaining the required resolution and with increased PSLR and ISLR.

The dissertation concludes with a description of an experiment that used a hardware simulator built on a real radar. The experiment confirms the applicability of the developed method and lays the foundation for further work towards an experiment using an actual flying platform. The experiment also highlights significant problems related to the accuracy of determining the platform's position using GNSS RTK, such as the need to ensure undistorted satellite reception and the rigidity of the base station mast. Furthermore, it is emphasized that even an accuracy of position determination of approximately $1\,\mathrm{cm}$ is insufficient for higher-band radars, necessitating the use of methods to improve this accuracy, such as IMU-supported Kalman filters and autofocusing.

6.2. Future Work Roadmap

The natural next step is to perform validation using the actual radar platform, which requires solving existing problems with the accuracy of determining the position of the radar platform. The author hopes that the work presented in this dissertation is the first step to creating a fully cognitive 3D imaging radar system, consisting of multiple drone borne passive and active radars that can create a 3D image in the real-time and adjust or modify their trajectories and operation modes in response to situation changes and the information obtained from the imaging.

In order to achieve this goal, it is necessary to work in two directions – first, the algorithms used in the tuning process should be optimized to allow them to work in real-time. Preliminary considerations on optimization of PSF determination were presented by the author in the paper

[28]. Second, it is necessary to generalize the developed algorithm so that it can be applied to multistatic systems. The path to this goal is determined by the following steps of radar system evolution:

— Bistatic system, with one moving receiver and a single stationary transmitter.
— Multistatic system, with one moving receiver and multiple stationary transmitters.
— Bistatic system, with one moving receiver and one moving transmitter.
— Multistatic system, with multiple moving or stationary transmitters and receivers, with the assumption that the routes of some transmitters and receivers cannot be changed.
— A system as above, with the assumption that targets can be changed during the measurement, and transmitters and receivers can disappear and reappear at any time, regardless of the algorithm.

Each of the above steps involves an increasing generalization of the developed method and is in itself a formidable research challenge, beyond the capabilities of a single researcher or perhaps even a research team. The author hopes that this dissertation and the published articles on this topic will be used by researchers conducting related research and contribute to the development of the scientific field and find application in industry and defense.

Bibliography

[1] V. L. Mulder, S. de Bruin, M. E. Schaepman, and T. R. Mayr. The use of remote sensing in soil and terrain mapping - A review, 2011.

[2] D. Brunner, G. Lemoine, and L. Bruzzone. Earthquake damage assessment of buildings using VHR optical and SAR imagery. *IEEE Transactions on Geoscience and Remote Sensing*, 48(5):2403–2420, 2010.

[3] P. Gamba, B. Houshmand, and M. Saccani. Detection and extraction of buildings from interferometric SAR data. *IEEE Transactions on Geoscience and Remote Sensing*, 38(1 II):611–618, 2000.

[4] M. Reggiannini and L. Bedini. Multi-sensor satellite data processing for marine traffic understanding. *Electronics (Switzerland)*, 8(2), 2019.

[5] M. Caris, S. Stanko, M. Malanowski, P. Samczynski, K. Kulpa, A. Leuther, and A. Tessmann. Mm-Wave SAR demonstrator as a test bed for advanced solutions in microwave imaging. *IEEE Aerospace and Electronic Systems Magazine*, 29(7):8–15, 2014.

[6] M. I. Skolnik. *Radar Handbook, Third Edition*. Electronics electrical engineering. McGraw-Hill Education, 2008.

[7] C. M. Neale and B. G. Crowther. An airborne multispectral video/radiometer remote sensing system: Development and calibration. *Remote Sensing of Environment*, 49(3):187–194, 1994.

[8] C. Mallet and F. Bretar. Full-waveform topographic lidar: State-of-the-art, 2009.

[9] C. Boryan, Z. Yang, and B. Haack. Evaluation of Sentinel-1A C-band Synthetic Aperture Radar for citrus crop classification in Florida, United States. In *International Geoscience and Remote Sensing Symposium (IGARSS)*, volume 2018-July, pages 7369–7372, 2018.

[10] R. Congalton. Remote sensing: An overview. *GIScience and Remote Sensing*, 47(4):443–459, 2010.

[11] D. C. Munson, J. D. O'brien, and W. Kenneth Jenkins. A Tomographic Formulation of Spotlight-Mode Synthetic Aperture Radar. *Proceedings of the IEEE*, 71(8):917–925, aug 1983.

[12] A. Reigber and A. Moreira. First demonstration of airborne SAR tomography using multibaseline L-band data. *IEEE Transactions on Geoscience and Remote Sensing*, 38(5 I):2142–2152, 2000.

[13] J. Drozdowicz, P. Samczynski, M. Wielgo, D. Gromek, and K. Klincewicz. The use of FPGA evaluation board as data acquisition and pre-processing system for Synthetic Aperture Radar. In *Proceedings International Radar Symposium*, volume 2015-Augus, pages 535–540, 2015.

[14] P. Samczynski, D. Gromek, J. Drozdowicz, M. Wielgo, K. Klincewicz, M. Malanowski, K. Kulpa, M. Nowakowski, J. Krzonkalla, M. Mordzonek, and M. Bryl. Experimental results of DANIEL-35

SAR system tests. In *Proceedings International Radar Symposium*, volume 2015-Augus, pages 571–576, 2015.

[15] P. Samczynski, D. Gromek, J. Drozdowicz, M. Wielgo, K. Klincewicz, A. Grabowski, M. Baczyk, and K. Kulpa. Recent results of high resolution ground image formation using miniaturized C-Band synthetic aperture radar. In *Proceedings of the European Conference on Synthetic Aperture Radar, EUSAR*, 2016.

[16] A. Moses, M. J. Rutherford, M. Kontitsis, and K. P. Valavanis. UAV-borne X-band radar for collision avoidance. *Robotica*, 32(1):97–114, 2014.

[17] G. Peterson. Miniature K-Band Radar for Agricultural Remote Sensing. In *2021 IEEE 21st Annual Wireless and Microwave Technology Conference, WAMICON 2021*, 2021.

[18] Y. Zhang, Q. Yang, B. Deng, Y. Qin, and H. Wang. Experimental research on interferometric inverse synthetic aperture radar imaging with multi- channel terahertz radar system. *Sensors (Switzerland)*, 19(10), 2019.

[19] D. Gromek, K. Radecki, J. Drozdowicz, P. Samczyński, and J. Szabatin. Passive SAR imaging using DVB-T illumination for airborne applications. *IET Radar, Sonar and Navigation*, 13(2):213–221, 2019.

[20] J. Drozdowicz, P. Samczynski, and M. K. Baczyk. Three-dimensional imaging of a rotating airborne target using bistatic inverse synthetic aperture radar. In *2017 Signal Processing Symposium, SPSympo 2017*, 2017.

[21] J. Drozdowicz, M. Wielgo, and M. K. Baczyk. Generalized SL0 algorithm for 3D circular SAR imaging. In *MIKON 2018 - 22nd International Microwave and Radar Conference*, pages 265–266, 2018.

[22] M. Martorella(editor). Pre-Released STO Technical Report Multi-Dimensional Radar Imaging (NATO Unclassified). Technical report, NATO Science and Technology Organization, 2021.

[23] Y. Huang, Q. Zhang, and L. Ferro-Famil. Forest height estimation using a single-pass airborne l-band polarimetric and interferometric sar system and tomographic techniques. *Remote Sensing*, 13(3):1–20, 2021.

[24] L. Zhao, E. Chen, Z. Li, W. Zhang, and Y. Fan. A New Approach for Forest Height Inversion Using X-Band Single-Pass InSAR Coherence Data. *IEEE Transactions on Geoscience and Remote Sensing*, 60, 2022.

[25] G. Corsini, M. Diani, F. Lombardini, and G. Pinelli. Simulated analysis and optimization of a three-antenna airborne InSAR system for topographic mapping. *IEEE Transactions on Geoscience and Remote Sensing*, 37(5 II):2518–2529, 1999.

[26] J. I. Askne, P. B. Dämmert, L. M. Ulander, and G. Smith. C-band repeat-pass interferometric sar observations of the forest. *IEEE Transactions on Geoscience and Remote Sensing*, 35(1):25–35, 1997.

[27] K. Zalite, O. Antropov, J. Praks, K. Voormansik, and M. Noorma. Monitoring of Agricultural Grasslands with Time Series of X-Band Repeat-Pass Interferometric SAR. *IEEE Journal of Selected Topics in Applied Earth Observations and Remote Sensing*, 9(8):3687–3697, 2016.

[28] J. Drozdowicz. Point spread function estimation for airborne three-dimensional synthetic aperture radar. In *Proceedings International Radar Symposium*, volume 2020-Octob, pages 264–269, 2020.

[29] J. Drozdowicz and P. Samczynski. Drone-Based 3D Synthetic Aperture Radar Imaging with Trajectory Optimization. *Sensors*, 22(18):6990, sep 2022.

[30] J. Drozdowicz. The Open-Source Framework for 3D Synthetic Aperture Radar Simulation. *IEEE Access*, 9:39518–39529, 2021.

[31] ISO. Quantities and units - Part 2: Mathematical signs and symbols to be used in the natural sciences and technology, 2009.

[32] Z. Li, Z. Bao, and F. Yang. Ground moving target detection and location based on SAR images for distributed spaceborne SAR. *Science in China, Series F: Information Sciences*, 48(5):632–646, 2005.

[33] K. Suwa, K. Yamamoto, M. Tsuchida, S. Nakamura, T. Wakayama, and T. Hara. Image-Based Target Detection and Radial Velocity Estimation Methods for Multichannel SAR-GMTI. *IEEE Transactions on Geoscience and Remote Sensing*, 55(3):1325–1338, 2017.

[34] Y. Á. López, M. G. Fernández, R. Grau, and F. Las-Heras. A synthetic aperture radar (SAR)-based technique for microwave imaging and material characterization. *Electronics (Switzerland)*, 7(12), 2018.

[35] S. Dey, N. Bhogapurapu, A. Bhattacharya, D. Mandal, J. M. Lopez-Sanchez, H. McNairn, and A. C. Frery. Rice phenology mapping using novel target characterization parameters from polarimetric SAR data. *International Journal of Remote Sensing*, 42(14):5519–5543, 2021.

[36] R. S. Chatterjee, S. K. Saha, Suresh Kumar, Sharika Mathew, R. C. Lakhera, and V. K. Dadhwal. Interferometric SAR for characterization of ravines as a function of their density, depth, and surface cover. *ISPRS Journal of Photogrammetry and Remote Sensing*, 64(5):472–481, 2009.

[37] S. Guillaso, L. Ferro-Famil, A. Reigber, and E. Pottier. Building characterization using L-band polarimetric interferometric SAR data. *IEEE Geoscience and Remote Sensing Letters*, 2(3):347–351, 2005.

[38] L. Xu, H. Zhang, C. Wang, B. Zhang, and M. Liu. Crop classification based on temporal information using Sentinel-1 SAR time-series data. *Remote Sensing*, 11(1), 2019.

[39] D. W. Winters. Target motion and high range resolution profile generation. *IEEE Transactions on Aerospace and Electronic Systems*, 48(3):2140–2153, 2012.

[40] J. J. De Wit, A. Meta, and P. Hoogeboom. Modified range-doppler processing for FM-CW synthetic aperture radar. *IEEE Geoscience and Remote Sensing Letters*, 3(1):83–87, jan 2006.

[41] A. Meta, P. Hoogeboom, and L. P. Ligthart. Signal processing for FMCW SAR. In *IEEE Transactions on Geoscience and Remote Sensing*, volume 45, pages 3519–3532, 2007.

[42] C. Özdemir, C. Ozdemir, and C. Özdemir. *Inverse Synthetic Aperture Radar Imaging with MATLAB Algorithms*. Wiley Series in Microwave and Optical Engineering. Wiley, 2012.

[43] C. V. Jakowatz, D. E. Wahl, P. H. Eichel, D. C. Ghiglia, and P. A. Thompson. *Spotlight-Mode Synthetic Aperture Radar: A Signal Processing Approach*. Springer US, 1996.

[44] K. Radecki. *Szybki algorytm projekcji wstecznej oparty na współrzędnych barycentrycznych do zastosowań w aktywnych i pasywnych zobrazowaniach radarowych SAR*. PhD thesis, Warsaw University of Technology, 2020.

[45] Science Applications International. SEQAL Definition Study: Synthetic Aperture Radar Image Quality Metrics. Technical Report ADA252684, Science Applications International, 1985.

[46] R. H. Mitchel, S. Marder, S. M. R. H. Mitchel, R. H. Mitchel, and S. Marder. Synthetic Aperture Radar (SAR) Image Quality Considerations. *Optical Engineering*, 21(1):210148, 1982.

[47] QUALITY | English meaning - Cambridge Dictionary.

[48] M. Labowski. *Methods of estimation of navigational elements of unmanned aerial vehicle in radar terrain imaging system*. Phdthesis, Warsaw, 2017.

[49] L. Xin, S. Hong, X. Lu, and H. Sun. Parameter assessment for SAR image quality evaluation system. In *2007 1st Asian and Pacific Conference on Synthetic Aperture Radar Proceedings, APSAR 2007*, pages 58–60, 2007.

[50] H. Zhang, Y. Li, and Y. Su. SAR image quality assessment using coherent correlation function. In *2012 5th International Congress on Image and Signal Processing, CISP 2012*, pages 1129–1133, 2012.

[51] G. Jia, W. Chang, Q. Zhang, and X. Luan. The Analysis and Realization of Motion Compensation for Circular Synthetic Aperture Radar Data. *IEEE Journal of Selected Topics in Applied Earth Observations and Remote Sensing*, 9(7):3060–3071, 2016.

[52] W. Pu, J. Wu, Y. Huang, W. Li, Z. Sun, J. Yang, and H. Yang. Motion Errors and Compensation for Bistatic Forward-Looking SAR With Cubic-Order Processing. *IEEE Transactions on Geoscience and Remote Sensing*, 54(12):6940–6957, 2016.

[53] P. L. Bogler. Motion-Compensated SAR Image ISLR. *IEEE Transactions on Geoscience and Remote Sensing*, GE-25(6):871–878, 1987.

[54] D. C. Griffith. Phase error compensation technique for improved synthetic aperture radar performance. *Johns Hopkins APL Technical Digest (Applied Physics Laboratory)*, 18(3):358–363, 1997.

[55] T. A. Kennedy. Strapdown Inertial Measurement Units For Motion Compensation For Synthetic Aperture Radars. *IEEE Aerospace and Electronic Systems Magazine*, 3(10):32–35, 1988.

[56] M. Martorella, F. Berizzi, J. Palmer, B. Haywood, and B. Bates. Image contrast and entropy based autofocusing for polarimetric ISAR. In *2007 International Waveform Diversity and Design Conference, WDD*, pages 245–249, 2007.

[57] M. Martorella, F. Berizzi, and B. Haywood. Contrast maximisation based technique for 2-D ISAR autofocusing. *IEE Proceedings: Radar, Sonar and Navigation*, 152(4):253–262, 2005.

[58] C. Noviello, G. Fornaro, and M. Martorella. Comparison of fast and accurate parametric ISAR motion compensation techniques. In *Proceedings of the European Conference on Synthetic Aperture Radar, EUSAR*, pages 1–4, 2016.

[59] S. Brisken, M. Martorella, and J. G. Worms. Multistatic image entropy based autofocus. In *2013 14th International Radar Symposium (IRS)*, volume 1, pages 443–448, 2013.

[60] J. Wang and X. Liu. SAR Minimum-entropy autofocus using an adaptive-order polynomial model. *IEEE Geoscience and Remote Sensing Letters*, 3(4):512–516, 2006.

[61] B. J. Zhang, X. L. Zhang, and S. J. Wei. A circular SAR image autofocus algorithm based on minimum entropy. In *Proceedings of the 2015 IEEE 5th Asia-Pacific Conference on Synthetic Aperture Radar, APSAR 2015*, pages 152–155, 2015.

[62] D. Massonnet and J.-C. C. Souyris. *Imaging with synthetic aperture radar*. EPFL Press, 2008.

[63] M. A. Richards, J. A. Scheer, and W. A. Holm. *Principles of modern radar: Basic principles*. 2010.

[64] P. Samczynski and K. S. Kulpa. Coherent mapdrift technique. *IEEE Transactions on Geoscience and Remote Sensing*, 48(3 PART2):1505–1517, 2010.

[65] G. Krieger, A. Moreira, H. Fiedler, I. Hajnsek, M. Werner, M. Younis, and M. Zink. TanDEM-X: A satellite formation for high-resolution SAR interferometry. In *IEEE Transactions on Geoscience and Remote Sensing*, volume 45, pages 3317–3340, 2007.

[66] R. Bamler and P. Hartl. Synthetic aperture radar interferometry. *Inverse Problems*, 14(4), 1998.

[67] M. Martorella, E. Giusti, S. Ghio, P. Samczynski, J. Drozdowicz, M. K. Baczyk, M. Wielgo, K. Stasiak, J. Julczyk, M. Ciesielski, M. Soszka, R. Mularzuk, G. Pizziol, D. Stagliano, and S. Lischi. 3D Radar Imaging for Non-Cooperative Target Recognition. In *Proceedings International Radar Symposium*, volume 2022-Septe, pages 300–305. IEEE Computer Society, 2022.

[68] C. Tofallis, R. Horst, P. M. Padalos, and N. V. Thoai. Introduction to Global Optimization. *The Journal of the Operational Research Society*, 47(7):962, 1996.

[69] J. C. Lagarias, J. A. Reeds, M. H. Wright, and P. E. Wright. Convergence properties of the Nelder-Mead simplex method in low dimensions. *SIAM Journal on Optimization*, 9(1):112–147, 1998.

[70] C. A. Wiley. Synthetic aperture radarsa paradigm for technology evolution. *IEEE Transactions on Aerospace and Electronic Systems*, AES-21(3):440–443, 1985.

[71] C. A. Wiley. Pulsed Doppler Radar Methods and Apparatus, 1954.

[72] S. R. Cloude. Polarimetric sar interferometry. *IEEE Transactions on Geoscience and Remote Sensing*, 36(5 PART 1):1551–1565, 1998.

[73] R. M. Goldstein, H. A. Zebker, and C. L. Werner. Satellite radar interferometry: Twodimensional phase unwrapping. *Radio Science*, 23(4):713–720, 1988.

[74] L. C. Graham. Synthetic Interferometer Radar For Topographic Mapping. *Proceedings of the IEEE*, 62(6):763–768, 1974.

[75] M. Scaioni, M. Marsella, M. Crosetto, V. Tornatore, and J. Wang. Geodetic and remote-sensing sensors for dam deformation monitoring, 2018.

[76] R. Giret, H. Jeuland, and P. Enert. A study of a 3D-SAR concept for a millimeter-wave imaging radar onboard an UAV. In *Conference Proceedings - 1st European Radar Conference, EuRAD*, pages 201–204, 2004.

[77] F. Gini and F. Lombardini. Multibaseline cross-track SAR interferometry: A signal processing perspective. *IEEE Aerospace and Electronic Systems Magazine*, 20(8 II):71–92, 2005.

[78] C. H. Casteel, Jr., L. A. Gorham, M. J. Minardi, S. M. Scarborough, K. D. Naidu, and U. K. Majumder. A challenge problem for 2D/3D imaging of targets from a volumetric data set in an urban environment. In *Algorithms for Synthetic Aperture Radar Imagery XIV*, volume 6568, page 65680D, 2007.

[79] S. Auer, T. Balz, S. Becker, and R. Bamler. 3D SAR simulation of urban areas based on detailed building models, dec 2010.

[80] M. Pinheiro, P. Prats, R. Scheiber, M. Nannini, and A. Reigber. Tomographic 3D reconstruction from airborne circular SAR. In *International Geoscience and Remote Sensing Symposium (IGARSS)*, volume 3, 2009.

[81] W. N. Barnes and T. H. Gauss. Improved Height Above Target (HAT) measurement algorithm, 1998.

[82] D. André. An analysis of 3D SAR from single pass nonlinear radar platform trajectories. *Algorithms for Synthetic Aperture Radar Imagery XVII*, 7699(April 2010):769908, 2010.

[83] B. D. Rigling and R. L. Moses. Flight path strategies for 3-D scene reconstruction from bistatic SAR. *IEE Proceedings: Radar, Sonar and Navigation*, 2004.

[84] W. Stecz and K. Gromada. UAV mission planning with SAR application. *Sensors (Switzerland)*, 20(4), 2020.

[85] B. Tian, X. Zhang, L. Dang, and S. Wei. A Fast Compressed Sensing 3D SAR Imaging Method Based on the Adaptive Threshold. In *FUSION 2019 - 22nd International Conference on Information Fusion*, 2019.

[86] L. Tang, H. Meng, X. Chen, J. Zhang, L. Lv, and K. Liu. A Novel 3D Imaging Method of FMCW MIMO-SAR. In *2018 China International SAR Symposium, CISS 2018 - Proceedings*. Institute of Electrical and Electronics Engineers Inc., nov 2018.

[87] S. peng Lai, M. lu Lan, Y. xuan Li, and B. M. Chen. Safe navigation of quadrotors with jerk limited trajectory. *Frontiers of Information Technology and Electronic Engineering*, 20(1):107–119, 2019.

[88] PX4-Contributors. Jerk-limited Type Trajectory for Multicopters | PX4 User Guide.

[89] PX4-Contributors. Parameter Reference | PX4 User Guide.

[90] J. A. Nelder and R. Mead. A Simplex Method for Function Minimization. *The Computer Journal*, 7(4):308–313, jan 1965.

[91] Mathworks. Find Minimum of Unconstrained Multivariable Function Using Derivative-Free Method - MATLAB fminsearch., 2013.

[92] M. Wielgo, D. Gromek, P. Samczynski, K. Stasiak, and M. Gawel. Low-Cost High-Resolution SAR Imaging on Drone with Mechanical Antenna Stabilization. In *Proceedings International Radar Symposium*, volume 2022-Septe, pages 83–86. IEEE Computer Society, 2022.

[93] J. Julczyk, K. Stasiak, D. Gromek, and M. Ciesielski. Four-Channel C-Band FMCW Radar Demonstrator with Real-Time Signal Processing and Data Presentation. In *2021 Signal Processing Symposium, SPSympo 2021*, pages 107–111. Institute of Electrical and Electronics Engineers Inc., 2021.